Numerical Simulation of Unsteady Convective Flow and Heat Transfer under Transient Boundary Condition using Lattice Boltzmann Method: Application to Geothermal System

アディティヤ, デワント, ハルトノ

https://hdl.handle.net/2324/4496055

Numerical Simulation of Unsteady Convective Flow and Heat Transfer under Transient Boundary Condition using Lattice Boltzmann Method: Application to Geothermal System

Aditya Dewanto Hartono

Numerical Simulation of Unsteady Convective Flow and Heat Transfer under Transient Boundary Condition using Lattice Boltzmann Method: Application to Geothermal System

A Doctoral Thesis Submitted to Kyushu University

For the Degree of Doctor of Engineering

By

Aditya Dewanto Hartono

Supervised by:

Professor Yuichi Sugai

Department of Earth Resources Engineering

Graduate School of Engineering

Kyushu University

2021

Abstract

Development of environmental-friendly natural energies has raised interest within the international research community due to their potential to prevent global warming by reduction of carbon dioxide (CO_2) emissions. Geothermal energy, amongst them, is acknowledged as the most promising underground natural resource. However, porous and fracture water flows in underground reserves include unclear factors. To increase efficiency in acquisition of geothermal heat, a better understanding of heat transfer processes occurring within geothermal reservoirs is necessary. This could be achieved by the development of a suitable numerical simulation methodology representative of the geothermal phenomena.

The direction of simulation studies on underground natural water flows related to the geothermal system has shifted to account for the importance of disclosing the fundamental physics behind the phenomena. Accordingly, the corresponding heat and mass transfer pertinent to the geothermal system may be regarded as a special mode of Rayleigh-Bènard convection flow with time-varying heat flux contribution from the hot underground rock formation. Such conditions trigger the emergence of unsteady convective fluid and thermal motions within the porous formation of the geothermal system. Undoubtedly, understanding such complex thermo-hydrodynamics system possesses considerable challenges.

The Lattice Boltzmann Method (LBM) has emerged as a powerful computational fluid dynamics (CFD) technique not only for handling typical industrial fluid-thermal problems, but also in uncovering the foundational aspects pertinent to the thermo-hydrodynamics of the geothermal system. As such, LBM can be a promising tool to assess the heat and mass transport problems at hand, due to its uniqueness compared to the traditional CFD methods in sense that LBM solves the representative Boltzmann expression of the flowing substances rather than directly handling the constitutive hydrodynamics equations in their operations. Modeling a flow problem using LBM has several advantages including a clear algorithm, straightforward treatment of boundary conditions, and innate feasibility for parallel computing architecture.

This study therefore aims to simulate the unsteady Rayleigh-Bènard convective fluid flow and heat transfer in a cavity domain with a time-varying temperature condition using the modified LBM that has been presented by considering second-order accuracy in space and time coordinates to follow complex and fast heat and mass transfer phenomena.

The thesis consists of six chapters laid out as follows:

Chapter 1 presents the background and primary objectives of the present study followed by a comprehensive literature reviews. The chapter finalizes by posing the structure of the current treatise.

Chapter 2 explains the formulation of fundamental theory of the lattice Boltzmann method (LBM) with emphasis on the establishment of the modified LBM scheme that is second-order accurate in spatial and temporal coordinates. The discussion was commenced by delivering the core concept of LBM, which is based on statistical mechanics. Thereupon, the perspective of LBM in respect of the flowing materials was elucidated. The stress was given to the uniqueness of LBM amongst other CFD methods. Subsequently, the Chapman-Enskog analysis was introduced as the vital element in LBM framework. The concept of discrete lattice velocity arrangement was presented, alongside associated procedures for assigning initial and boundary conditions in LBM. The prescribed LBM scheme was preliminarily applied for conducting natural convection simulation in a differentially-heated cavity with opposing hot and cold vertical walls to confirm the capacity and validity of the present LBM scheme.

Chapter 3 demonstrates the applicability of present LBM scheme in simulating natural convection and heat transfer phenomena during the unsteady period of the flow. As far as modeling the flow problem using LBM is concerned, two properties are routinely considered including (a) the discrete lattice Boltzmann expressions, and (b) the discrete forcing schemes. The contemporary issue regarding proper selection of lattice Boltzmann scenario based on the availability of diverse expressions relates to the aforementioned two properties was examined in detail. Later on, the computational performance of disparate LBM scenarios was tested upon two distinct physical configurations, namely the natural convection in a differentially-heated cavity and the Rayleigh-Bènard convection with aspect ratio equal to unity. The superior capacity of the modified LBM scheme considering to the standard first-order counterpart was discernible from the numerical results of both physical phenomena.

Chapter 4 investigates the unsteady Rayleigh-Bènard convection with transient boundary conditions in a rectangular cavity of aspect ratio two. Herein, the transient boundary was invoked by assigning a time-periodic condition for the hot wall at the bottom side of the domain. Meanwhile, the opposing horizontal wall at the top was kept at constant cold temperature. By appointing the vertical boundaries to be perfectly insulated, the flow domain was a simplification of a closed-thermodynamic system with unsteady heat flux from the bottom ambient. Using the modified LBM scheme by considering second-order accurate, principal focus was bestowed upon disclosing the impact of

amplitude and frequency of the hot oscillating wall upon the convective fluid flow and heat transfer characteristics for different Rayleigh number conditions.

Chapter 5 extends the analysis to the effect of distinct aspect ratios upon the convective flow and heat transfer characteristics of the system under investigation. Finally, the currently unresolved problem regarding heat and mass transfer behavior of Rayleigh-Bènard system under the influence of high-oscillation frequency of the hot wall was investigated in detail. It was therefore concluded that the modified LBM simulation methodology is capable in simulating diverse conditions of the unsteady Rayleigh-Bènard convection system, including the extreme cases of high-frequency oscillation of the hot wall.

Chapter 6 poses some concluding remarks of the present study. As final annotation, a few plausible directions for future works were provided therein, as well.

Acknowledgments

Table of Contents

List of Figures

List of Tables

Chapter 1: Introduction

1.1 Background

Geothermal energy has been acknowledged as one of the most promising environmental-friendly natural energies that holds potential to mitigate global warming. By definition, geothermal energy is energy in the form of heat that is contained within the hot interior of the Earth. Geothermal energy is commonly used for power plant generation. Being considered as renewable and clean natural resource, geothermal energy holds important role in the future.
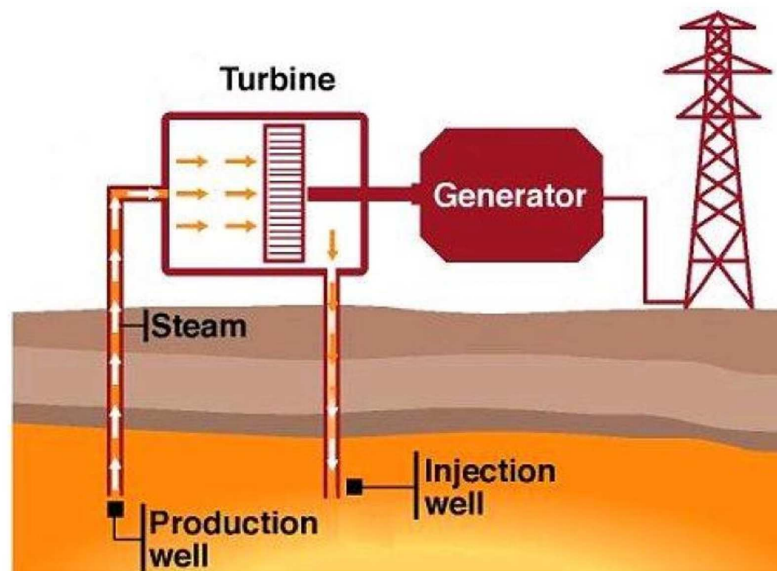
Figure 1.1. Schematic illustration of geothermal energy utilization in power-plant generation (mozambiqueminingpost.com).

At the current era of increasing concern regarding environmental issues, better understanding of the physical processes involved in the geothermal reservoirs is pivotal to promote utilization of such natural resource. However, thorough apprehension regarding the underlying physics of heat and mass transfer in geothermal energy is challenged by the inherent complexity of the phenomena. Fluid flows and heat transfer in underground porous media includes challenging and unclear factors. Comprehensive assessment through implementation of suitable numerical simulation technique

might offer a way to decipher such complexity, hence providing opportunity to gain better understanding of thermal convection flow and heat transfer in hot underground geothermal reservoir.

The direction of simulation studies on underground natural water flows related to the geothermal system has shifted to account for the importance of disclosing the fundamental physics behind the phenomena. Accordingly, the corresponding heat and mass transfer pertinent to the geothermal system may be regarded as a special mode of Rayleigh-Bènard convection flow with time-varying heat flux contribution from the hot underground rock formation. Such conditions trigger the emergence of unsteady convective fluid and thermal motions within the porous formation of the geothermal system. Undoubtedly, understanding such complex thermo-hydrodynamics system possesses considerable challenges.

The Lattice Boltzmann Method (LBM) has emerged as a powerful computational fluid dynamics (CFD) technique not only for handling typical industrial fluid-thermal problems, but also in uncovering the foundational aspects pertinent to the thermo-hydrodynamics of the geothermal system. Relying on the statistical mechanics, LBM regards the flowing materials through the collective behavior of the accompanying molecules (He and Doolen, 2002; Kruger *et al.*, 2017). It differs from traditional CFD methods in sense that it solves the representative Boltzmann expression of the flowing substances rather than directly handling the corresponding hydrodynamics equations in their operations. Because of this unique feature, modelling a flow problem using LBM has several advantages, including a clear algorithm (Trouette, 2013), straightforward treatment of boundary conditions (Mezrhab *et al.*, 2010), and innate feasibility for parallel computing architecture (Jami *et al.*, 2016). As a promising numerical tool, LBM is currently a vibrant research topic in the discipline of CFD. As such, LBM can be a promising tool to assess the heat and mass transport problems at hand.

1.2 Literature Study

As far as modelling the flow problem using LBM is concerned, two properties are routinely considered: (a) the discrete lattice Boltzmann expressions, and (b) the discrete forcing schemes. The former parameter has been extensively discussed in the literature. Ubertini *et al.*, (2010) investigated three distinct models of discrete lattice Boltzmann expression for hydrodynamics simulation, namely the first-order, the second-order, and the scheme derived through implementation of the Verlet discretization, which all showed a second-order accuracy both in spatial and time coordinates with

respect to the convective system. They argued that such equivalence breaks down when the nature of the physical systems necessitates the inclusion of external forcing expression.

Silva and Semiao (2012) carried out a comprehensive assessment of distinct lattice Boltzmann remarks using Chapman-Enskog analysis. Guo *et al.* (2002) highlight the significance of the different lattice Boltzmann schemes towards the accuracy of the recovered Navier-Stokes expression from the Chapman-Enskog analysis. Additionally, they mentioned that the choice of discrete forcing model depends heavily upon the exactitude of the restored continuum hydrodynamics representation.

On the other hand, the discrete forcing model in LBM is the other prominent property when modelling the flow is sought. Several authors have proposed diverse expressions to accommodate external forcing term in the generic lattice Boltzmann equation. Luo (2000) was among the first authors to propose a mathematical expression for the discrete forcing term in LBM, alongside with He *et al.* (1998) and Guo *et al.* (2002). Later on, Kupershtokh *et al.* (2009) introduced a forcing model based on the association of exact-difference-method upon the corresponding Boltzmann equation.

The presence of different mathematical expressions for both the discrete lattice Boltzmann equation and the forcing model offers diverse LBM strategies for hydrodynamics modelling. However, choosing a suitable approach is still a matter of debate. To alleviate such issues, Mohamad and Kuzmin (2010) investigated the behavior of three different forcing models by simulating natural convection in closed and open-ended cavities. They found that the investigated forcing models produced equivalent numerical solutions at steady-state conditions.

Subsequently, Krivovichev (2019) presented a comprehensive evaluation regarding stability analysis of the six widely-used forcing models based on the application of the von Neumann method to linear approximation of the system of nonlinear lattice Boltzmann expressions. They found that better stability properties prevailed upon the forcing models that are implicit in their nature. Zheng *et al.* (2019) found that as long as the simulation comprises low Mach number flow, different forcing schemes in LBM would return equivalent steady-state solutions.

It is apparent from the available literature that few works have looked into the implications of both distinct lattice Boltzmann expressions and different forcing models in LBM simulation. Moreover, the primary focus of the published works has revolved around the discrepancy in the computational characteristics of distinct LBM scenarios during the steady-state condition of the simulation, leaving the behavior during the unsteady period of the flow unexplained.

Pertinent to the unsteady thermal convection and heat transfer, earlier studies mainly focused on investigating the unsteady heat and fluid flow in a differentially-heated cavity arrangement. Herein,

the enclosure was subjected upon contrasting temperature conditions at the opposing vertical walls, while the horizontal perimeters were assumed to be adiabatic. The pioneering simulation work in the topic of unsteady convection in a differentially-heated cavity was performed by Kazmierczak and Chinoda (1992) using finite difference method (FDM). The study was later followed by other researchers using different numerical techniques (Antohe and Lage, 1996, 1997; Kwak and Hyun, 1996). Few variations of the study were also available involving porous media (Wang *et al.*, 2008; Wu and Wang, 2017), nanofluid (Sheremet *et al.*, 2018) and magnetic field (Kefayati, 2013).

To the best of the author's knowledge, almost all of the former studies assessing unsteady thermal convection incorporates differentially-heated cavity in their assessments. Perhaps, the only treatise close enough to representing the geothermal system was the recent investigation of Nasseri *et al.* (2021). Nevertheless, instead of the bottom hot wall, the oscillating wall was appointed at the top cold boundary. Therefore, the topic of unsteady fluid flow and thermal convection under the framework of Rayleigh-Bènard convection is currently very scarce.

1.3 Objectives

The primary objectives of this thesis were as follows:

1. To propose a modified LBM scheme that is second-order accurate in spatial and temporal spaces. The modified LBM scheme includes the single-relaxation-time (SRT) and the two-relaxation-time (TRT) scenarios.

2. To elucidate the contemporary unclear issue regarding proper selection of LBM schemes in simulating thermal convection and heat transfer problems.

3. To implement the proposed LBM scheme in evaluating the unsteady Rayleigh-Bènard convection triggered by transient hot temperature at the bottom boundary wall.

1.4 Outline of the Thesis

The thesis is hierarchically constructed as follows:

Chapter 2 explains the formulation of fundamental theory of the lattice Boltzmann method (LBM) with emphasis on the establishment of the modified LBM scheme that is second-order accurate in spatial and temporal coordinates. The proposed LBM scheme was preliminarily applied for conducting natural convection simulation in a differentially-heated cavity with opposing hot and cold vertical walls to confirm the capacity and validity of the present LBM scheme.

Chapter 3 demonstrates the applicability of present LBM scheme in simulating natural convection and heat transfer phenomena during the unsteady period of the flow. The contemporary issue regarding proper selection of lattice Boltzmann scenario based on the availability of diverse expressions relates to the (a) discrete lattice Boltzmann model and (b) discrete forcing schemes was examined in detail.

Chapter 4 investigates the unsteady Rayleigh-Bènard convection with transient boundary conditions in a rectangular cavity of aspect ratio two. Herein, the transient boundary was invoked by assigning a time-periodic condition for the hot wall at the bottom side of the domain. Meanwhile, the opposing horizontal wall at the top was kept at constant cold temperature. Using the modified LBM scheme by considering second-order accurate, principal focus was bestowed upon disclosing the impact of amplitude and frequency of the hot oscillating wall upon the convective fluid flow and heat transfer characteristics for different Rayleigh number conditions.

Chapter 5 extends the analysis to the effect of distinct aspect ratios upon the convective flow and heat transfer characteristics of the system under investigation. Finally, the currently unresolved problem regarding heat and mass transfer behavior of Rayleigh-Bènard system under the influence of high-oscillation frequency of the hot wall was investigated.

Chapter 6 poses some concluding remarks of the present study as well as plausible directions for future works.

Chapter 2: Fundamental Theory of Lattice Boltzmann Method

2.1 Introduction to Computational Fluid Dynamics

Computational fluid dynamics (CFD) is a specific subset of fluid mechanics that examine the behavior of flowing substances by means of numerical analysis. Here, the governing equations representing the dynamics of the flowing materials possess essential role. Such formulations are typically portrayed by a set of partial differential equations describing conservation of mass, momentum, and energy (Çengel and Cimbala, 2018; Pletcher *et al.*, 2016). The core idea of CFD is therefore to find particular solutions of the governing equations for the specific system under investigation with the aid of computing devices (Kruger *et al.*, 2017; Pletcher *et al.*, 2016).

Typical in CFD is discretization of the associated dynamical equations at hand. As such, the continuum formulations must be transformed into their commensurate discrete forms, which then allow them to be deciphered into a step-by-step recipes suitable for implementation within a computer ecosystem. There are many well-established numerical discretization techniques available in the literature. The conventional numerical methods, amongst them, are the most prominent algorithms. In this framework, the flowing constituents are treated as a collection of infinitesimal macroscopic control units. Hence, the perspective is macroscopic, and the fluid is regarded as a continuum quantity (Mohamad, 2019). Depending on the discretizing way the associated dynamical equations, the classical numerical methods may be classified into finite difference method (FDM), finite volume method (FVM) and finite element method (FEM) (Kruger *et al.*, 2017; Mohamad, 2019; Moufekkir *et al.*, 2012).

On the other hand, a relatively nascent CFD technique has emerged by considering the flowing substances from microscopic standpoint. Such method is termed as molecular dynamics (MD) (Kruger *et al.*, 2017). In MD simulation, evolution of each molecules composing a particular flowing substance is tracked. Thereupon, accumulation of dynamical states from all the individual molecules constituting the flowing material is regarded as the representative of the dynamical condition of the system at hand. Because MD simulation includes tracking of individual molecules, enormous computing resource is required in performing flow modeling. Consequently, application of MD

simulation is currently still limited in the microscopic-scale domain. Extensive researches are underway to extend the applicability of MD technique in simulating flow physics in a larger-scale.

Another type of numerical technique prevailed as the extension of the lattice gas automata method (Shan, 1997). Relying on statistical mechanics, the so-called lattice Boltzmann method (LBM) has been established within the discipline of CFD. Here, instead of examining each individual molecules, LBM regards the flowing materials through the collective behavior of the accompanying molecules (He and Doolen, 2002; Kruger *et al.*, 2017). Hence, the perspective of LBM falls in between macroscopic and microscopic standpoints, termed as mesoscopic viewpoint (Kruger *et al.*, 2017; Mohamad, 2019; Succi, 2001). Figure 2.1 illustrates the classification of CFD techniques based on their approach in treating the flowing substances.

2.2   Principles of Lattice Boltzmann Method

The Lattice Boltzmann Method (LBM) was proposed in 1988 by McNamara and Zanetti as a modified scenario to overcome the deficiency of the earlier lattice gas automata (LGA) algorithm in modeling fluid displacement (Mohamad, 2019; Succi, 2001; Sukop and Thorne, 2006). As time proceeds, LBM has consistently demonstrated its superiority against the LGA technique. Henceforward, LBM has replaced its predecessor as the favorable numerical technique in practical flow modeling. As a promising numerical tool, LBM has raised considerable interest and is currently a vibrant research topic in the discipline of CFD (Seta, 2010).

The principal distinctive feature of LBM compared with the classical numerical methods lies upon its nature in solving the representative Boltzmann equation of the flowing materials instead of directly handling the prevalent hydrodynamics equations. Following the principle of kinetic theory of gases, LBM regards the flowing materials as accumulations of their pertinent particles. Here, each corresponding particle itself resembles collection of molecules of a particular flowing entity. In the framework of the kinetic theory of gases, the gas particles always collide each other during their movements. Following this notion, LBM imitates the behavior of gas molecules in manifesting the dynamics of the flowing materials. Accordingly, materials displacements in LBM are represented by a series of collision and propagation amongst the associated particles. In LBM, the movement of the flowing entities is manifested by tracking the representative distribution function of the particles. The evolutionary equation of the distribution function in spatial and temporal coordinates is defined as the Boltzmann equation.
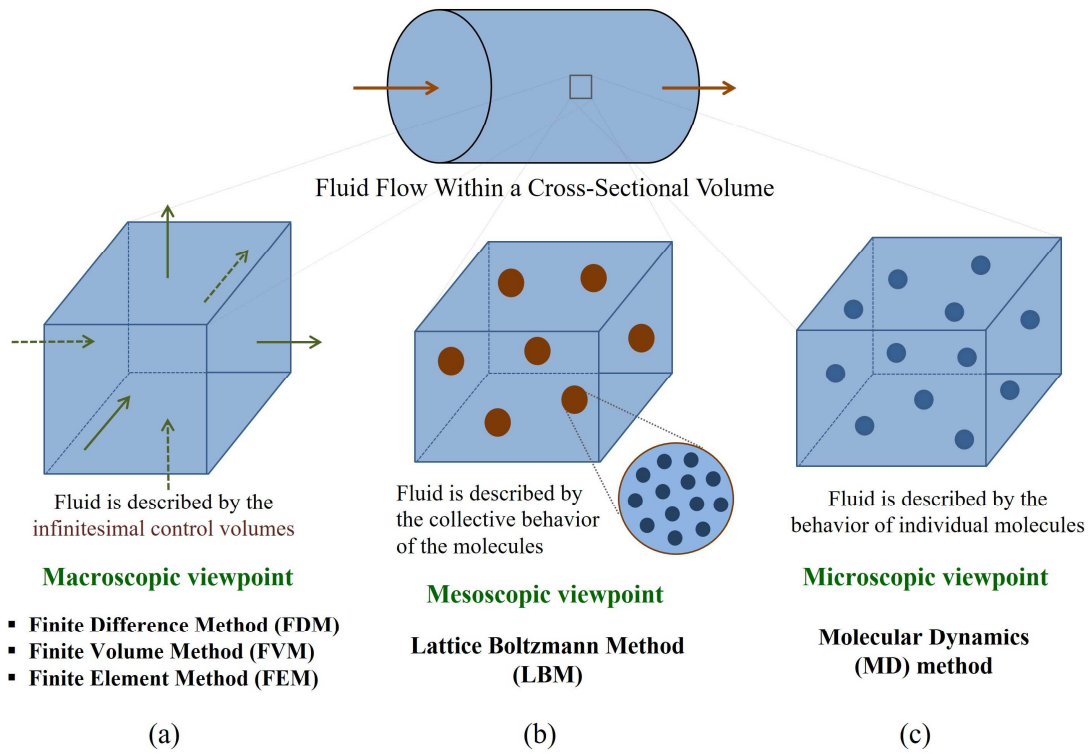
Figure 2.1. Classification of computational fluid dynamics techniques, including (a) classical methods, (b) lattice Boltzmann method, and (c) molecular dynamics method.

As a particle-based numerical technique, LBM offers several advantages over the classical CFD solvers. These include: (a) clear algorithm (Trouette, 2013), (b) straightforward treatment of boundary conditions (Mezrhab *et al.*, 2010; Varmazyar *et al.*, 2017; Wada *et al.*, 2020), (c) innate feasibility for parallel computing architecture (Calore *et al.*, 2016; Jami *et al.*, 2016; Molla *et al.*, 2018; Wei *et al.*, 2018), (d) capability of LBM in simultaneously solve the Navier-Stokes and continuity equations without the necessity of solving Poisson's equation (Seta, 2009; Sukop and Thorne, 2006), (e) direct connection between fluid density and pressure through the equation of state (Kruger *et al.*, 2017; Sukop and Thorne, 2006), and (f) ease in incorporating additional physical complexity into the system at hand (He and Luo, 1997; El Mansouri *et al.*, 2017).

2.3 Lattice Boltzmann Equations for Convective Fluid Flow and Heat Transfer

Convective fluid flow and heat transfer phenomena are governed by two flowing entities that propagate simultaneously and synergistically within the flow domain, namely the fluid and thermal

substances. In its operation, LBM distinguishes the mesoscopic representation of fluid and thermal components. The fluid particles are represented by the density distribution function (*f*), while the thermal element is represented by the temperature distribution function (*g*). Each of the corresponding distribution functions satisfies the representative Boltzmann equations for the fluid and thermal substances, respectively.

For the fluid constituent, the Boltzmann equation depicts the evolution of the density distribution function, expressed as

$$\frac{\partial f}{\partial t} + \xi_\alpha \frac{\partial f}{\partial x_\alpha} + \frac{F_\alpha}{\rho} \frac{\partial f}{\partial \xi_\alpha} = \Omega(f),$$
(3.1)

where f, ξ_α, ρ, F_α and $\Omega(f)$ denote the density distribution function, fluid particles' velocity, fluid density, external force and density collision operator, respectively. It is noteworthy to mention that equation (3.1) is defined in the phase space, which consists of the velocity and spatial-temporal spaces. Performing discretization of equation (3.1) in velocity coordinate results in the following remark:

$$\frac{\partial f_i}{\partial t} + \xi_{i\alpha} \frac{\partial f_i}{\partial x_\alpha} = \Omega_i(f_i) + R_i,$$
(3.2)

where f_i, $\xi_{i\alpha}$, R_i and $\Omega_i(f_i)$ designate the discrete density population, discrete velocities of fluid particles, discrete forcing expression and discrete form of density collision operator, respectively.

For the thermal constituent, the representative Boltzmann equation portrays the evolution of the temperature distribution function within the phase space, expressed as

$$\frac{\partial g}{\partial t} + e_\alpha \frac{\partial g}{\partial x_\alpha} = \Omega(g).$$
(3.3)

Here, g, e_α and $\Omega(g)$ denote the temperature distribution function, thermal particles' velocity and thermal collision operator, respectively. The discrete-velocity form of equation (3.3) takes the following form:

$$\frac{\partial g_i}{\partial t} + e_{i\alpha} \frac{\partial g_i}{\partial x_\alpha} = \Omega_i(g_i),$$
(3.4)

where g_i, $e_{i\alpha}$ and $\Omega_i(g_i)$ specify the discrete thermal population, discrete velocities of thermal particles and discrete collision operator for thermal particles, correspondingly.

In order to obtain the proper discrete representations of Boltzmann equation from both flowing entities, equations (3.2) and (3.4) need to be discretized further in spatial and temporal spaces. In the present study, the stress was given to elucidate the associated spatial-temporal discretization

operations that will produce the discrete lattice Boltzmann equations which are second-order accurate in time and space. Such model was found to be capable in returning better numerical stability and accuracy than the standard first-order accurate lattice Boltzmann scheme. Thereupon, appraisal regarding extension of the modified lattice Boltzmann scheme to include advanced collision term was provided in detail.

2.3.1 Single-Relaxation-Time Lattice Boltzmann Model for Fluid and Thermal Components

The current section elucidates the establishment of single-relaxation-time (SRT) lattice Boltzmann equations for fluid and thermal substances that occupy second-order accuracy in spatial and temporal dimensions. As such, discretization of equations (3.2) and (3.4) was administered by capturing the associated expanded formulas up to the second-truncation terms.

For the fluid population, the derivation of second-order SRT lattice Boltzmann equation was commenced by expanding the left-hand side of equation (3.2) as

$$\frac{\partial f_i}{\partial t} + \xi_{i\alpha}\frac{\partial f_i}{\partial x_\alpha} = \frac{f_i(x_\alpha, t+\Delta t) - f_i(x_\alpha, t)}{\Delta t} + \frac{\Delta x_\alpha}{\Delta t}\frac{f_i(x_\alpha + \xi_{i\alpha}\Delta t, t+\Delta t) - f_i(x_\alpha, t+\Delta t)}{\Delta x_\alpha}$$

$$\frac{\partial f_i}{\partial t} + \xi_{i\alpha}\frac{\partial f_i}{\partial x_\alpha} = \frac{f_i(x_\alpha + \xi_{i\alpha}\Delta t, t+\Delta t) - f_i(x_\alpha, t)}{\Delta t}. \tag{3.5}$$

Meanwhile, expansion of the expressions on the right-hand side of equation (3.2) satisfies the following remarks, accordingly:

$$\Omega_i(f_i) \cong \frac{\Omega_i(f_i)(x_\alpha + \xi_{i\alpha}\Delta t, t+\Delta t)}{2} + \frac{\Omega_i(f_i)(x_\alpha, t)}{2} \tag{3.6}$$

$$R_i \cong \frac{R_i(x_\alpha + \xi_{i\alpha}\Delta t, t+\Delta t)}{2} + \frac{R_i(x_\alpha, t)}{2}. \tag{3.7}$$

Thereupon, combining equations (3.5) - (3.7) the expanded-form of equation (3.2) takes the following description:

$$\frac{f_i(x_\alpha + \xi_{i\alpha}\Delta t, t+\Delta t) - f_i(x_\alpha, t)}{\Delta t} = \frac{\Omega_i(f_i)(x_\alpha + \xi_{i\alpha}\Delta t, t+\Delta t) + \Omega_i(f_i)(x_\alpha, t)}{2}$$

$$+ \frac{R_i(x_\alpha + \xi_{i\alpha}\Delta t, t+\Delta t) + R_i(x_\alpha, t)}{2}. \tag{3.8}$$

Introducing the following definitions,

$$\tilde{f}_i(x_\alpha, t) = f_i(x_\alpha, t) - \frac{\Omega_i(f_i)(x_\alpha, t)\Delta t}{2} - \frac{R_i(x_\alpha, t)\Delta t}{2} \tag{3.9}$$

$$\tilde{f}_i\left(x_\alpha + \xi_{i\alpha}\Delta t, t + \Delta t\right) = f_i\left(x_\alpha + \xi_{i\alpha}\Delta t, t + \Delta t\right) - \frac{\Omega_i\left(f_i\right)\left(x_\alpha + \xi_{i\alpha}\Delta t, t + \Delta t\right)\Delta t}{2}$$
$$- \frac{R_i\left(x_\alpha + \xi_{i\alpha}\Delta t, t + \Delta t\right)}{2}, \tag{3.10}$$

equation (3.8) can be expressed as

$$\tilde{f}_i\left(x_\alpha + \xi_{i\alpha}\Delta t, t + \Delta t\right) = \tilde{f}_i\left(x_\alpha, t\right) + \Omega_i\left(f_i\right)\left(x_\alpha, t\right)\Delta t + R_i\left(x_\alpha, t\right)\Delta t. \tag{3.11}$$

Subsequently, the Bhatnagar-Gross-Krook (BGK) model (He and Doolen, 2002; Kruger *et al.*, 2017) was employed to approximate the expression of discrete collision operator form $\Omega_i\left(f_i\right)$. Such premise was described by

$$\Omega_i\left(f_i\right)\left(x_\alpha, t\right) = -\frac{1}{\tau_f}\left(f_i\left(x_\alpha, t\right) - f_i^{eq}\left(x_\alpha, t\right)\right), \tag{3.12}$$

where τ_f denotes the relaxation time for fluid population. Quantity f_i^{eq} depicts the density equilibrium population and is defined as

$$f_i^{eq} = w_i \rho \left(1 + \frac{\xi_{i\alpha} u_\alpha}{c_s^2} + \frac{\left(\xi_{i\alpha} u_\alpha\right)^2}{2c_s^4} - \frac{u_\alpha u_\beta}{2c_s^2}\right). \tag{3.13}$$

Here, u_α and c_s specify the fluid velocity and the lattice speed of sound. Quantity w_i specifies the weighting constants for density population which values are unique to the selected lattice velocity set.

Substituting equation (3.12) into (3.11), the following description prevailed:

$$\tilde{f}_i\left(x_\alpha + \xi_{i\alpha}\Delta t, t + \Delta t\right) = \tilde{f}_i\left(x_\alpha, t\right) - \frac{\Delta t}{\tau_f}\left(f_i\left(x_\alpha, t\right) - f_i^{eq}\left(x_\alpha, t\right)\right) + R_i\left(x_\alpha, t\right)\Delta t. \tag{3.14}$$

Performing necessary mathematical arrangements upon equation (3.14), the following remarks emanated:

$$\tilde{f}_i\left(x_\alpha + \xi_{i\alpha}\Delta t, t + \Delta t\right) - \tilde{f}_i\left(x_\alpha, t\right) = -\frac{f_i\left(x_\alpha, t\right)\Delta t}{\tau_f} + \frac{f_i^{eq}\left(x_\alpha, t\right)\Delta t}{\tau_f} + \frac{\tau_f R_i\left(x_\alpha, t\right)\Delta t}{\tau_f}$$
$$\tilde{f}_i\left(x_\alpha + \xi_{i\alpha}\Delta t, t + \Delta t\right) - \tilde{f}_i\left(x_\alpha, t\right) = -\frac{\Delta t}{\tau_f}\left(f_i\left(x_\alpha, t\right) - f_i^{eq}\left(x_\alpha, t\right) - \tau_f R_i\left(x_\alpha, t\right)\right). \tag{3.15}$$

Subsequently, combining equations (3.9) and (3.12), the following remark prevailed:

$$f_i\left(x_\alpha, t\right) = \frac{2\tau_f\left(\tilde{f}_i\left(x_\alpha, t\right) + \frac{\Delta t}{2\tau_f} f_i^{eq}\left(x_\alpha, t\right) + \frac{\Delta t}{2} R_i\left(x_\alpha, t\right)\right)}{2\tau_f + \Delta t}. \tag{3.16}$$

Substituting equation (3.16) into (3.15), the following expressions emerged:

$$\tilde{f}_i\left(x_\alpha+\xi_{i\alpha}\Delta t,t+\Delta t\right)-\tilde{f}_i\left(x_\alpha,t\right)=-\frac{\Delta t}{\tau_f}\left(\frac{2\tau_f\tilde{f}_i\left(x_\alpha,t\right)+f_i^{eq}\Delta t+\tau_f R_i\left(x_\alpha,t\right)\Delta t}{2\tau_f+\Delta t}\right)$$

$$+\frac{\Delta t}{\tau_f}f_i^{eq}\left(x_\alpha,t\right)+\frac{\Delta t}{\tau_f}\tau_f R_i\left(x_\alpha,t\right)$$

$$\tilde{f}_i\left(x_\alpha+\xi_{i\alpha}\Delta t,t+\Delta t\right)-\tilde{f}_i\left(x_\alpha,t\right)=-\frac{\Delta t}{\tau_f}\left(\frac{2\tau_f\left(\tilde{f}_i\left(x_\alpha,t\right)-f_i^{eq}\left(x_\alpha,t\right)\right)-2\tau_f^2 R_i\left(x_\alpha,t\right)}{2\tau_f+\Delta t}\right) \quad (3.17)$$

$$\tilde{f}_i\left(x_\alpha+\xi_{i\alpha}\Delta t,t+\Delta t\right)-\tilde{f}_i\left(x_\alpha,t\right)=-\frac{\Delta t}{\tau_f+\dfrac{\Delta t}{2}}\left(\tilde{f}_i\left(x_\alpha,t\right)-f_i^{eq}\left(x_\alpha,t\right)\right)+\frac{\tau_f R_i\left(x_\alpha,t\right)\Delta t}{\tau_f+\dfrac{\Delta t}{2}}.$$

Thereupon, the second-order SRT lattice Boltzmann equation for the fluid population was obtained as

$$\tilde{f}_i\left(x_\alpha+\xi_{i\alpha}\Delta t,t+\Delta t\right)-\tilde{f}_i\left(x_\alpha,t\right)=-\frac{\Delta t}{\tau_f+\dfrac{\Delta t}{2}}\left(\tilde{f}_i\left(x_\alpha,t\right)-f_i^{eq}\left(x_\alpha,t\right)\right)+\frac{\tau_f R_i\left(x_\alpha,t\right)\Delta t}{\tau_f+\dfrac{\Delta t}{2}}. \quad (3.18)$$

Introducing the following pseudo-variable for the relaxation time,

$$\tilde{\tau}_f=\tau_f+\frac{\Delta t}{2}, \quad (3.19)$$

equation (3.18) can be expressed as

$$\tilde{f}_i\left(x_\alpha+\xi_{i\alpha}\Delta t,t+\Delta t\right)-\tilde{f}_i\left(x_\alpha,t\right)=-\frac{\Delta t}{\tilde{\tau}_f}\left(\tilde{f}_i\left(x_\alpha,t\right)-f_i^{eq}\left(x_\alpha,t\right)\right)+\left(1-\frac{\Delta t}{2\tilde{\tau}_f}\right)R_i\left(x_\alpha,t\right)\Delta t. \quad (3.20)$$

Equation (3.20) is the preferred expression of the second-order SRT (or BGK) lattice Boltzmann equation representing the evolution of the fluid particles. In practical computer programming, equation (3.20) is typically decomposed into two interlinked steps, namely the collision and streaming steps, defined as

Collision step:

$$\tilde{f}_i^*\left(x_\alpha,t\right)=\tilde{f}_i\left(x_\alpha,t\right)-\frac{\Delta t}{\tilde{\tau}_f}\left(\tilde{f}_i\left(x_\alpha,t\right)-f_i^{eq}\left(x_\alpha,t\right)\right)+\left(1-\frac{\Delta t}{2\tilde{\tau}_f}\right)R_i\left(x_\alpha,t\right)\Delta t. \quad (3.21)$$

Streaming step:

$$\tilde{f}_i\left(x_\alpha+\xi_{i\alpha}\Delta t,t+\Delta t\right)=\tilde{f}_i^*\left(x_\alpha,t\right).$$

The density relaxation time $\tilde{\tau}_f$ is tied to the fluid kinematic viscosity of the fluid υ as

$$v = c_s^2 \left(\tilde{\tau}_f - \frac{\Delta t}{2} \right). \tag{3.22}$$

For the thermal population, the derivation of concomitant second-order SRT lattice Boltzmann equation was administered by expanding the left-hand side of equation (3.4) as

$$\frac{\partial g_i}{\partial t} + e_{i\alpha} \frac{\partial g_i}{\partial x_\alpha} = \frac{g_i(x_\alpha, t + \Delta t) - g_i(x_\alpha, t)}{\Delta t} + \frac{\Delta x_\alpha}{\Delta t} \frac{g_i(x_\alpha + e_{i\alpha}\Delta t, t + \Delta t) - g_i(x_\alpha, t + \Delta t)}{\Delta x_\alpha}$$

$$\frac{\partial g_i}{\partial t} + e_{i\alpha} \frac{\partial g_i}{\partial x_\alpha} = \frac{g_i(x_\alpha + e_{i\alpha}\Delta t, t + \Delta t) - g_i(x_\alpha, t)}{\Delta t}. \tag{3.23}$$

On the other hand, expanding the right-hand side of equation (3.4) returns the following remark:

$$\Omega_i(g_i) \cong \frac{\Omega_i(g_i)(x_\alpha, t) + \Omega_i(g_i)(x_\alpha + e_{i\alpha}\Delta t, t + \Delta t)}{2}. \tag{3.24}$$

Combining equations (3.23) and (3.24), the expanded-form of equation (3.4) takes the following description:

$$\frac{g_i(x_\alpha + e_{i\alpha}\Delta t, t + \Delta t) - g_i(x_\alpha, t)}{\Delta t} = \frac{\Omega_i(g_i)(x_\alpha + e_{i\alpha}\Delta t, t + \Delta t) + \Omega_i(g_i)(x_\alpha, t)}{2} \tag{3.25}$$

Introducing the following definitions,

$$\tilde{g}_i(x_\alpha, t) = g_i(x_\alpha, t) - \frac{\Omega_i(g_i)(x_\alpha, t)\Delta t}{2}$$

$$\tilde{g}_i(x_\alpha + e_{i\alpha}\Delta t, t + \Delta t) = g_i(x_\alpha + e_{i\alpha}\Delta t, t + \Delta t) - \frac{\Omega_i(g_i)(x_\alpha + e_{i\alpha}\Delta t, t + \Delta t)\Delta t}{2}, \tag{3.26}$$

equation (3.25) can be expressed as,

$$\tilde{g}_i(x_\alpha + e_{i\alpha}\Delta t, t + \Delta t) = \tilde{g}_i(x_\alpha, t) - \Omega_i(g_i)(x_\alpha, t)\Delta t. \tag{3.27}$$

Similar with the earlier case of fluid constituent, the Bhatnagar-Gross-Krook approximation was used in defining the discrete collision operator for thermal component, namely,

$$\Omega_i(g_i)(x_\alpha, t) = -\frac{1}{\tau_g} \left(g_i(x_\alpha, t) - g_i^{eq}(x_\alpha, t) \right), \tag{3.28}$$

where τ_g specifies the relaxation time for thermal population. Parameter g_i^{eq} portrays the thermal equilibrium population and is defined as

$$g_i^{eq} = z_i T \left(1 + \frac{e_{i\alpha}u_\alpha}{c_s^2} + \frac{(e_{i\alpha}u_\alpha)^2}{2c_s^4} - \frac{u_\alpha u_\beta}{2c_s^2} \right). \tag{3.29}$$

Quantity z_i designates the weighting coefficients for the thermal population.

Substituting equation (3.28) into (3.27), the following expression was captured:

$$\tilde{g}_i\left(x_\alpha + e_{i\alpha}\Delta t, t + \Delta t\right) = \tilde{g}_i\left(x_\alpha, t\right) - \frac{\Delta t}{\tau_g}\left(g_i\left(x_\alpha, t\right) - g_i^{eq}\left(x_\alpha, t\right)\right). \tag{3.30}$$

Then, combining equation (3.26) with (3.28), the following description prevailed:

$$g_i\left(x_\alpha, t\right) = \frac{2\tau_g\left(\tilde{g}_i\left(x_\alpha, t\right) + \frac{\Delta t}{2\tau_g} g_i^{eq}\left(x_\alpha, t\right)\right)}{2\tau_g + \Delta t}. \tag{3.31}$$

Finally, substituting equation (3.31) into (3.30), the second-order SRT (or BGK) lattice Boltzmann equation for the thermal constituent was obtained as

$$\tilde{g}_i\left(x_\alpha + e_{i\alpha}\Delta t, t + \Delta t\right) - \tilde{g}_i\left(x_\alpha, t\right) = -\frac{\Delta t}{\tilde{\tau}_g}\left(\tilde{g}_i\left(x_\alpha, t\right) - g_i^{eq}\left(x_\alpha, t\right)\right), \tag{3.32}$$

where $\tilde{\tau}_g$ is defined as

$$\tilde{\tau}_g = \tau_g + \frac{\Delta t}{2}. \tag{3.33}$$

Here, the thermal relaxation time $\tilde{\tau}_g$ is linked to the thermal diffusivity D as

$$D = c_s^2\left(\tilde{\tau}_g - \frac{\Delta t}{2}\right). \tag{3.34}$$

The associated collision and streaming steps for the thermal evolution equation occupy the following relationships:

Collision step:

$$\tilde{g}_i^*\left(x_\alpha, t\right) = \tilde{g}_i\left(x_\alpha, t\right) - \frac{\Delta t}{\tilde{\tau}_g}\left(\tilde{g}_i\left(x_\alpha, t\right) - g_i^{eq}\left(x_\alpha, t\right)\right). \tag{3.35}$$

Streaming step:

$$\tilde{g}_i\left(x_\alpha + e_{i\alpha}\Delta t, t + \Delta t\right) = \tilde{g}_i^*\left(x_\alpha, t\right).$$

At this point, the discrete lattice Boltzmann expressions for both fluid and thermal components have been established properly as equations (3.20) and (3.32), respectively. The corresponding relationships incorporate single relaxation time in their delineations, correspondingly depicted by $\tilde{\tau}_f$ and $\tilde{\tau}_g$. Such configurations were considered as the basic models for convective heat and mass transport modeling. Extension of this scheme is available by assimilating advanced model for both $\Omega_i(f_i)$ and $\Omega_i(g_i)$, in lieu of the Bhatnagar-Gross-Krook model. Such discussion is the topic of the forthcoming section.

2.3.2 Two-Relaxation-Time Lattice Boltzmann Model for Fluid and Thermal Components

The single-relaxation-time (SRT) lattice Boltzmann model developed in the previous section is generally suitable for the majority of convection heat and mass transfer phenomena considered in this study. However, such model suffers from unrealistically high computational demand when simulating rapid fluid flow and heat transfer cases, especially those incorporating high Rayleigh number (*Ra*). In this vein, the two-relaxation-time lattice Boltzmann model offers solution to overcome the shortcoming of SRT LBM model.

As the name implies, the two-relaxation-time (TRT) lattice Boltzmann model uses two relaxation times in approximating the discrete collision terms of the fluid and thermal populations, depicted accordingly by $\Omega_i(f_i)$ and $\Omega_i(g_i)$. The model was proposed by Irina Ginzburg (d'Humières and Ginzburg, 2009; Ginzburg *et al.*, 2008). In the present work, the standard TRT model was modified so as to establish a TRT scheme that occupies second-order accuracy in spatial and temporal coordinates.

In TRT framework, the relaxation time is decomposed into the symmetric and anti-symmetric fractions. Amongst them, one relaxation time is associated with the macroscopic quantity of the flow, while another relaxation time is a free parameter that can be tuned in order to control the accuracy and stability of simulation. This particular feature empowers TRT LBM scheme with superior flexibility in performing flow simulation than the earlier SRT LBM method. Hence, the drawback of SRT LBM in simulating high Rayleigh number cases can be overcome by the modified TRT LBM scheme.

For the fluid population, the TRT LBM scheme was derived by assigning the following expression for the discrete collision operator $\Omega_i(f_i)$, replacing the BGK model expressed in equation (3.12):

$$\Omega_i(f_i)(x_\alpha, t) = -\frac{1}{\tau_f^+}\left(f_i^+(x_\alpha, t) - f_i^{eq+}(x_\alpha, t)\right) - \frac{1}{\tau_f^-}\left(f_i^-(x_\alpha, t) - f_i^{eq-}(x_\alpha, t)\right). \qquad (3.36)$$

Here, f_i^+, f_i^{eq+} and τ_f^+ represent the symmetric part of the fluid population, equilibrium population and the relaxation time, respectively. Meanwhile, f_i^-, f_i^{eq-} and τ_f^- designate the anti-symmetric portion of the fluid population, equilibrium population and the relaxation time, accordingly. Consequently, the discrete forcing term R_i was also decomposed into corresponding symmetric and anti-symmetric parts, namely,

$$R_i(x_\alpha, t) = R_i^+(x_\alpha, t) + R_i^-(x_\alpha, t), \qquad (3.37)$$

where R_i^+ and R_i^- denote the symmetric and anti-symmetric portion of the forcing term, respectively. The following relationships prevail in TRT framework:

$$f_i\left(x_\alpha,t\right)=f_i^+\left(x_\alpha,t\right)+f_i^-\left(x_\alpha,t\right); \qquad f_i^{eq}\left(x_\alpha,t\right)=f_i^{eq+}\left(x_\alpha,t\right)+f_i^{eq-}\left(x_\alpha,t\right). \qquad (3.38)$$

Substituting equations (3.36) and (3.37) into equation (3.11), the following expression was captured:

$$\tilde{f}_i^* = \tilde{f}_i - \frac{\Delta t}{\tau_f^+}\left(f_i^+ - f_i^{eq+}\right) - \frac{\Delta t}{\tau_v^-}\left(f_i^- - f_i^{eq-}\right) + R_i^+\Delta t + R_i^-\Delta t. \qquad (3.39)$$

In the above relationship, the fraction which denote the dependence of a particular quantity upon spatial and temporal dimensions has been dropped. To simplify the mathematical operation, such approach will be implemented, hereinafter. Subsequently, parameters f_i^+ and f_i^- must be replaced by their concomitant second-order counterparts, namely $\tilde{f}_i^+$ and $\tilde{f}_i^-$. To find the expressions relating the former and latter parameters, equations (3.36) and (3.37) need to be substituted into equation (3.9). Associating relationships described in equation (3.38), the following remarks were obtained:

$$\begin{aligned}
f_i^+ &= \frac{2\tau_f^+\tilde{f}_i^+ + \Delta t f_i^{eq+} + \tau_f^+\Delta t R_i^+}{2\tau_f^+ + \Delta t} \\
f_i^- &= \frac{2\tau_f^-\tilde{f}_i^- + \Delta t f_i^{eq-} + \tau_f^-\Delta t R_i^-}{2\tau_f^- + \Delta t}.
\end{aligned} \qquad (3.40)$$

Substituting equation (3.40) into (3.39), the following annotations prevailed:

$$\tilde{f}_i^{*+} = \tilde{f}_i^+ - \frac{\Delta t}{\tau_f^+ + \dfrac{\Delta t}{2}}\left(\tilde{f}_i^+ - f_i^{eq+}\right) + \frac{\tau_f^+ R_i^+\Delta t}{\tau_f^+ + \dfrac{\Delta t}{2}} \qquad (3.41)$$

$$\tilde{f}_i^{*-} = \tilde{f}_i^- - \frac{\Delta t}{\tau_f^- + \dfrac{\Delta t}{2}}\left(\tilde{f}_i^- - f_i^{eq-}\right) + \frac{\tau_f^- R_i^-\Delta t}{\tau_f^- + \dfrac{\Delta t}{2}}. \qquad (3.42)$$

Based on the relationships described in equations (3.41) and (3.42), it is clear that

$$\tilde{f}_i^* = \tilde{f}_i^{*+} + \tilde{f}_i^{*-}. \qquad (3.43)$$

Finally, combining expressions in equations (3.41) and (3.42), the second-order TRT lattice Boltzmann scheme for fluid displacement was retrieved as

$$\tilde{f}_i^* = \tilde{f}_i - \frac{\Delta t}{\tilde{\tau}_f^+}\left(\tilde{f}_i^+ - f_i^{eq+}\right) - \frac{\Delta t}{\tilde{\tau}_f^-}\left(\tilde{f}_i^- - f_i^{eq-}\right) + \left(1 - \frac{\Delta t}{2\tilde{\tau}_f^+}\right)R_i^+\Delta t + \left(1 - \frac{\Delta t}{2\tilde{\tau}_f^-}\right)R_i^-\Delta t. \qquad (3.44)$$

Here, parameters $\tilde{\tau}_f^+$ and $\tilde{\tau}_f^-$ were defined as

$$\tilde{\tau}_f^+ = \tau_f^+ + \frac{\Delta t}{2}; \qquad \tilde{\tau}_f^- = \tau_f^- + \frac{\Delta t}{2}. \tag{3.45}$$

For the fluid population, the anti-symmetric relaxation time $\tilde{\tau}_f^-$ is free parameter while the symmetric relaxation time $\tilde{\tau}_f^+$ relates to the fluid kinematic viscosity υ as

$$\upsilon = c_s^2 \left(\tilde{\tau}_f^+ - \frac{\Delta t}{2} \right). \tag{3.46}$$

As a final annotation pertinent to the TRT model representing fluid constituent, the so-called magic parameter Λ_f (d'Humières and Ginzburg, 2009) was necessary to linked the symmetric and the anti-symmetric relaxation time. Such property is defined as

$$\Lambda_f = \left(\tilde{\tau}_f^+ - \frac{\Delta t}{2} \right)\left(\tilde{\tau}_f^- - \frac{\Delta t}{2} \right). \tag{3.47}$$

Previous investigation revealed that the optimum value of Λ_f is $1/12$ (Peng *et al.*, 2016). The following relationships apply to the proposed second-order TRT LBM scheme for fluid component:

$$\begin{aligned}
\tilde{f}_i^+ &= \frac{\tilde{f}_i + \tilde{f}_{\bar{i}}}{2}; & \tilde{f}_i^- &= \frac{\tilde{f}_i - \tilde{f}_{\bar{i}}}{2} \\
f_i^{eq+} &= \frac{f_i^{eq} + f_{\bar{i}}^{eq}}{2}; & f_i^{eq-} &= \frac{f_i^{eq} - f_{\bar{i}}^{eq}}{2},
\end{aligned} \tag{3.48}$$

where the subscript symbol $\bar{\imath}$ specifies opposite direction of i.

For the thermal population, the mathematical derivation of second-order TRT LBM for thermal populations adopts similar procedure as in the earlier fluid constituents. In this framework, the discrete collision operator for thermal constituent $\Omega_i(g_i)$ was identified as

$$\Omega_i(g_i) = -\frac{1}{\tau_g^+}\left(g_i^+ - g_i^{eq+} \right) - \frac{1}{\tau_g^-}\left(g_i^- - g_i^{eq-} \right), \tag{3.49}$$

where g_i^+, g_i^{eq+} and τ_g^+ denote the symmetric part of the thermal population, thermal equilibrium population and thermal relaxation time, respectively. Meanwhile, g_i^-, g_i^{eq-} and τ_g^- specify the anti-symmetric fraction of the thermal population, thermal equilibrium population and thermal relaxation time, accordingly. Substituting equation (3.49) into (3.27), the following expression was obtained:

$$\tilde{g}_i^* = \tilde{g}_i - \frac{\Delta t}{\tau_g^+}\left(g_i^+ - g_i^{eq+} \right) - \frac{\Delta t}{\tau_g^-}\left(g_i^- - g_i^{eq-} \right). \tag{3.50}$$

Subsequently, substituting equation (3.49) into (3.26), the following remarks emerged:

$$g_i^+ = \frac{2\tau_g^+ \tilde{g}_i^+ + \Delta t g_i^{eq+}}{2\tau_g^+ + \Delta t}; \qquad g_i^- = \frac{2\tau_g^- \tilde{g}_i^- + \Delta t g_i^{eq-}}{2\tau_g^- + \Delta t}. \tag{3.51}$$

Substituting equation (3.51) into (3.50), the following expressions prevailed:

$$\tilde{g}_i^{*+} = \tilde{g}_i^+ - \frac{\Delta t}{\tau_g^+ + \dfrac{\Delta t}{2}}\left(\tilde{g}_i^+ - g_i^{eq+}\right) \tag{3.52}$$

$$\tilde{g}_i^{*-} = \tilde{g}_i^- - \frac{\Delta t}{\tau_g^- + \dfrac{\Delta t}{2}}\left(\tilde{g}_i^- - g_i^{eq-}\right). \tag{3.53}$$

Finally, combining equations (3.52) and (3.53), the second-order TRT lattice Boltzmann scheme for thermal population was obtained as

$$\tilde{g}_i^* = \tilde{g}_i - \frac{\Delta t}{\tilde{\tau}_g^+}\left(\tilde{g}_i^+ - g_i^{eq+}\right) - \frac{\Delta t}{\tilde{\tau}_g^-}\left(\tilde{g}_i^- - g_i^{eq-}\right), \tag{3.54}$$

where parameters $\tilde{\tau}_g^+$ and $\tilde{\tau}_g^-$ occupy the following definitions, respectively:

$$\tilde{\tau}_g^+ = \tau_g^+ + \frac{\Delta t}{2}; \qquad \tilde{\tau}_g^- = \tau_g^- + \frac{\Delta t}{2}. \tag{3.55}$$

For thermal population, the symmetric relaxation time $\tilde{\tau}_g^+$ acts as the free-tuned parameter, while the anti-symmetric counterpart $\tilde{\tau}_g^-$ was tied to the thermal diffusion coefficient D, as described by:

$$D = c_s^2\left(\tilde{\tau}_g^- - \frac{\Delta t}{2}\right). \tag{3.56}$$

The associated magic parameter for thermal population is defined as

$$\Lambda_g = \left(\tilde{\tau}_g^+ - \frac{\Delta t}{2}\right)\left(\tilde{\tau}_g^- - \frac{\Delta t}{2}\right). \tag{3.57}$$

Similar with the erstwhile fluid population case, the optimum value of Λ_g was found to be $1/12$ (Peng *et al.*, 2016). The following remarks apply for the second-order thermal TRT LBM scheme:

$$\begin{aligned}
\tilde{g}_i^+ &= \frac{\tilde{g}_i + \tilde{g}_{\bar{i}}}{2}; & \tilde{g}_i^- &= \frac{\tilde{g}_i - \tilde{g}_{\bar{i}}}{2} \\
g_i^{eq+} &= \frac{g_i^{eq} + g_{\bar{i}}^{eq}}{2}; & g_i^{eq-} &= \frac{g_i^{eq} - g_{\bar{i}}^{eq}}{2}.
\end{aligned} \tag{3.58}$$

2.4 The Governing Mathematical Remarks and Principal Dimensionless Groups

The convective flow and heat transfer simulation conducted in this study is governed by three constitutive equations, namely, the continuity, Navier-Stokes, and heat equations, expressed as

$$\frac{\partial \rho}{\partial t} + \frac{\partial}{\partial x_\alpha}\left(\rho u_\alpha\right) = 0 \tag{3.59}$$

$$\frac{\partial}{\partial t}\left(\rho u_\alpha\right) + \frac{\partial}{\partial x_\beta}\left(\rho u_\alpha u_\beta\right) = -\frac{\partial p}{\partial x_\beta} + \mu \frac{\partial}{\partial x_\beta}\left(\frac{\partial u_\alpha}{\partial x_\beta} + \frac{\partial u_\beta}{\partial x_\alpha}\right) + F_\alpha \tag{3.60}$$

$$\frac{\partial T}{\partial t} + \frac{\partial}{\partial x_\alpha}\left(T u_\alpha\right) = \frac{\partial}{\partial x_\alpha}\left(D\frac{\partial T}{\partial x_\alpha}\right), \tag{3.61}$$

where ρ, u_i, p, T, μ and D denote the fluid density, velocity, pressure, temperature, dynamic viscosity, and thermal diffusion coefficient, respectively. Parameter F_α represents the contribution from the buoyancy force, which takes the following description:

$$F_\alpha = \rho G_\alpha \beta_T \left(T - T_{ref}\right), \tag{3.62}$$

where G_α specifies the gravitational acceleration, β_T depicts the thermal expansion coefficient, and T_{ref} designates the assigned reference temperature. The corresponding key dimensionless groups were identified as

$$Nu = \frac{hL}{\rho D c_p}; \qquad Pr = \frac{\upsilon}{D}; \qquad Ra = \frac{G_y \beta_T \left(T_{hot} - T_{cold}\right)L^3}{\upsilon D}, \tag{3.63}$$

where Nu, Pr, and Ra designate the Nusselt, Prandtl, and Rayleigh number, accordingly. T_{hot} and T_{cold} denote the hot and cold temperature conditions, respectively. Physical quantities of h, c_p, and L represent, respectively, the heat transfer coefficient, fluid specific heat capacity, and the characteristic length of the domain. The generic dimensionless parameters were defined as:

$$x^* = \frac{x}{L}; \qquad y^* = \frac{y}{L}; \qquad u_\alpha^* = \frac{u_\alpha L}{D}. \tag{3.64}$$

Here, x and y express, respectively, the horizontal and vertical length of the investigated domain.

2.5   Introduction to the Chapman-Enskog Analysis

At this point, it is clear that LBM adopts unique approach in its operation in which numerical solutions of equation (3.59) - (3.61) are obtained through finding solutions of different equations, namely the representative Boltzmann equations. This particular characteristic contradicts the customary approach. As such, in order for this approach to be reliable, there must be a specific way to connect the representative Boltzmann equations with the prevalent hydrodynamics formulations.

Such relationship can be revealed by evaluating the Chapman-Enskog analysis (Kruger *et al.*, 2017; Silva and Semiao, 2012).

Principally, the Chapman-Enskog analysis is administered by expanding the representative lattice Boltzmann equations of fluid and thermal components in Taylor series around the corresponding equilibrium populations. Integrating the expanded equations for all the associated particles allows one to recover the fundamental macroscopic relationships. Detail discussions regarding the Chapman-Enskog analysis used in this study will be postponed to the next chapter of this treatise. As can be seen in later chapter, the Chapman-Enskog analysis allows one to see the connection between the representative Boltzmann equations and the prevalent macroscopic relationships of equation (3.59) - (3.61).

2.6 Discrete Lattice Velocity Set in Lattice Boltzmann Simulation

The concept of discrete lattice velocity ties closely to the streaming step of the lattice Boltzmann algorithm. After undergoing collision, the particles will propagate within the domain following discrete directions which are determined by the assigned discrete lattice velocity set for the dynamical system at hand.

Principally, the discrete velocity set in LBM is represented by the symbol DdQq (Kruger *et al.*, 2017; Mohamad, 2019; Sukop and Thorne, 2006). It manifests d-number of dimensions and q-available direction of movements. As an example, simulation in two-dimensional domain incorporating nine discrete plausible direction of movements will be prescribed as D2Q9 velocity set. The present study assimilates D2Q9 and D2Q5 velocity arrangements to simulate fluid and thermal movements, respectively. Figure 2.2 demonstrates the schematic illustration of the D2Q9 and D2Q5 velocity set.

For the D2Q9 velocity arrangement, there are nine possible directions of particles' movements, including those that are stationary. Such configuration satisfies the following conditions:

$$\xi_{i\alpha} = \begin{cases} (0,0), & \text{for } i = 0 \\ (1,0),(0,1),(-1,0),(0,-1), & \text{for } i = 1,2,3,4 \\ (1,1),(-1,1),(-1,-1),(1,-1), & \text{for } i = 5,6,7,8 \end{cases} \qquad (3.65)$$
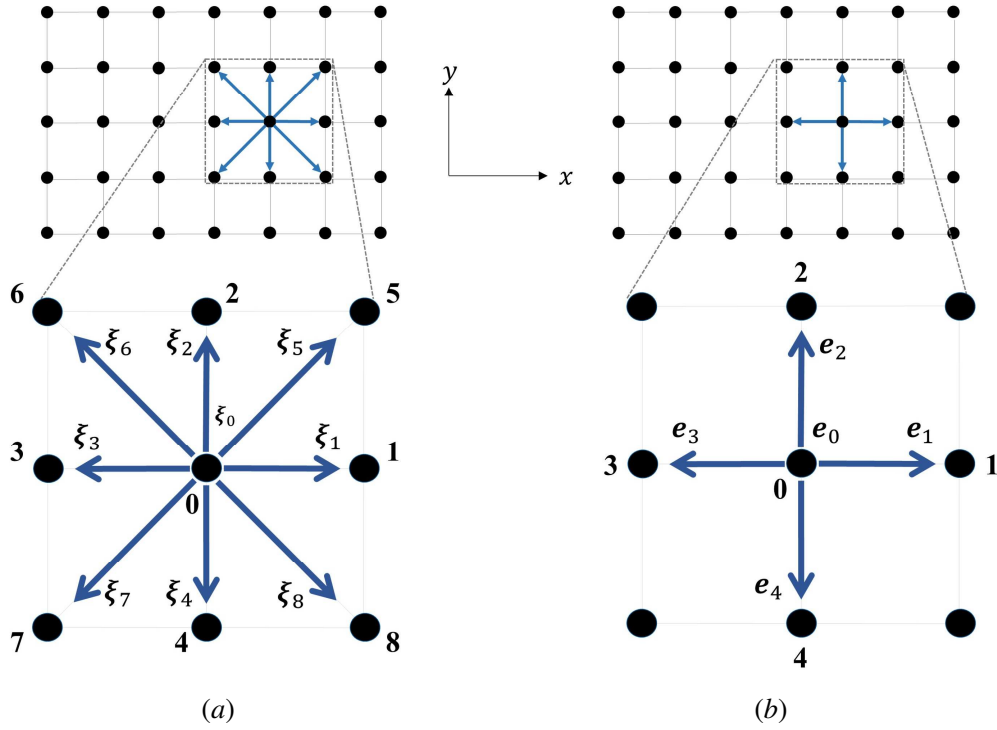
Figure 2.2. Schematic illustration of discrete velocity sets in lattice Boltzmann simulation, showing (a) D2Q9 and (b) D2Q5 velocity set.

$$w_i = \begin{cases} \dfrac{4}{9}, & \text{for } i = 0 \\ \dfrac{1}{9}, & \text{for } i = 1, 2, 3, 4 \\ \dfrac{1}{36}, & \text{for } i = 5, 6, 7, 8. \end{cases} \tag{3.66}$$

In the above formulation, w_i specifies the weighting coefficients for the density population appeared in equation (3.13).

On the other hand, the D2Q5 velocity set comprises five possible direction of movements. For this particular discrete lattice arrangement, the following conditions prevail:

$$e_{i\alpha} = \begin{cases} (0,0), & \text{for } i = 0 \\ (1,0),(0,1),(-1,0),(0,-1), & \text{for } i = 1, 2, 3, 4 \end{cases} \tag{3.67}$$

$$z_i = \begin{cases} \dfrac{2}{6}, & \text{for } i = 0 \\[2mm] \dfrac{1}{6}, & \text{for } i = 1, 2, 3, 4. \end{cases} \tag{3.68}$$

Here, represents the weighting factors for the thermal populations appeared in equation (3.29).

2.7 Treatment of Initial and Boundary Conditions in Lattice Boltzmann Method

2.7.1 Implementation of Initial Condition in Lattice Boltzmann Method

In any CFD techniques, initial condition is mandatory to be defined prior to running the simulation. In LBM, initial conditions for fluid density and velocity are typically prescribed in stationary condition as:

$$\rho\left(x_\alpha, t = 0\right) = 1; \qquad u_\alpha\left(x_\alpha, t = 0\right) = 0. \tag{3.69}$$

Meanwhile, initial condition for temperature is assigned following the appointed thermal condition at the corresponding walls of the domain.

2.7.2 Implementation of Boundary Condition in Lattice Boltzmann Method

LBM adopts indirect approach in defining the boundary conditions. As such, the macroscopic properties at the boundaries have to be decomposed into their representative distribution functions. The operation includes decomposition of distribution functions into known an unknown populations at a particular boundary (Kruger *et al.*, 2017; Mohamad, 2019; Sukop and Thorne, 2006). Figure 2.3 illustrates the corresponding notion. Therein, the D2Q9 discrete velocity set was selected to exemplify the concept. In the figure, the known and unknown distribution functions at the respective walls were represented by the blue and red colors, respectively. To elaborate the situation at the particular boundary, the condition at the left-boundary wall was considered further.
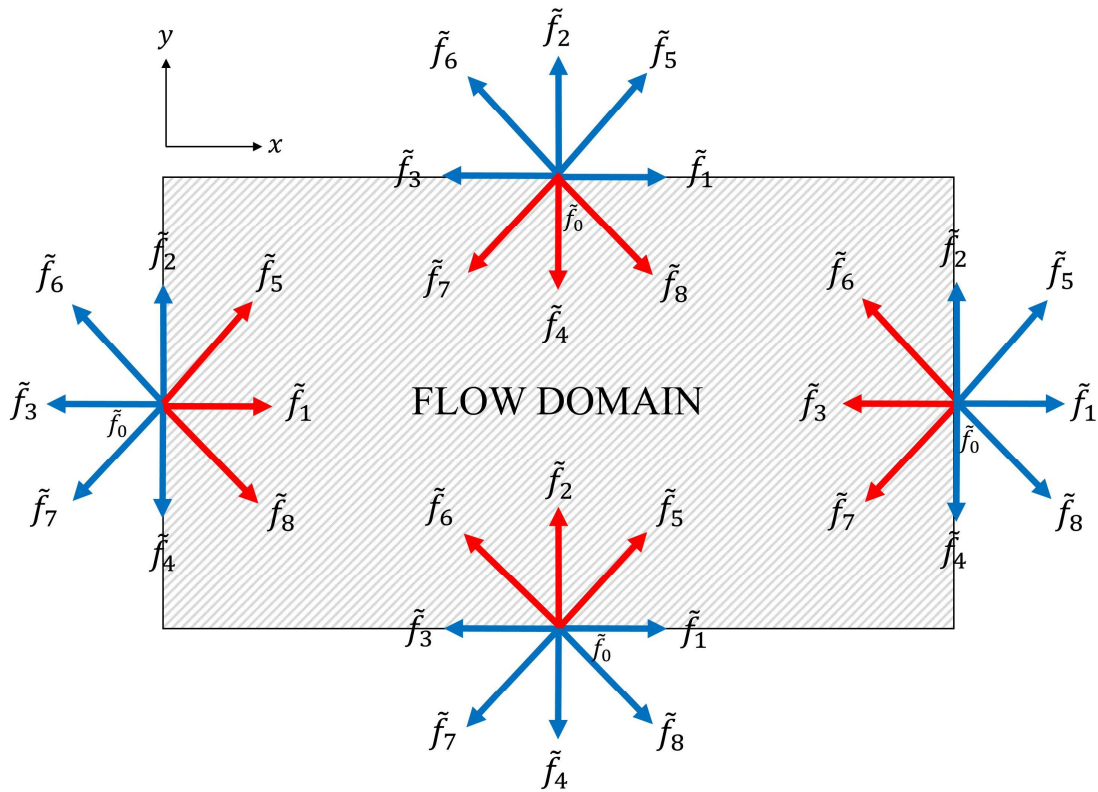
Figure 2.3. Boundary conditions in LBM for the vertical and horizontal walls, displaying the known distributions (blue color) and the unknown distribution (red color).

Figure 2.4 demonstrates condition at the central boundary node of the left-perimeter. Therein, the right-side of the particular boundary node is the fluid region, while the opposite side is the solid region. Considering Figure 2.4(*a*), during streaming step, the right-neighbor side of fluid node contributes upon propagating the $\tilde{f}_3$ population towards the central node of interest. Equivalently, the neighboring node at the top-right side delivers the $\tilde{f}_7$ population towards the selected central boundary node. Similar situations occur upon all neighboring fluid nodes with their own associated populations.
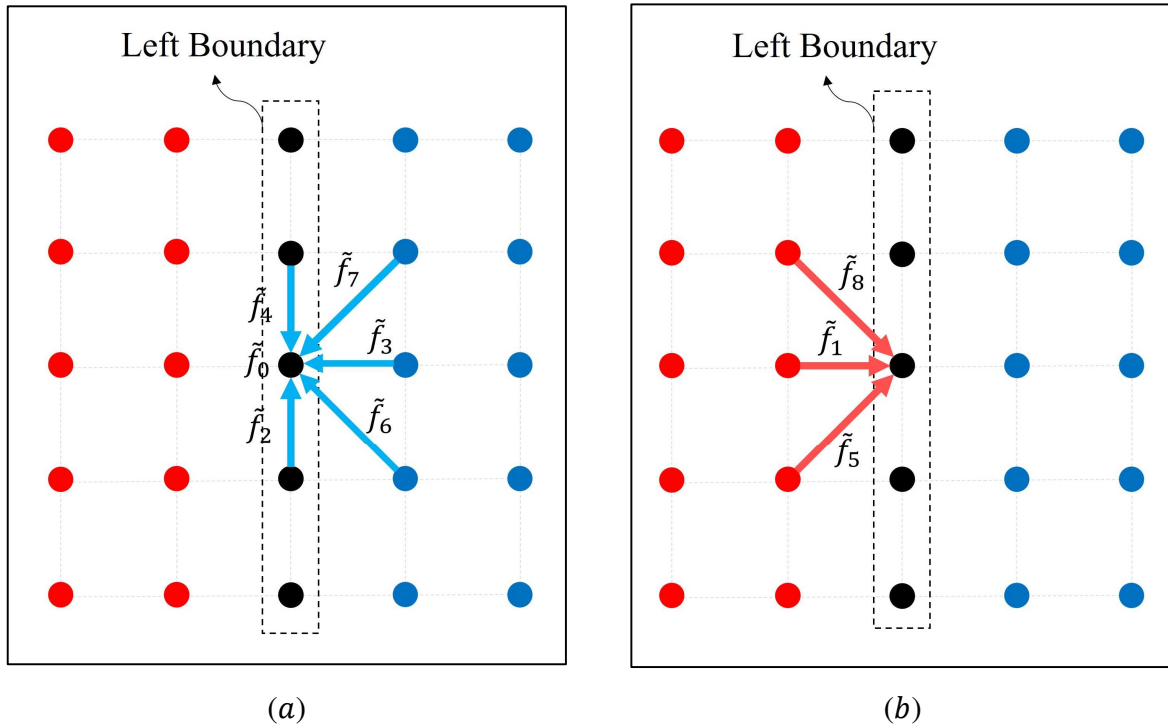
Figure 2.4. (*a*) The known and (*b*) unknown distribution functions at the left boundary. The associated solid, fluid and boundary nodes were displayed using red, blue and black colors, respectively.

The streamed-populations from the neighboring fluid nodes constitute the known populations at the selected central boundary node, namely the $\tilde{f}_2, \tilde{f}_3, \tilde{f}_4, \tilde{f}_6$, and $\tilde{f}_7$ populations. Considering that the stationary population $\tilde{f}_0$ also exist within the boundary of interest, a total of six distribution functions were defined therein.

Figure 2.4(*b*) demonstrates the streamed-populations from the neighboring solid nodes towards the boundary node of interest. Because the neighboring solid nodes do not possess any contributions to the fluid flow, then the corresponding populations were essentially non-existent. Therefore, the $\tilde{f}_1$, $\tilde{f}_5$ and $\tilde{f}_8$ populations were unknown at the particular node of interest. Similar situation applies to the other boundary walls, establishing the known and unknown distribution functions for each appropriate boundaries.

Therefore, the principal idea of boundary treatments in LBM is to find out expressions for the unknown populations at boundary walls. The present work administers two commonly implemented boundary strategies in LBM, namely the bounce-back and the non-equilibrium bounce-back methods.

For the bounce-back (BB) approach, the unknown populations at a particular boundary are determined from the known populations by implementing bounce-back scenario. Here, the population leaving a particular fluid node towards a specific boundary node is reflected back into the original fluid node.

Figure 2.5 illustrates the concept of BB method. During streaming step, a particular population $\tilde{f}_i$ is leaving the fluid node towards the boundary node. Upon reaching the boundary node, the population was reflected back into the original fluid node. Since the reflected population now possesses opposite direction of movement, the population is now identified as $\tilde{f}_{\bar{\imath}}$, in which the symbol $\bar{\imath}$ is used to denote the direction opposite of i.
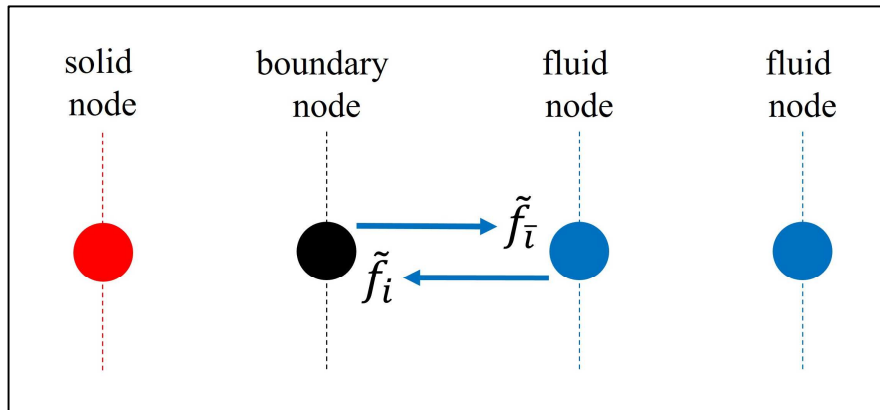
Figure 2.5. Bounce-back boundary method in LBM.

Such operation satisfies the following rule:

$$\tilde{f}_{\bar{\imath}}\left(x_{\alpha,\text{boundary}}, t + \Delta t\right) = \tilde{f}_i^*\left(x_{\alpha,\text{boundary}}, t\right). \tag{3.70}$$

Here, $x_{\alpha,\text{boundary}}$ designates the location of the boundary within the flowing domain. The term on the right-side of the equation manifests the condition of populations after collision step was performed. Therefore, for the corresponding left-boundary wall case, the unknown populations were configured as

$$\tilde{f}_1\left(x_{\alpha,left},t+\Delta t\right)=\tilde{f}_3^*\left(x_{\alpha,left},t+\Delta t\right)$$

$$\tilde{f}_5\left(x_{\alpha,left},t+\Delta t\right)=\tilde{f}_7^*\left(x_{\alpha,left},t+\Delta t\right) \tag{3.71}$$

$$\tilde{f}_8\left(x_{\alpha,left},t+\Delta t\right)=\tilde{f}_6^*\left(x_{\alpha,left},t+\Delta t\right).$$

In the above expression, $x_{\alpha,\text{left}}$ specifies the left-boundary position. The unknown populations at other boundary positions, as well as at the boundary corners, can be determined following similar manner.

Aside from the bounce-back scheme, there is another technique for implementing boundary conditions in LBM, namely the non-equilibrium bounce back (NEBB) method. Such technique was proposed by Zou and He (Zou and He, 1997). The technique was based upon the fulfillment of conservation of mass and momentum as well as the non-equilibrium conditions at the boundaries. Different from the earlier scenario, NEBB method necessitates additional computations at the boundary in order to retrieve the expressions for the unknown populations. Taking similar boundary location as in the previous technique as an exemplification, the unknown parameters at the left-boundary wall is determined as

$$\rho_{left}=\frac{1}{1-u_{x,\text{left}}}\left(\tilde{f}_0+\tilde{f}_2+\tilde{f}_4+2\left(\tilde{f}_3+\tilde{f}_6+\tilde{f}_7\right)-\frac{1}{2}F_x\right)$$

$$\tilde{f}_1=\tilde{f}_3+\frac{2}{3}\rho_{left}u_{x,\text{left}}-\frac{1}{6}F_x$$

$$\tilde{f}_5=\tilde{f}_7-\frac{1}{2}\left(\tilde{f}_2-\tilde{f}_4\right)+\frac{1}{6}\rho_{left}u_{x,\text{left}}+\frac{1}{2}\rho_{left}u_{y,\text{left}}-\frac{1}{6}F_x-\frac{1}{4}F_y \tag{3.72}$$

$$\tilde{f}_8=\tilde{f}_6+\frac{1}{2}\left(\tilde{f}_2-\tilde{f}_4\right)+\frac{1}{6}\rho_{left}u_{x,\text{left}}-\frac{1}{2}\rho_{left}u_{y,\text{left}}-\frac{1}{6}F_x+\frac{1}{4}F_y.$$

The unknown parameters for other boundary locations can be determined following similar manner.

For thermal population, the anti-bounce back (ABB) technique (Kruger *et al.*, 2017) is typically implemented. Such method was administered as

$$\tilde{g}_{\bar{i}}\left(x_{\text{boundary}},t+\Delta t\right)=-\tilde{g}_i^*\left(x_{\text{boundary}},t\right)+2z_iT_{\text{wall}}, \tag{3.73}$$

where T_{wall} notifies the prescribed temperature condition at particular boundary wall.

2.8 A Preliminary Application of Modified LBM Scheme for Two-Dimensional Differentially-Heated Cavity

In order to test the modified LBM scheme, the corresponding algorithm was used to simulate convective flow and heat transfer in a two-dimensional differentially-heated cavity. Figure 2.6 schematized the configuration of the problem at hand.
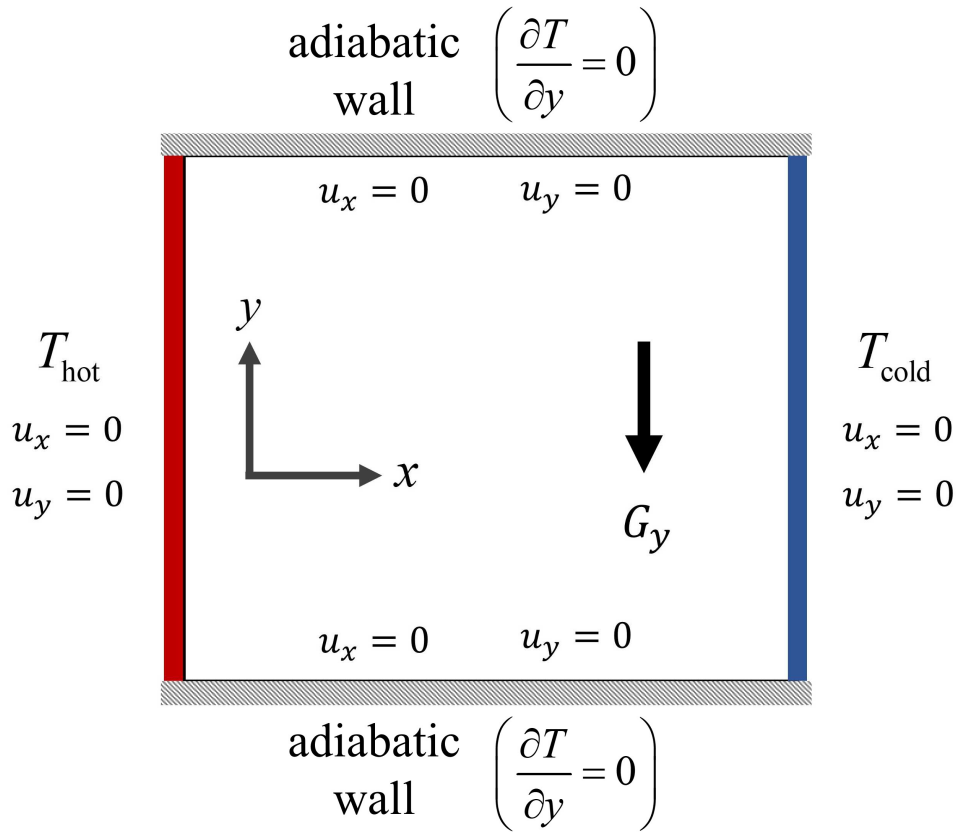
Figure 2.6. Domain configuration for two-dimensional natural convection in a differentially-heated cavity.

The entire domain was initially filled with a stationary fluid. The vertical walls of the cavity were characterized by contrasting thermal conditions. The left-vertical wall was set to be warmer than the opposing right-wall. The horizontal boundaries were set to be perfectly insulated. The NEBB method was adopted for the fluid population, while thermal population follows the ABB method. The simulation was conducted for varying Rayleigh number of $10^3 \leq Ra \leq 10^7$. Low Rayleigh number flows of $10^3 \leq Ra \leq 10^4$ were simulated using the second-order SRT model, while flows of $10^5 \leq Ra \leq 10^7$ were simulated using the second-order TRT model. The simulation adheres to the constitutive relationships described by equations (3.59) - (3.64).

Figure 2.7 demonstrates the streamlines and isotherms at steady-state condition for $Ra = 10^3$ and $Ra = 10^4$, while Figure 2.8 presents the conditions for $Ra = 10^5$ and $Ra = 10^6$. The simulation results for $Ra = 10^7$ were displayed in Figure 2.9.
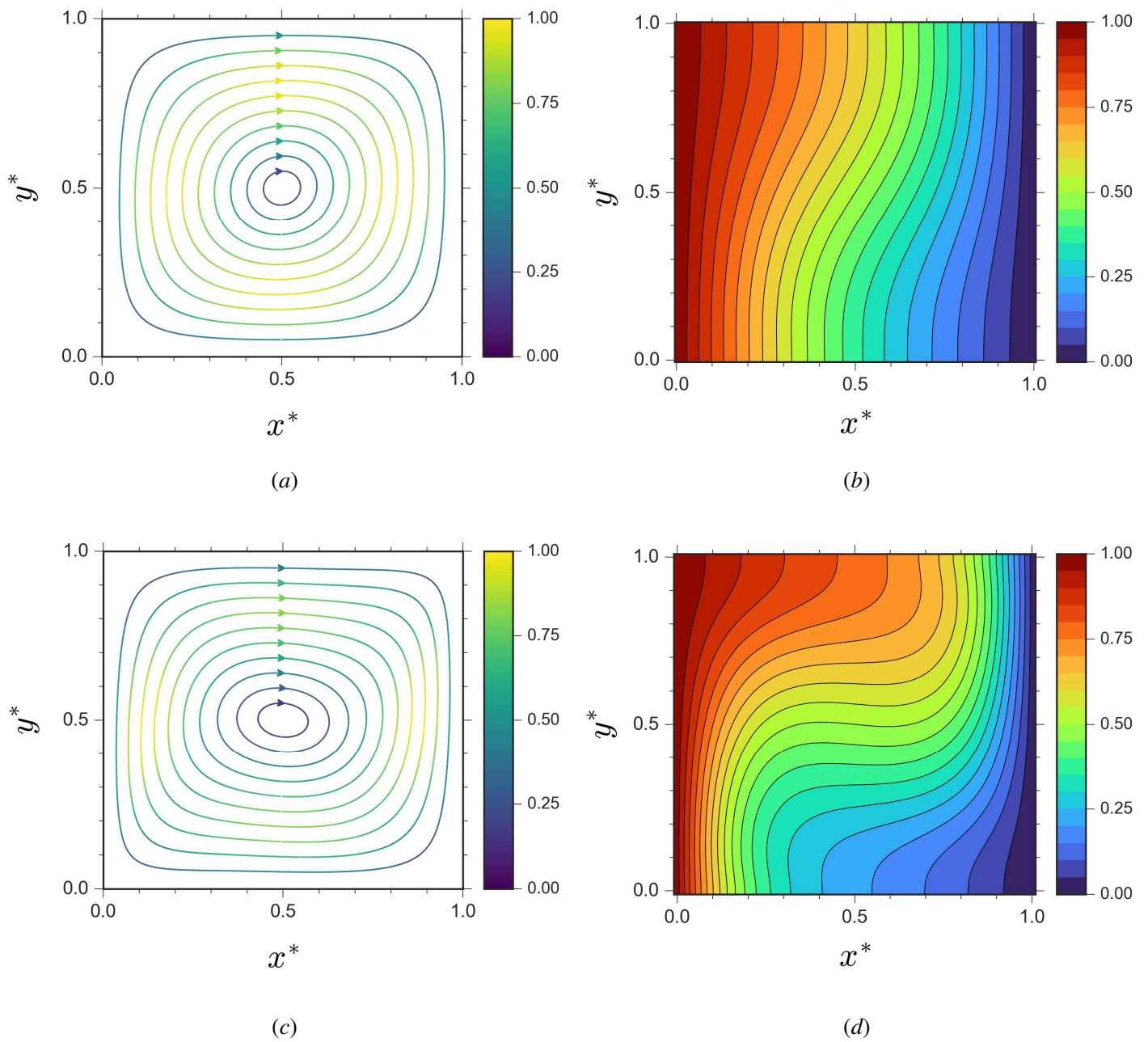
Figure 2.7. Simulation results of natural convection and heat transfer in a differentially-heated cavity using second-order SRT LBM scheme, displaying (*a*) streamlines for $Ra = 10^3$, (*b*) isotherms for $Ra = 10^3$, (*c*) streamlines for $Ra = 10^4$, and (*d*) isotherms for $Ra = 10^4$.
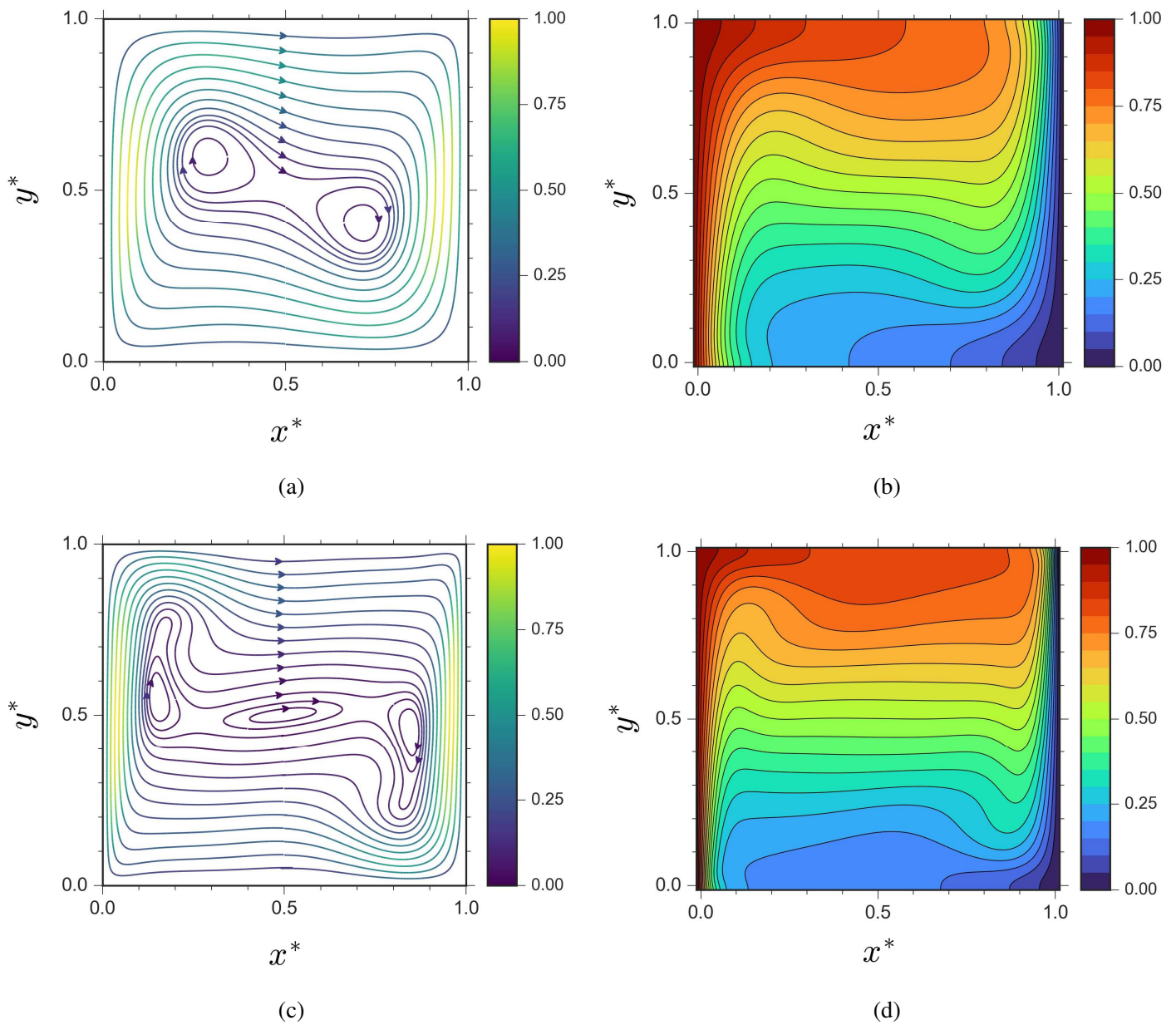
Figure 2.8. Simulation results of natural convection and heat transfer in a differentially-heated cavity using second-order TRT LBM scheme, displaying (a) streamlines for $Ra = 10^5$, (b) isotherms for $Ra = 10^5$, (c) streamlines for $Ra = 10^6$, and (d) isotherms for $Ra = 10^6$.
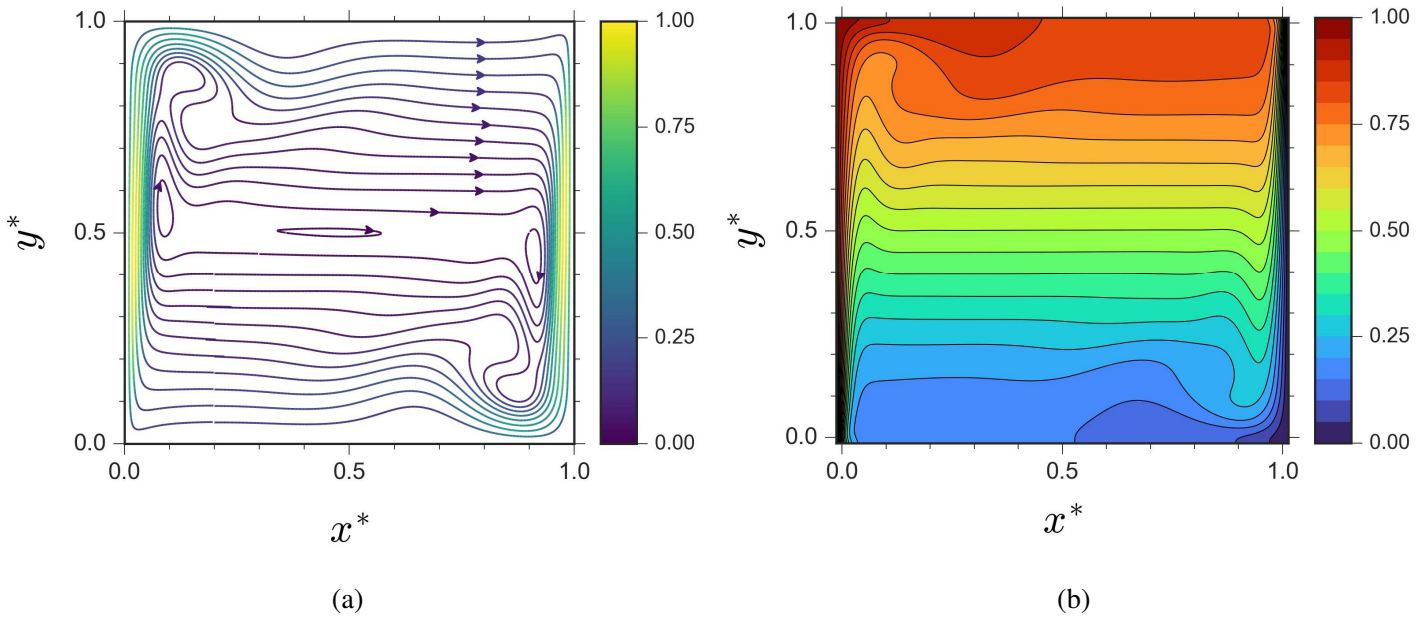
Figure 2.9. Simulation results of natural convection and heat transfer in a differentially-heated cavity using second-order TRT LBM scheme, displaying (a) streamlines for $Ra = 10^7$ and (b) isotherms for $Ra = 10^7$.

All the recovered velocity and temperature contours from the present study display excellent agreement with previous researches of Dixit and Babu (2006), Du and Liu (2013), Mayne *et al.* (2000), Shu *et al.* (2002), De Vahl Davis (1983), and Yu and Tian (2012). Table 2.1 outlines the comparison of average Nusselt numbers obtained from the present simulation with previous studies. The results show very good agreement for the associated range of Rayleigh numbers. Hence, it can be deduced that the proposed LBM scheme in this study occupies reliable capacity in simulating convective flow and heat transfer phenomena.

Table 2.1. Comparison of average Nusselt number at steady-state condition with previous studies.

Rayleigh Number	LBM Scheme (Present Study)	Dixit and Babu (2006)	Yu and Tian (2012)	Du and Liu (2013)
10^3	1.110	1.121	1.118	1.108
10^4	2.237	2.286	2.244	2.252
10^5	4.522	4.546	4.520	4.596
10^6	8.840	8.652	8.804	8.822
10^7	16.566	16.790	16.298	16.424

Chapter 3: Comparison Study of Modified LBM Scenario with Previous LBM Scenarios under Unsteady Thermal Convection Flow and Heat Transfer Simulation

3.1 Diverse Lattice Boltzmann Schemes in Convective Fluid Flow and Heat Transfer

As far as modeling concurrent heat and mass transfer problem using lattice Boltzmann method (LBM) is concerned, two properties are routinely considered: (a) the discrete LBM modeling and (b) the discrete forcing schemes. Considering both factors, the LBM scenarios offer few possible scenarios to conduct thermal convective flow and heat transfer. However, choosing a suitable approach is still a matter of debate. In this study, two different lattice Boltzmann equations and three distinct forcing models have been studied and compared to figure out the discrepancy in simulation performance between them. Within the framework of the single-relaxation-time (SRT) LBM model, two non-isothermal thermo-hydrodynamics systems, namely natural convection in a differentially-heated cavity and Rayleigh-Bènard convection, were selected as the physical platforms to test the diverse LBM scenarios.

3.1.1 First- and Second-Order Accurate Lattice Boltzmann Models

The present study proposes the modified LBM scenario that occupies second-order accuracy in spatial and temporal coordinates. The standard LBM, however, inhabits first-order accuracy in space and time. As such, two different manifestations of flowing entities prevail in LBM, namely the first- and the second-order accurate LBM scenarios.

In the framework of the standard first-order accurate LBM scenario, the fluid and thermal materials are represented by the following remarks, respectively:

$$f_i\left(x_\alpha + \xi_{i\alpha}\Delta t, t + \Delta t\right) - f_i\left(x_\alpha, t\right) = -\frac{\Delta t}{\tau_f}\left(f_i\left(x_\alpha, t\right) - f_i^{eq}\left(x_\alpha, t\right)\right) + R_i\left(x_\alpha, t\right)\Delta t \qquad (5.1)$$

$$g_i\left(x_\alpha + e_{i\alpha}\Delta t, t + \Delta t\right) - g_i\left(x_\alpha, t\right) = -\frac{\Delta t}{\tau_g}\left(g_i\left(x_\alpha, t\right) - g_i^{eq}\left(x_\alpha, t\right)\right). \qquad (5.2)$$

Here, all the associated parameters occupy similar definitions as shown in chapter 2. On the other hand, the modified LBM scenario by considering second-order accurate LBM takes the description of equations (2.20) and (2.32) for the fluid and thermal components, respectively. For convenience, both equations are rewritten here as

$$\tilde{f}_i\left(x_\alpha + \xi_{i\alpha}\Delta t, t + \Delta t\right) - \tilde{f}_i\left(x_\alpha, t\right) = -\frac{\Delta t}{\tilde{\tau}_f}\left(\tilde{f}_i\left(x_\alpha, t\right) - f_i^{eq}\left(x_\alpha, t\right)\right) + \left(1 - \frac{\Delta t}{2\tilde{\tau}_f}\right)R_i\left(x_\alpha, t\right)\Delta t \quad (5.3)$$

$$\tilde{g}_i\left(x_\alpha + e_{i\alpha}\Delta t, t + \Delta t\right) - \tilde{g}_i\left(x_\alpha, t\right) = -\frac{\Delta t}{\tilde{\tau}_g}\left(\tilde{g}_i\left(x_\alpha, t\right) - g_i^{eq}\left(x_\alpha, t\right)\right). \quad (5.4)$$

Similarly, all the pertinent quantities in equations (5.3) and (5.4) are defined in chapter 2.

A careful inspection upon equations (5.1) - (5.4) reveals that the representative discrete Boltzmann equations for the first- and second-order LBM scenarios display dissimilar mathematical form. As such, it seems conceivable to expect dissimilarity in the computational performance from each model in simulating thermal convective flow and heat transfer phenomena. It has been challenged further by the presence of distinct models related to the discrete forcing terms R_i. The latter subject is discussed in more detail in the upcoming section.

3.1.2 Discrete Forcing Simulation for LBM

The discrete forcing term R_i appears in the representative Boltzmann equations for the fluid population, as displayed in equations (5.3) and (5.4). In this framework, there exist different mathematical expressions for R_i. In this study, three prominent mathematical models for the discrete forcing term R_i were considered, namely the scheme proposed by Luo (2000), Guo et al. (2002), and Kupershtokh et al. (2009), expressed respectively as

$$R_i = w_i\left(\frac{\xi_{i\alpha}F_\alpha}{c_s^2}\right) \quad (5.5)$$

$$R_i = w_i\left(\frac{\xi_{i\alpha} - u_\alpha}{c_s^2} + \frac{\left(\xi_{i\alpha}u_\alpha\right)\xi_{i\alpha}}{c_s^4}\right)F_\alpha \quad (5.6)$$

$$R_i = f_i^{eq}\left(\rho, u_\alpha + \Delta u_\alpha\right) - f_i^{eq}\left(\rho, u_\alpha\right). \quad (5.7)$$

In the above formulations, F_α depicts the buoyancy force.

3.1.3 Disparate LBM scenarios for Unsteady Convective Flow and Heat Transfer

From the erstwhile explanations, it is therefore apparent that there exist distinct scenarios in simulating natural convection and heat transfer with LBM based on the available combinations of

discrete order and forcing for LBM scenarios. Table 3.1 outlines the plausible LBM scenarios considered in the present study. Hereinafter, the devised LBM scenario listed in the first-column of Table 3.1 will be referred in the forthcoming analysis.

Table 3.1. The plausible arrangements for simulating the buoyancy-driven natural convection flow with LBM scenarios.

LBM Scenarios	Order	Discrete Forcing
IA IB IC	First-Order (Equations (5.1) and (5.2))	Luo (Equation (5.5)) Guo et al. (Equation (5.6)) Kupershtokh et al. (Equation (5.7))
IIA IIB IIC	Second-Order (Equations (5.3) and (5.4))	Luo (Equation (5.5)) Guo et al. (Equation (5.6)) Kupershtokh et al. (Equation (5.7))

3.2 Chapman-Enskog Analysis of Disparate LBM scenarios

As was discussed briefly in section 2.5, the Chapman-Enskog analysis occupies indispensable role in LBM scenarios. It provides a firm theoretical foundation to see the connection between the representative Boltzmann equations for the flowing entities and their concomitant macroscopic thermo-hydrodynamics expressions. Moreover, the evaluation is pivotal to disclose the capacity of each considered LBM scenarios in returning the fundamental macroscopic relationships. The present section was devoted to elaborate the Chapman-Enskog analysis for the associated fluid and thermal populations. The evaluation was conducted within the framework of the SRT LBM model for both first- and second-order schemes.

3.2.1 Chapman-Enskog Analysis for Fluid Component

The Chapman-Enskog analysis for the fluid population was commenced by establishing the following definitions pertinent to variables that will be used throughout the evaluation:

$$\zeta_i = f_i^{eq} + \epsilon \zeta_i^{(1)} + \epsilon^2 \zeta_i^{(2)}$$

$$\frac{\partial}{\partial t} = \epsilon \frac{\partial}{\partial t_1} + \epsilon^2 \frac{\partial}{\partial t_2}$$

$$\xi_{i\alpha} \frac{\partial}{\partial x_\alpha} = \epsilon \xi_{i\alpha} \frac{\partial}{\partial x_\alpha^{(1)}} + \epsilon^2 \xi_{i\alpha} \frac{\partial}{\partial x_\alpha^{(2)}}$$

$$R_i = \epsilon R_i^{(1)}.$$

(5.8)

Here, ϵ denotes small quantity which value lies within the order of Knudsen number. The pseudo-quantity ζ_i was defined as

$$\zeta_i = \begin{cases} f_i, & \text{for scenario IA, IB and IC} \\ \tilde{f}_i, & \text{for scenario IIA, IIB and IIC.} \end{cases} \tag{5.9}$$

Substituting equation (2.12) into equation (2.2), as well as associating the general expression of the fluid population defined in equation (5.9), the generalized discrete forms of the representative Boltzmann equations encompassing the first- and second-order schemes were configured as

$$\frac{\partial \zeta_i}{\partial t} + \xi_{i\alpha} \frac{\partial \zeta_i}{\partial x_\alpha} = -\frac{1}{\sigma}\left(\zeta_i - f_i^{eq}\right) + \varphi R_i, \tag{5.10}$$

where σ and φ were defined as

$$\sigma = \begin{cases} \tau_f, & \text{for scenario IA, IB and IC} \\ \tilde{\tau}_f, & \text{for scenario IIA, IIB and IIC.} \end{cases} \tag{5.11}$$

$$\varphi = \begin{cases} 1, & \text{for scenario IA, IB and IC} \\ \left(1 - \dfrac{\Delta t}{2\tilde{\tau}_f}\right), & \text{for scenario IIA, IIB and IIC.} \end{cases} \tag{5.12}$$

Adopting Taylor series expansion upon equation (5.10), the following remarks prevailed:

$$\begin{aligned} \mathrm{O}(\cdot): \quad & \left(\frac{\partial}{\partial t_1} + \xi_{i\alpha} \frac{\partial}{\partial x_\alpha^{(1)}}\right) f_i^{eq} = -\frac{1}{\sigma} \zeta_i^{(1)} + \varphi R_i^{(1)} \\ \mathrm{O}(\cdot^2): \quad & \left(\frac{\partial}{\partial t_2} + \xi_{i\alpha} \frac{\partial}{\partial x_\alpha^{(2)}}\right) f_i^{eq} + \left(\frac{\partial}{\partial t_1} + \xi_{i\alpha} \frac{\partial}{\partial x_\alpha^{(1)}}\right)\left(\left(1 - \frac{\Delta t}{2\sigma}\right)\zeta_i^{(1)} + \frac{\Delta t}{2}\varphi R_i^{(1)}\right) = -\frac{1}{\sigma}\zeta_i^{(2)}. \end{aligned} \tag{5.13}$$

Here, $\mathrm{O}(\epsilon)$ and $\mathrm{O}(\epsilon^2)$ specify respectively the first- and second-order Taylor-expansion terms of equation (5.10). Thereupon, the moments of $\mathrm{O}(\epsilon)$ and $\mathrm{O}(\epsilon^2)$ can be obtained as

Moments of $\mathrm{O}(\epsilon)$:

$$\begin{aligned} \sum_i \left(\frac{\partial}{\partial t_1} + \xi_{i\alpha} \frac{\partial}{\partial x_\alpha^{(1)}}\right) f_i^{eq} &= \sum_i \left(-\frac{1}{\sigma}\zeta_i^{(1)} + \varphi R_i^{(1)}\right) \\ \sum_i \xi_{i\alpha} \left(\frac{\partial}{\partial t_1} + \xi_{i\alpha} \frac{\partial}{\partial x_\alpha^{(1)}}\right) f_i^{eq} &= \sum_i \xi_{i\alpha}\left(-\frac{1}{\sigma}\zeta_i^{(1)} + \varphi R_i^{(1)}\right) \\ \sum_i \xi_{i\alpha}\xi_{i\beta} \left(\frac{\partial}{\partial t_1} + \xi_{i\alpha} \frac{\partial}{\partial x_\alpha^{(1)}}\right) f_i^{eq} &= \sum_i \xi_{i\alpha}\xi_{i\beta}\left(-\frac{1}{\sigma}\zeta_i^{(1)} + \varphi R_i^{(1)}\right) \end{aligned} \tag{5.14}$$

Moments of $O(\epsilon^2)$:

$$\sum_i \left(\frac{\partial}{\partial t_2} + \xi_{i\alpha} \frac{\partial}{\partial x_\alpha^{(2)}} \right) f_i^{eq} + \sum_i \left(\frac{\partial}{\partial t_1} + \xi_{i\alpha} \frac{\partial}{\partial x_\alpha^{(1)}} \right) \left(1 - \frac{\Delta t}{2\sigma} \right) \zeta_i^{(1)}$$

$$+ \sum_i \left(\frac{\partial}{\partial t_1} + \xi_{i\alpha} \frac{\partial}{\partial x_\alpha^{(1)}} \right) \frac{\Delta t}{2} \varphi R_i^{(1)} = -\frac{1}{\sigma} \sum_i \zeta_i^{(2)}$$

$$\sum_i \xi_{i\alpha} \left(\frac{\partial}{\partial t_2} + \xi_{i\alpha} \frac{\partial}{\partial x_\alpha^{(2)}} \right) f_i^{eq} + \sum_i \xi_{i\alpha} \left(\frac{\partial}{\partial t_1} + \xi_{i\alpha} \frac{\partial}{\partial x_\alpha^{(1)}} \right) \left(1 - \frac{\Delta t}{2\sigma} \right) \zeta_i^{(1)}$$

$$+ \sum_i \xi_{i\alpha} \left(\frac{\partial}{\partial t_1} + \xi_{i\alpha} \frac{\partial}{\partial x_\alpha^{(1)}} \right) \frac{\Delta t}{2} \varphi R_i^{(1)} = -\frac{1}{\sigma} \sum_i \xi_{i\alpha} \zeta_i^{(2)}. \tag{5.15}$$

In order to proceed, the expressions of moments of four particular parameters have to be configured, namely moments of the equilibrium density population f_i^{eq}, moments of first-order expanded term of the fluid population $\zeta_i^{(1)}$, moments of the second-order expanded term of the fluid population $\zeta_i^{(2)}$, and moments of the discrete forcing term R_i.

The moments of the former parameter was configured as

$$\sum_i f_i^{eq} = \sum_i \zeta_i + m\Delta t \sum_i R_i = \rho$$

$$\sum_i \xi_{i\alpha} f_i^{eq} = \sum_i \xi_{i\alpha} \zeta_i + m\Delta t \sum_i \xi_{i\alpha} R_i = \rho u_\alpha$$

$$\sum_i \xi_{i\alpha} \xi_{i\beta} f_i^{eq} = \sum_i \xi_{i\alpha} \xi_{i\beta} \zeta_i + m\Delta t \sum_i \xi_{i\alpha} \xi_{i\beta} R_i = \rho u_\alpha u_\beta + \rho c_s^2 \delta_{\alpha\beta} \tag{5.16}$$

$$\sum_i \xi_{i\alpha} \xi_{i\beta} \xi_{i\gamma} f_i^{eq} = \sum_i \xi_{i\alpha} \xi_{i\beta} \xi_{i\gamma} \zeta_i + m\Delta t \sum_i \xi_{i\alpha} \xi_{i\beta} \xi_{i\gamma} R_i = \rho c_s^2 \left(u_\alpha \delta_{\beta\gamma} + u_\beta \delta_{\alpha\gamma} + u_\gamma \delta_{\alpha\beta} \right)$$

Here, δ_{ij} represents the Kronecker delta. Quantity m was defined as

$$m = \begin{cases} 0, & \text{for scenario IA, IB and IC} \\ \dfrac{1}{2}, & \text{for scenario IIA, IIB and IIC.} \end{cases} \tag{5.17}$$

Subsequently, moments of $\zeta_i^{(1)}$ and $\zeta_i^{(2)}$ were respectively configured as

$$\sum_i \zeta_i^{(1)} = -m\Delta t \sum_i R_i^{(1)}$$

$$\sum_i \xi_{i\alpha} \zeta_i^{(1)} = -m\Delta t \sum_i \xi_{i\alpha} R_i^{(1)}$$

$$\sum_i \xi_{i\alpha} \xi_{i\beta} \zeta_i^{(1)} = -m\Delta t \sum_i \xi_{i\alpha} \xi_{i\beta} R_i^{(1)} \tag{5.18}$$

$$\sum_i \xi_{i\alpha} \xi_{i\beta} \xi_{i\gamma} \zeta_i^{(1)} = -m\Delta t \sum_i \xi_{i\alpha} \xi_{i\beta} \xi_{i\gamma} R_i^{(1)}$$

$$\sum_i \zeta_i^{(2)} = 0$$

$$\sum_i \xi_{i\alpha} \zeta_i^{(2)} = 0$$

$$\sum_i \xi_{i\alpha} \xi_{i\beta} \zeta_i^{(2)} = 0 \tag{5.19}$$

$$\sum_i \xi_{i\alpha} \xi_{i\beta} \xi_{i\gamma} \zeta_i^{(2)} = 0.$$

Lastly, Table 3.2 outlines the moments of the forcing term R_i.

Table 3.2. Mathematical expressions for the moments of the discrete forcing
terms R_i by three considered forcing schemes.

Forcing Model	Zeroth-Order Moment $\left(\sum_i R_i\right)$	First-Order Moment $\left(\sum_i \xi_{i\alpha} R_i\right)$	Second-Order Moment $\left(\sum_i \xi_{i\alpha} \xi_{i\beta} R_i\right)$
Luo	0	F_α	0
Guo, et al.	0	F_α	$F_\alpha u_\beta + u_\alpha F_\beta$
Kupershtokh, et al.	0	F_α	$F_\alpha u_\beta + u_\alpha F_\beta + \dfrac{1}{\rho}\left(F_\alpha F_\beta\right)$

Substituting equations (5.16), (5.18) and (5.19) into equations (5.14) and (5.15), the following remarks are obtained:

$$\frac{\partial \rho}{\partial t_1} + \frac{\partial}{\partial x_\alpha^{(1)}}\left(\rho u_\alpha\right) = 0 \tag{5.20}$$

$$\frac{\partial}{\partial t_1}\left(\rho u_\alpha\right) + \frac{\partial}{\partial x_\beta^{(1)}}\left(\rho u_\alpha u_\beta + \rho c_s^2 \delta_{\alpha\beta}\right) = \left(\varphi + \frac{m\Delta t}{\sigma}\right)\sum_i \xi_{i\alpha} R_i^{(1)} \tag{5.21}$$

$$\frac{\partial}{\partial t_1}\left(\rho u_\alpha u_\beta + \rho c_s^2 \delta_{\alpha\beta}\right) = -\frac{\partial}{\partial x_\gamma^{(1)}}\left(\rho c_s^2 u_\alpha \delta_{\beta\gamma} + \rho c_s^2 u_\beta \delta_{\alpha\gamma} + \rho c_s^2 u_\gamma \delta_{\alpha\beta}\right)$$
$$+ \left(\varphi + \frac{m\Delta t}{\sigma}\right)\sum_i \xi_{i\alpha} \xi_{i\beta} R_i^{(1)} \tag{5.22}$$

$$\frac{\partial \rho}{\partial t_2} + \frac{\partial}{\partial x_\alpha^{(2)}}(\rho u_\alpha) = \frac{\partial}{\partial t_1}\sum_i R_i^{(1)}\left(m\Delta t - \frac{m(\Delta t)^2}{2\sigma} - \frac{\Delta t}{2}\varphi\right)$$
$$+ \frac{\partial}{\partial x_\alpha^{(1)}}\sum_i \xi_{i\alpha}R_i^{(1)}\left(m\Delta t - \frac{m(\Delta t)^2}{2\sigma} - \frac{\Delta t}{2}\varphi\right) \tag{5.23}$$

$$\frac{\partial}{\partial t_2}(\rho u_\alpha) + \frac{\partial}{\partial x_\beta^{(2)}}\left(\rho u_\alpha u_\beta + \rho c_s^2 \delta_{\alpha\beta}\right) = \frac{\partial}{\partial t_1}\sum_i \xi_{i\alpha}R_i^{(1)}\left(m\Delta t - \frac{m(\Delta t)^2}{2\sigma} - \frac{\Delta t}{2}\varphi\right)$$
$$+ \frac{\partial}{\partial x_\beta^{(1)}}\sum_i \xi_{i\alpha}\xi_{i\beta}R_i^{(1)}\left(m\Delta t - \frac{m(\Delta t)^2}{2\sigma} - \frac{\Delta t}{2}\varphi\right), \tag{5.24}$$

Combining equations (5.20) - (5.24), the following descriptions are prevailed:

$$\frac{\partial \rho}{\partial t} + \frac{\partial}{\partial x_\alpha}(\rho u_\alpha) + \frac{\partial}{\partial t}(\rho u_\alpha) + \frac{\partial}{\partial x_\beta}\left(\rho u_\alpha u_\beta + \rho c_s^2 \delta_{\alpha\beta}\right) =$$
$$\left(\varphi + \frac{m}{\Delta t}\right)\sum_i \xi_{i\alpha}R_i + \frac{\partial}{\partial t}\sum_i R_i\left(m\Delta t - \frac{m(\Delta t)^2}{2\sigma} - \frac{\Delta t}{2}\varphi\right)$$
$$+ \left(\frac{\partial}{\partial t}\sum_i \xi_{i\alpha}R_i + \frac{\partial}{\partial x_\alpha}\sum_i \xi_{i\alpha}R_i\right)\left(m\Delta t - \frac{m(\Delta t)^2}{2\sigma} - \frac{\Delta t}{2}\varphi\right)$$
$$- \frac{\Delta t}{2}\varphi\frac{\partial}{\partial x_\beta}\sum_i \xi_{i\alpha}\xi_{i\beta}R_i + \left(1 - \frac{\Delta t}{2\sigma}\right)\frac{\partial}{\partial x_\beta}\left(m\Delta t\sum_i \xi_{i\alpha}\xi_{i\beta}R_i\right). \tag{5.25}$$

$$\frac{\partial}{\partial t}\left(\rho u_\alpha u_\beta + \rho c_s^2 \delta_{\alpha\beta}\right) + \frac{\partial}{\partial x_\gamma}\left(\rho c_s^2 u_\alpha \delta_{\beta\gamma} + \rho c_s^2 u_\beta \delta_{\alpha\gamma} + \rho c_s^2 u_\gamma \delta_{\alpha\beta}\right) = \left(\varphi + \frac{m\Delta t}{\sigma}\right)\sum_i \xi_{i\alpha}\xi_{i\beta}R_i. \tag{5.26}$$

Equation (5.26) can be rearranged as

$$\frac{m\Delta t}{\sigma}\sum_i \xi_{i\alpha}\xi_{i\beta}R_i = \frac{\partial}{\partial t}\left(\rho u_\alpha u_\beta + \rho c_s^2 \delta_{\alpha\beta}\right) + \frac{\partial}{\partial x_\gamma}\left(\rho c_s^2 u_\alpha \delta_{\beta\gamma} + \rho c_s^2 u_\beta \delta_{\alpha\gamma} + \rho c_s^2 u_\gamma \delta_{\alpha\beta}\right)$$
$$- \varphi\sum_i \xi_{i\alpha}\xi_{i\beta}R_i. \tag{5.27}$$

Expanding the terms inside the brackets of equation (5.27), as well as executing proper mathematical rearrangement, the following remark was obtained:

$$m\Delta t \sum_i \xi_{i\alpha}\xi_{i\beta}R_i = -\sigma\frac{\partial}{\partial x_\gamma}\left(\rho u_\alpha u_\beta u_\gamma\right) + \sigma\rho c_s^2\left(\frac{\partial u_\alpha}{\partial x_\beta} + \frac{\partial u_\beta}{\partial x_\alpha}\right)$$
$$+ \sigma\left(\varphi + \frac{m\Delta t}{\sigma}\right)\left(u_\alpha\sum_i \xi_{i\beta}R_i + u_\beta\sum_i \xi_{i\alpha}R_i\right) \tag{5.28}$$
$$- \sigma\varphi\sum_i \xi_{i\alpha}\xi_{i\beta}R_i.$$

Substituting equation (5.28) into (5.25), as well as replacing the expressions for the zeroth- and first-order forcing moment terms from Table 3.2, the following remarks are captured:

$$\frac{\partial\rho}{\partial t} + \frac{\partial}{\partial x_\alpha}\left(\rho u_\alpha\right) = \frac{\partial}{\partial x_\alpha}\left(F_\alpha\left(m\Delta t - \frac{m(\Delta t)^2}{2\sigma} - \frac{\Delta t}{2}\varphi\right)\right) \tag{5.29}$$

$$\frac{\partial}{\partial t}\left(\rho u_\alpha\right) + \frac{\partial}{\partial x_\beta}\left(\rho u_\alpha u_\beta\right) = -\frac{\partial}{\partial x_\beta}\left(\rho c_s^2\delta_{\alpha\beta}\right) + \rho c_s^2\left(\sigma - \frac{\Delta t}{2}\right)\frac{\partial}{\partial x_\beta}\left(\frac{\partial u_\alpha}{\partial x_\beta} + \frac{\partial u_\beta}{\partial x_\alpha}\right)$$
$$+ \left(\varphi + \frac{m\Delta t}{\sigma}\right)F_\alpha + \frac{\partial}{\partial t}\left(F_\alpha\left(m\Delta t - \frac{m(\Delta t)^2}{2\sigma} - \frac{\Delta t}{2}\varphi\right)\right)$$
$$+ \left(\sigma - \frac{\Delta t}{2}\right)\left(\varphi + \frac{m\Delta t}{\sigma}\right)\frac{\partial}{\partial x_\beta}\left(u_\alpha F_\beta + F_\alpha u_\beta\right) \tag{5.30}$$
$$- \left(\sigma - \frac{\Delta t}{2}\right)\frac{\partial}{\partial x_\beta}\frac{\partial}{\partial x_\gamma}\left(\rho u_\alpha u_\beta u_\gamma\right) - \sigma\varphi\frac{\partial}{\partial x_\beta}\sum_i \xi_{i\alpha}\xi_{i\beta}R_i.$$

Substituting the expressions of σ, φ and m from equations (5.11), (5.12) and (5.17) into equations (5.29) and (5.30), the continuity and Navier-Stokes equations for the standard first-order accurate LBM scenario are recovered respectively as

$$\frac{\partial\rho}{\partial t} + \frac{\partial}{\partial x_\alpha}\left(\rho u_\alpha\right) = -\frac{\Delta t}{2}\frac{\partial F_\alpha}{\partial x_\alpha} \tag{5.31}$$

$$\frac{\partial}{\partial t}\left(\rho u_\alpha\right) + \frac{\partial}{\partial x_\beta}\left(\rho u_\alpha u_\beta\right) = -\frac{\partial p}{\partial x_\beta} + v\frac{\partial}{\partial x_\beta}\left(\frac{\partial u_\alpha}{\partial x_\beta} + \frac{\partial u_\beta}{\partial x_\alpha}\right) + F_\alpha$$
$$- \left(\tau_f - \frac{\Delta t}{2}\right)\frac{\partial}{\partial x_\beta}\frac{\partial}{\partial x_\gamma}\left(\rho u_\alpha u_\beta u_\gamma\right) - \frac{\Delta t}{2}\frac{\partial F_\alpha}{\partial t} \tag{5.32}$$
$$- \left(\tau_f - \frac{\Delta t}{2}\right)\frac{\partial}{\partial x_\beta}\left(u_\alpha F_\beta + F_\alpha u_\beta\right) - \tau_f\frac{\partial}{\partial x_\beta}\sum_i \xi_{i\alpha}\xi_{i\beta}R_i.$$

Meanwhile, the recovered hydrodynamics expressions for the second-order accurate LBM scenario occupy the following forms, respectively:

$$\frac{\partial \rho}{\partial t} + \frac{\partial}{\partial x_\alpha}\left(\rho u_\alpha\right) = 0 \tag{5.33}$$

$$\begin{aligned}
\frac{\partial}{\partial t}\left(\rho u_\alpha\right) + \frac{\partial}{\partial x_\beta}\left(\rho u_\alpha u_\beta\right) &= -\frac{\partial p}{\partial x_\beta} + \upsilon \frac{\partial}{\partial x_\beta}\left(\frac{\partial u_\alpha}{\partial x_\beta} + \frac{\partial u_\beta}{\partial x_\alpha}\right) + F_\alpha \\
&\quad -\left(\tilde{\tau}_f - \frac{\Delta t}{2}\right)\frac{\partial}{\partial x_\beta}\frac{\partial}{\partial x_\gamma}\left(\rho u_\alpha u_\beta u_\gamma\right) \\
&\quad -\left(\tilde{\tau}_f - \frac{\Delta t}{2}\right)\frac{\partial}{\partial x_\beta}\left(u_\alpha F_\beta + F_\alpha u_\beta\right) - \left(\tilde{\tau}_f - \frac{\Delta t}{2}\right)\frac{\partial}{\partial x_\beta}\sum_i \xi_{i\alpha}\xi_{i\beta}R_i.
\end{aligned} \tag{5.34}$$

Here, the pressure p and fluid kinematic viscosity υ accordingly occupy the following descriptions:

$$p = \rho c_s^2 \delta_{\alpha\beta} \tag{5.35}$$

$$\upsilon = \begin{cases} \rho c_s^2\left(\tau_f - \dfrac{\Delta t}{2}\right), & \text{for scenario IA, IB and IC} \\[2mm] \rho c_s^2\left(\tilde{\tau}_f - \dfrac{\Delta t}{2}\right), & \text{for scenario IIA, IIB and IIC.} \end{cases} \tag{5.36}$$

In comparison with the exact continuity and Navier-Stokes formulas depicted by equations (2.59) and (2.60), the recovered macroscopic expressions of equations (5.31) - (5.34) contain residual fractions. By incorporating the second-order moment of the discrete forcing term R_i from Table 3.2, the mathematical expressions for residual fractions in the recovered hydrodynamics equations from each considered LBM scenario can be obtained. Table 3.3 summarizes such annotations.

Table 3.3. The residual fractions in the recovered continuity and Navier-Stokes equations from every considered LBM scenario.

LBM scenario	Residual Fractions in the Restored Continuity Equation	Residual Fractions in the Restored Navier-Stokes Equation
IA	$-\dfrac{\Delta t}{2}\dfrac{\partial F_\alpha}{\partial x_\alpha}$	$-\dfrac{\Delta t}{2}\dfrac{\partial F_\alpha}{\partial t} + \left(\tau_\upsilon - \dfrac{\Delta t}{2}\right)\dfrac{\partial}{\partial x_\beta}\left(u_\alpha F_\beta + F_\alpha u_\beta\right)$
IB	$-\dfrac{\Delta t}{2}\dfrac{\partial F_\alpha}{\partial x_\alpha}$	$-\dfrac{\Delta t}{2}\dfrac{\partial F_\alpha}{\partial t} - \dfrac{\Delta t}{2}\dfrac{\partial}{\partial x_\beta}\left(u_\alpha F_\beta + F_\alpha u_\beta\right)$
IC	$-\dfrac{\Delta t}{2}\dfrac{\partial F_\alpha}{\partial x_\alpha}$	$-\dfrac{\Delta t}{2}\dfrac{\partial F_\alpha}{\partial t} - \dfrac{\Delta t}{2}\dfrac{\partial}{\partial x_\beta}\left(u_\alpha F_\beta + F_\alpha u_\beta\right) - \tau_\upsilon\dfrac{\partial}{\partial x_\beta}\left(\dfrac{F_\alpha F_\beta}{\rho}\right)$

IIA	0	$\left(\overline{\tau}_{v} - \dfrac{\Delta t}{2} \right) \dfrac{\partial}{\partial x_{\beta}} \left(u_{\alpha} F_{\beta} + F_{\alpha} u_{\beta} \right)$
IIB	0	0
IIC	0	$-\left(\overline{\tau}_{v} - \dfrac{\Delta t}{2} \right) \dfrac{\partial}{\partial x_{\beta}} \left(\dfrac{F_{\alpha} F_{\beta}}{\rho} \right)$

3.2.2 Chapman-Enskog Analysis for Thermal Population

The Chapman-Enskog analysis for the thermal population was administered by undertaking similar exposition as in the fluid population case described earlier. The only difference is that the representative Boltzmann equations for the thermal population, namely equations (5.2) and (5.4), were used in the evaluation. Adopting similar procedures as in the former fluid population case, the recovered macroscopic heat equation takes the following remark:

$$\frac{\partial T}{\partial t} + \frac{\partial}{\partial x_{\alpha}} (T u_{\alpha}) = \frac{\partial}{\partial x_{\alpha}} \left(D \frac{\partial T}{\partial x_{\alpha}} \right) + \frac{D}{c_s^2} \frac{\partial}{\partial x_{\alpha}} \left(T \left(\frac{\partial u_{\alpha}}{\partial t} + \frac{\partial}{\partial x_{\beta}} \left(u_{\alpha} u_{\beta} \right) \right) \right). \tag{5.37}$$

Here, the thermal diffusivity occupies the following definitions for the first- and second-order LBM scenarios, respectively:

$$D = \begin{cases} c_s^2 \left(\tau_g - \dfrac{\Delta t}{2} \right), & \text{for scenario IA, IB and IC} \\[2mm] c_s^2 \left(\tilde{\tau}_g - \dfrac{\Delta t}{2} \right), & \text{for scenario IIA, IIB and IIC.} \end{cases} \tag{5.38}$$

A careful inspection upon equation (5.37) indicates that that the first- and second-order accurate thermal LBM scenarios essentially returned equivalent macroscopic heat equation. Such situation exist presumably due to the absence of the discrete forcing term R_i in the representative Boltzmann equations of the thermal population. Here, in comparison with the exact formulation of heat equation (2.61), the restored macroscopic heat equation contains one residual fraction, appropriately depicted by the last term on the right hand side of equation (5.37). Nevertheless, it is noteworthy to mention that the former residual terms in the restored momentum equation are also presented within the thermal residual fraction.

3.3 Numerical Simulation of Unsteady Thermal Convection Flow and Heat Transfer

The theoretical aspects of Chapman-Enskog analysis in the earlier sections of this section extend the analysis to examine the plausible discrepancy in computational behavior amongst the considered LBM scenarios. Two distinguished convection and heat transfer phenomena (the natural convection in a differentially-heated cavity and the Rayleigh-Bènard convection) were appointed as the physical platforms to test the computational characteristics of disparate LBM scenarios.

The numerical simulations of both physical phenomena were performed in a two-dimensional closed cavity under the condition of $Ra = 10^4$ and $Pr = 0.71$. The computational workloads were administered upon the graphical processing unit (GPU) ecosystem so as to expedite the analyses. In such physical arrangements, the Mach number (Ma) is defined as

$$Ma = \frac{u_{\text{char}}}{c_s} = \sqrt{\frac{Ra\upsilon^2}{PrH^2c_s^2}},$$
(5.39)

where u_{char} designates the characteristic velocity of the flowing material. The particular property is defined as

$$u_{\text{char}} = \sqrt{G_y\beta_T\left(\Theta_{\text{hot}} - \Theta_{\text{cold}}\right)H} = \sqrt{\frac{Ra\upsilon^2}{PrH^2}},$$
(5.40)

where Θ_{hot} and Θ_{cold} specify, respectively, the dimensionless hot and cold temperatures. The dimensionless temperature can be expressed as

$$\Theta = \frac{T - T_{\text{ref}}}{T_{\text{hot}} - T_{\text{cold}}},$$
(5.41)

where T_{ref} denotes the reference temperature that is usually set as Θ_{cold}.

3.3.1 Numerical Simulation of Natural Convection in a Differentially-Heated Cavity

Figure 3.1 schematizes the physical configuration of natural convection in a differentially-heated cavity. The entire domain is assumed to be filled with a stationary fluid.
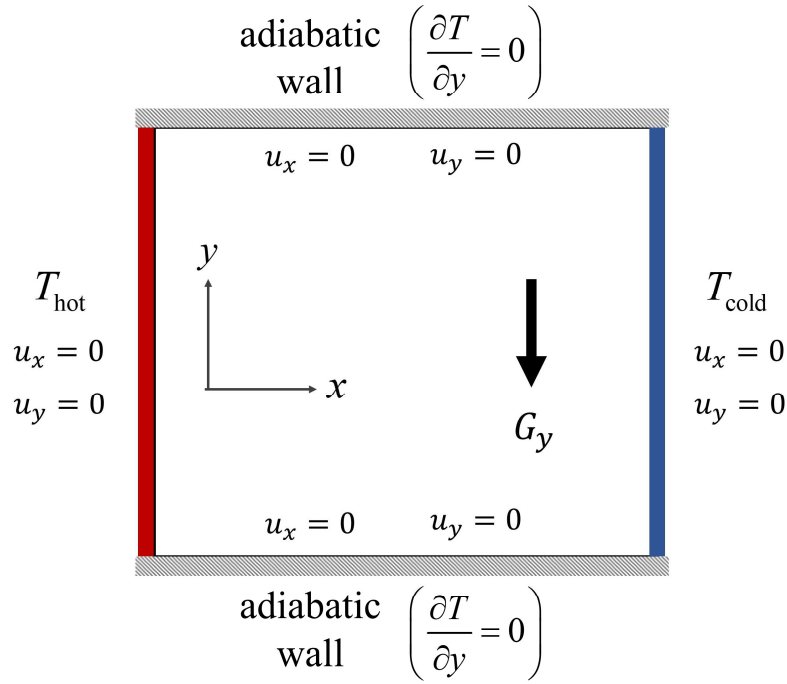
Figure 3.1. Domain configuration for two-dimensional natural convection in a differentially-heated cavity.

The vertical walls of the cavity were characterized by contrasting thermal conditions. The left-border keeps a constant hot temperature (T_{hot}) while the opposite wall is assumed to be a constant cold temperature (T_{cold}). On the other hand, the horizontal boundaries are assumed to be heat insulated. For the fluid substance, the non-equilibrium bounce-back (NEBB) method, exemplified by equation (2.72), was adopted upon all the corresponding perimeters including the four corners. Meanwhile, for the thermal population, the anti-bounce-back (ABB) method, expressed by equation (2.73), and the central finite difference technique were administered upon the vertical and horizontal boundaries.

To accomplish a valid comparison, numerical simulations for all the considered LBM scenarios were accomplished for hydrodynamic relaxation time $(\tau_v = 0.6)$ and Mach number $(Ma = 0.1)$ conditions. The average Nusselt number $\langle Nu \rangle$ was calculated as the dimensionless property that represents the heat transfer performance of each concomitant LBM scenario. This property is abided to the following definition:

$$\langle Nu \rangle = 1 + \left(\frac{\langle u_x^* \Theta \rangle}{\Theta_{hot} - \Theta_{cold}} \right), \tag{5.42}$$

where $\langle u_x^* \Theta \rangle$ represents the average of the product between the dimensionless horizontal velocity and the dimensionless temperature along the cold or hot wall. For the sake of validation, the associated steady-state flow profile by the IIB-LBM scenario was selected to examine the final streamlines and isotherms in the corresponding heat and mass transport system.

Table 3.4 outlines the principal steady-state numerical properties from distinct LBM scenarios. The parameters were compared with the outcomes of finite difference method (FDM) (De Vahl Davis, 1983) and finite element method (FEM) (Syrjälä, 1996). Assuming the solutions of FDM and FEM show more accurate ones, it reveals that LBM scenarios adopt a second-order accurate model (i.e., scenario IIA, IIB, and IIC) are capable in delivering better compliance with the benchmark solutions than the ones which comprise first-order scheme (i.e., scenario IA, IB, and IC).

Table 3.4. Steady-state solutions of two-dimensional natural convection in a differentially-heated cavity for $Ra = 10^4$, $Pr = 0.71$, $\tau_v = 0.6$, and $Ma = 0.1$ by LBM scenarios, finite difference method (FDM) (De Vahl Davis, 1983) and finite element method (FEM) (Syrjälä, 1996).

Simulation Parameters	LBM Scenarios (Present Study)						FDM	FEM
	IA	IB	IC	IIA	IIB	IIC		
$\langle Nu \rangle$	2.2341	2.2339	2.2339	2.2424	2.2423	2.2424	2.243	2.2448
Max $u_x^{*\dagger}$	16.0678	16.0619	16.0619	16.1742	16.1732	16.1742	16.178	16.1853
Max $u_y^{*\ddagger}$	19.3927	19.3864	19.3864	19.6011	19.5999	19.6011	19.617	19.6316
Location of Max $u_x^{*\dagger}$	0.8116	0.8116	0.8116	0.8204	0.8204	0.8204	0.823	0.8230
Location of Max $u_y^{*\ddagger}$	0.1159	0.1159	0.1159	0.1189	0.1189	0.1189	0.119	0.1188

†at $x^* = 0.5$; ‡at $y^* = 0.5$.

Figure 3.2 exhibits the steady-state streamlines and isotherms from the selected LBM scenario. The corresponding streamlines and isotherms profiles look a good matching with the literature, such as in Dixit and Babu (2006), Du and Liu (2013), Mayne *et al.* (2000), and Yu and Tian (2012). It is found, however, that the simulation results using the six associated LBM scenarios exhibit the almost same steady-state flow profiles. From a practical point of view, very LBM scenario shows the same numerical solutions for the steady-state condition.

$$(a)$$
$$(b)$$
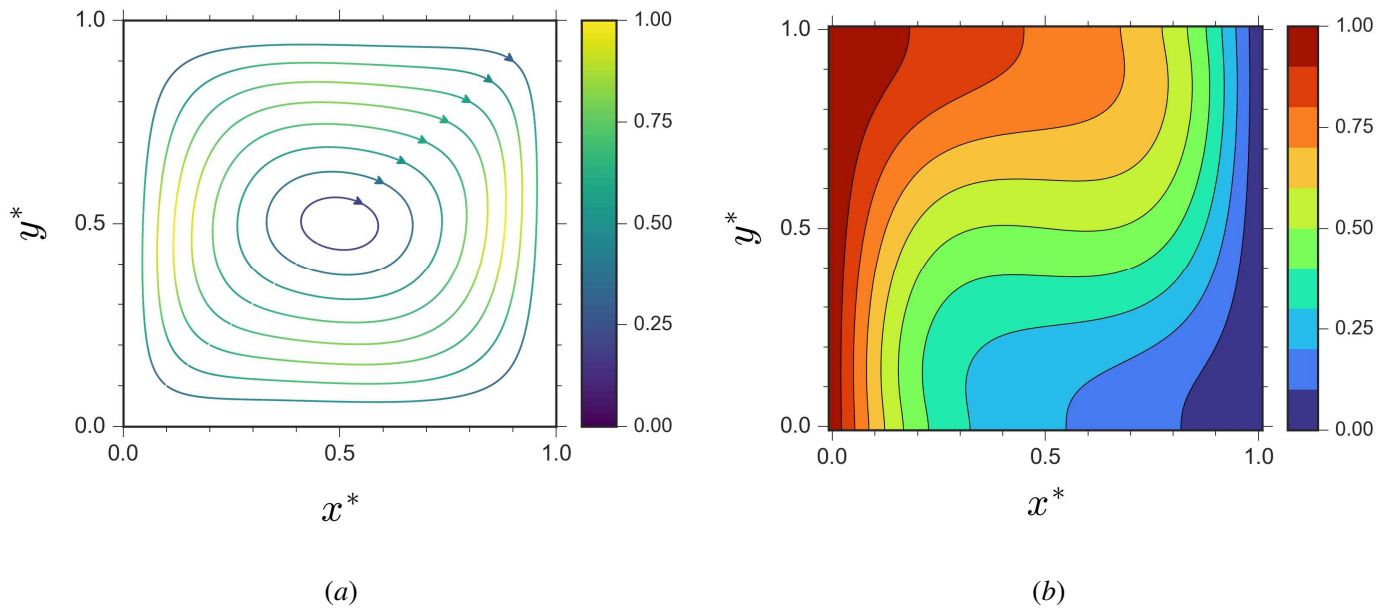
Figure 3.2. Steady-state flow characteristics of two-dimensional natural convection in a differentially-heated cavity for $Ra = 10^4$, $Pr = 0.71$, $\tau_v = 0.6$ and $Ma = 0.1$ by IIB-LBM scenario, displaying (a) Streamlines and (b) Isotherms contour.

Recording the behavior of specific parameters along the simulation process provides a way of uncovering additional key information regarding the computational capacity of the considered LBM scenarios. Figure 3.3 shows the profiles of $\langle Nu \rangle$ from different LBM scenarios with the dimensional simulation time t appointed as the horizontal axis. The figure clearly displays the existence of striking contrast in the computational characteristics among distinct LBM scenarios.
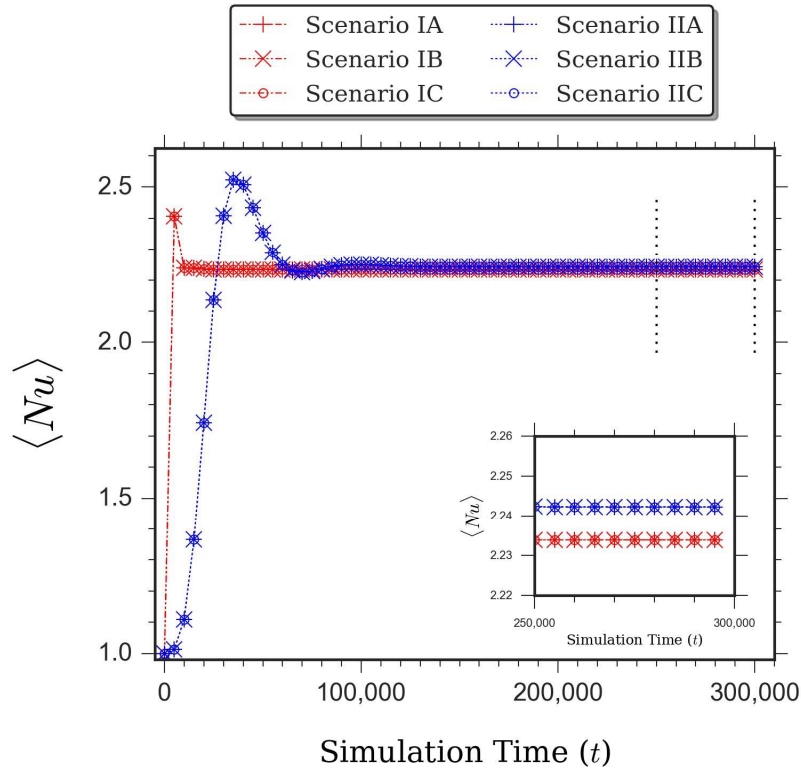
Figure 3.3. Profiles of average Nusselt number $\langle Nu \rangle$ from different LBM scenarios during the unsteady period up to the accomplishment of the steady-state condition of the natural convection a in differentially-heated cavity for $Ra = 10^4$, $Pr = 0.71$, $\tau_\nu = 0.6$, and $Ma = 0.1$. Figure inset displays the magnification of the computational characteristics in the steady-state condition of the simulation.

The discrepancy in computational characteristics amongst distinct LBM scenarios was predominantly apparent when the simulations prevail under unsteady-state condition. Altering the fashion from unsteady to steady state, the disparity either decreases gradually or was negligible (Figure 3.3). Such discrepancy was in agreement with the physical properties outlined in Table 3.4.

Figure 3.3 unveils essential information regarding the primary factor responsible for the observed discrepancy in computational performance of distinct LBM scenarios. It appears then that the order of accuracy of the LBM equation is the predominant factor that generates the observed disparity in computational characteristics. On the other hand, the contribution of distinct forcing strategies upon such disparity is found to be inconsequential. The profiles of dimensionless horizontal velocity u_x^* at the vertical mid-plane of the enclosure $\left(x^* = 0.5 \right)$ were displayed in Figure 3.4. Therein, the profiles of u_x^* demonstrate similar behavior with the ones observed in Figure 3.3.
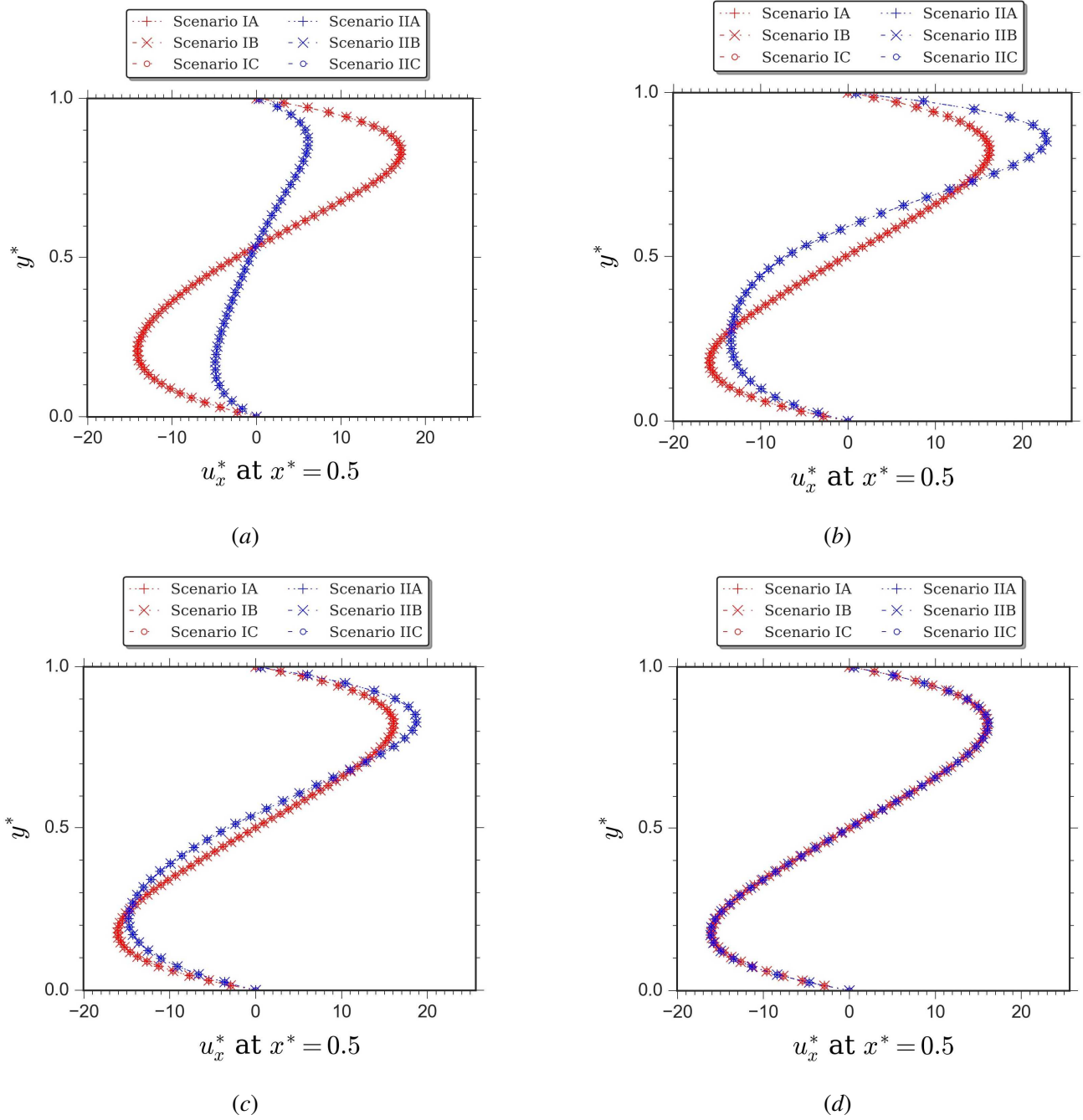
Figure 3.4. Profiles of dimensionless horizontal velocity at the vertical mid-plane of the cavity upon different simulation periods of natural convection in differentially-heated cavity for $Ra = 10^4$, $Pr = 0.71$, $\tau_v = 0.6$ and $Ma = 0.1$, demonstrating condition at time iteration: (*a*) 10,000; (*b*) 25,000; (*c*) 50,000 and (*d*) 300,000.

Figure 3.5 displays the corresponding computational overhead from every considered LBM scenario. The scenario IIC was identified as the particular LBM scenario with the highest computational demand in modeling fluid flow and heat transfer in a differentially-heated cavity, therein.
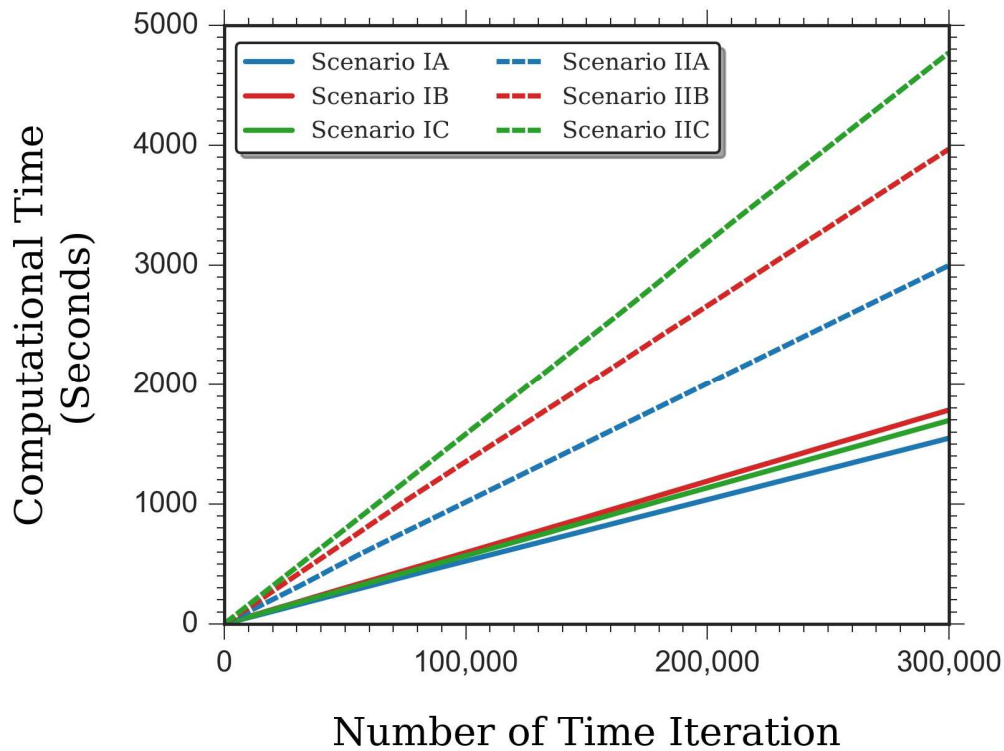
Figure 3.5. Computational overhead of disparate LBM scenarios in modelling natural convection in a differentially-heated cavity with $Ra = 10^4$, $Pr = 0.71$, $\tau_v = 0.6$ and $Ma = 0.1$, starting from the unsteady period up to the accomplishment of the steady-state period

3.3.2 Simulation of Rayleigh-Bènard Convection

After undertaking evaluation regarding computational characteristics of distinct LBM scenarios upon simulating natural convection in a differentially-heated enclosure in the previous section, the current segment of the article aims at elucidating the capacity of disparate LBM scenarios while simulating the Rayleigh-Bènard convection (RBC) phenomena as illustrated in Figure 3.6.

$$T_{\text{cold}}$$

$$u_x = 0 \qquad u_y = 0$$

adiabatic
wall

$$\left(\frac{\partial T}{\partial x} = 0 \right)$$

$$u_x = 0$$
$$u_y = 0$$

adiabatic
wall

$$\left(\frac{\partial T}{\partial x} = 0 \right)$$

$$u_x = 0$$
$$u_y = 0$$

y

x

G_y

$$u_x = 0 \qquad u_y = 0$$

$$T_{\text{hot}}$$
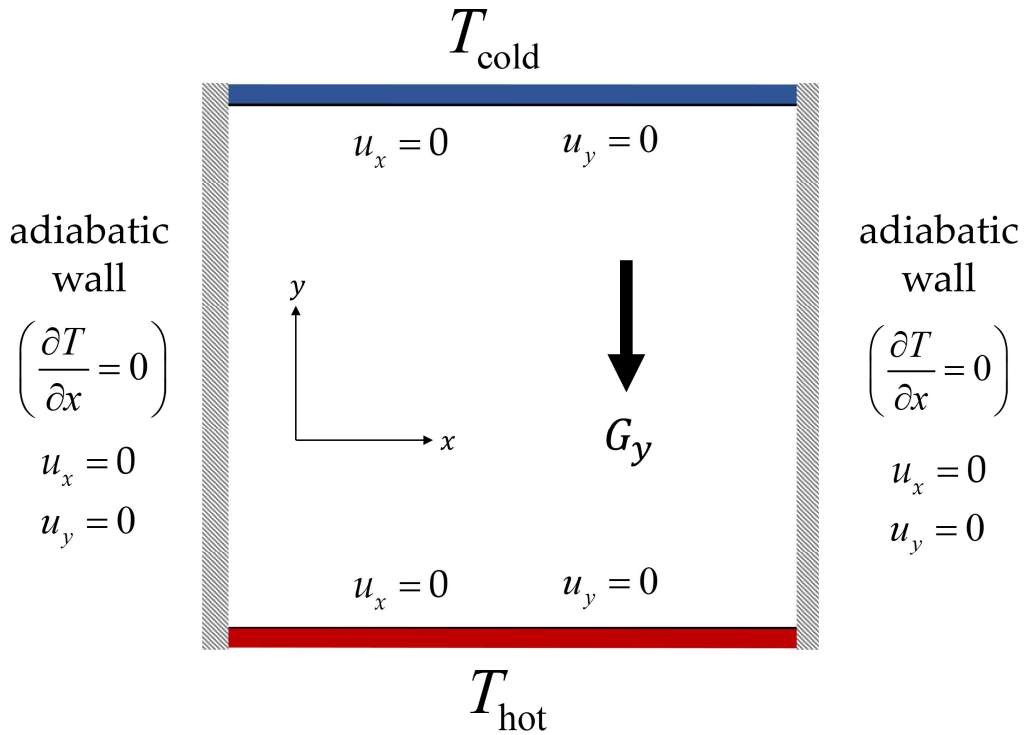
Figure 3.6. Domain configuration for two-dimensional Rayleigh-Bènard convection with aspect ratio one.

Hot temperature condition was imposed upon the horizontal bottom wall while the opposing top margin was set to occupy cold temperature. The vertical boundaries were set to be perfectly insulated. Boundary treatments were accomplished through adopting similar strategies with the erstwhile case of natural convection in a differentially-heated cavity. However, appropriate adjustments were necessary in order to account the appointed wall conditions in RBC configuration

The contrasting driving force from buoyancy and gravitational attraction in the RBC system results in perpetual competition between the tendency of the flowing materials to move upward and downward, correspondingly. Such a situation enables the associated thermo-hydrodynamics phenomena to exhibit a number of plausibly distinct flow behaviors with variable convection roll patterns (Goldhirsch *et al.*, 1989; Shan, 1997). To mitigate such complexity, the present study assimilates infinitesimal perturbation into the corresponding physical system. The perturbation was

administered to the initial density and temperature profiles. Such functions were respectively defined as

$$\rho_{\text{initial}}(x,y) = \rho_{\text{ref}}\left(1 + \beta_T \frac{(\Theta_{\text{hot}} - \Theta_{\text{cold}})y}{N_y}\left(1 - 0.001\sin\left(\frac{2\pi x}{N_x}\right)\right)\right) \qquad (5.43)$$

$$\Theta_{\text{initial}}(x,y) = \Theta_{\text{hot}} - \left(\frac{(\Theta_{\text{hot}} - \Theta_{\text{cold}})y}{N_y}\left(1 - 0.001\sin\left(\frac{2\pi x}{N_x}\right)\right)\right), \qquad (5.44)$$

where N_x and N_y designate the associated lattice nodes in the horizontal and vertical directions of the spatial coordinate, respectively.

The performance of heat transfer in RBC system was represented by the average Nusselt number at the hot wall, $\langle Nu \rangle_0$. The corresponding parameter was mathematically expressed as

$$\langle Nu \rangle_0 = \frac{1}{N_x(\Theta_{\text{hot}} - \Theta_{\text{cold}})}\sum_{i=1}^{N_x} q_y(i)\big|_{y=0}. \qquad (5.45)$$

Here, q_y specifies the local heat flux in vertical direction, defined as

$$q_y = u_y^*\Theta - \frac{\partial\Theta}{\partial y}. \qquad (5.46)$$

The last term on the right-hand side of the above formula denotes temperature gradient in a vertical direction.

Figure 3.7 presents the final streamlines and isotherms for RBC simulation with $Ra = 10^4$ and $Pr = 0.71$. Similar to the former case of natural convection in a differentially-heated cavity, the steady-state flow profile from scenario IIB was selected for exhibition and validation purposes. The corresponding streamlines and isotherms displayed in Figure 3.7 were in excellent agreement with the earlier work of Ouertatani *et al.* (2008).

Similarly to the former case of natural convection in a differentially-heated cavity, the obtained steady-state responses from distinct LBM scenarios demonstrate identical flow profiles. Nevertheless, minor discrepancy was observed in the captured $\langle Nu \rangle_0$ solutions, which are summarized and compared with the outcomes of finite volume method (FVM) (Ouertatani *et al.*, 2008) in Table 3.5.

(a) (b)
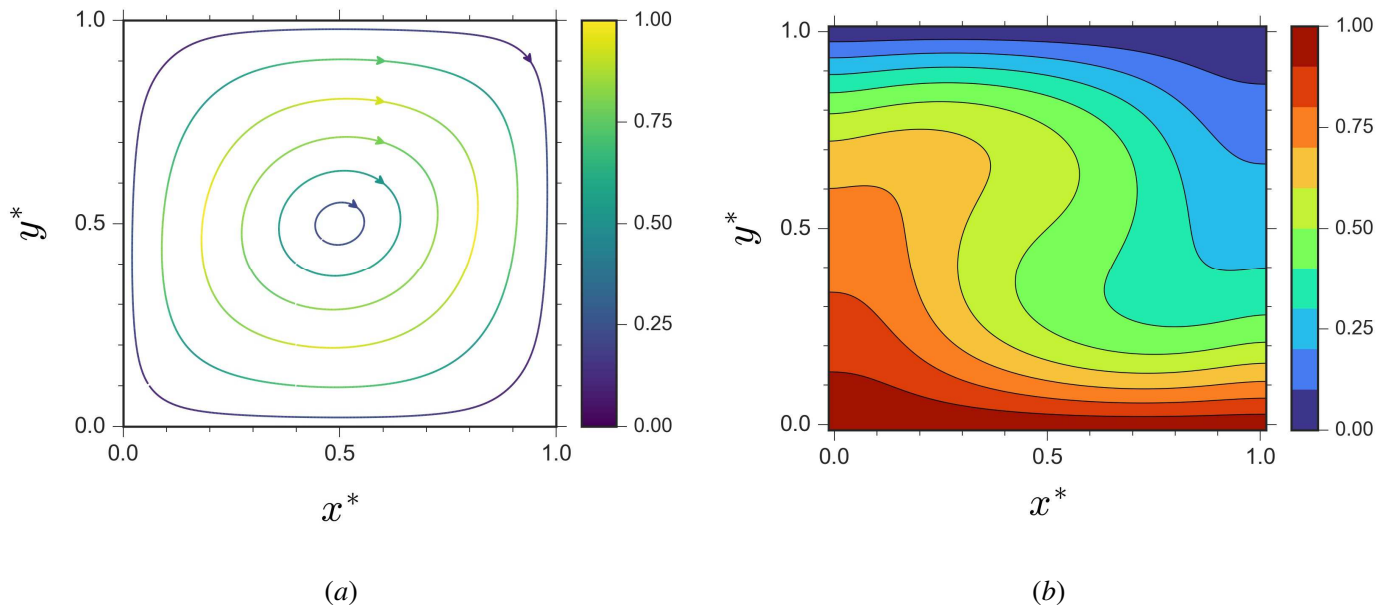
Figure 3.7. Steady-state flow characteristics of Rayleigh-Bènard convection with aspect ratio = 1, $Ra = 10^4$, $Pr = 0.71$, $\tau_v = 0.6$, and $Ma = 0.1$ from scenario IIB, displaying (a) Streamlines and (b) Isotherms contour.

Table 3.5. Average Nusselt number at the hot wall $\langle Nu \rangle_0$ of the Rayleigh-Bènard convection system from distinct LBM scenarios during the steady-state period of the flow for aspect ratio = 1, $Ra = 10^4$, $Pr = 0.71$, $\tau_v = 0.6$, and $Ma = 0.1$ compared with the outcome of the finite volume method (FVM) (Ouertatani *et al.*, 2008)

Simulation Parameter	LBM Scenario (Present Study)						FVM
	IA	IB	IC	IIA	IIB	IIC	
$\langle Nu \rangle_0$	2.1681	2.1684	2.1684	2.1554	2.1555	2.1554	2.1581

A better accuracy of $\langle Nu \rangle_0$ solutions was obtained from the LBM scenarios which adopt a second-order accurate LBM scenario. The profiles of $\langle Nu \rangle_0$ along the simulation process exhibited characteristics similar to those observed in the former natural convection case. Figure 3.8 illustrates further the behavior of $\langle Nu \rangle_0$. Figure 3.9 shows the profiles of dimensionless vertical velocity u_y^* at the horizontal mid-plane of the cavity $\left(y^* = 0.5 \right)$. Therein, similar computational behavior was observed as the one prevailing in Figure 3.8.
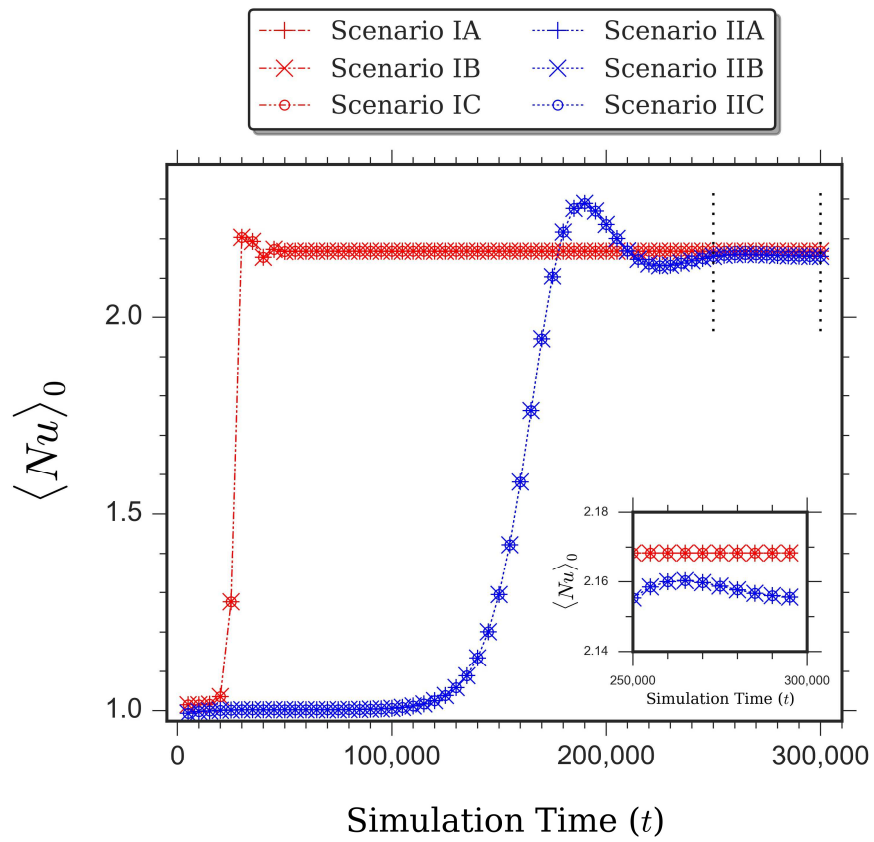
Figure 3.8. Profiles of average Nusselt number at the hot wall $\langle Nu \rangle_0$ from different LBM scenarios during the unsteady period up to the accomplishment of steady-state condition of the Rayleigh-Bènard convection for aspect ratio = 1, $Ra = 10^4$, $Pr = 0.71$, $\tau_\upsilon = 0.6$, and $Ma = 0.1$. Figure inset displays the magnification of the computational characteristics in the steady-state region of the simulation.
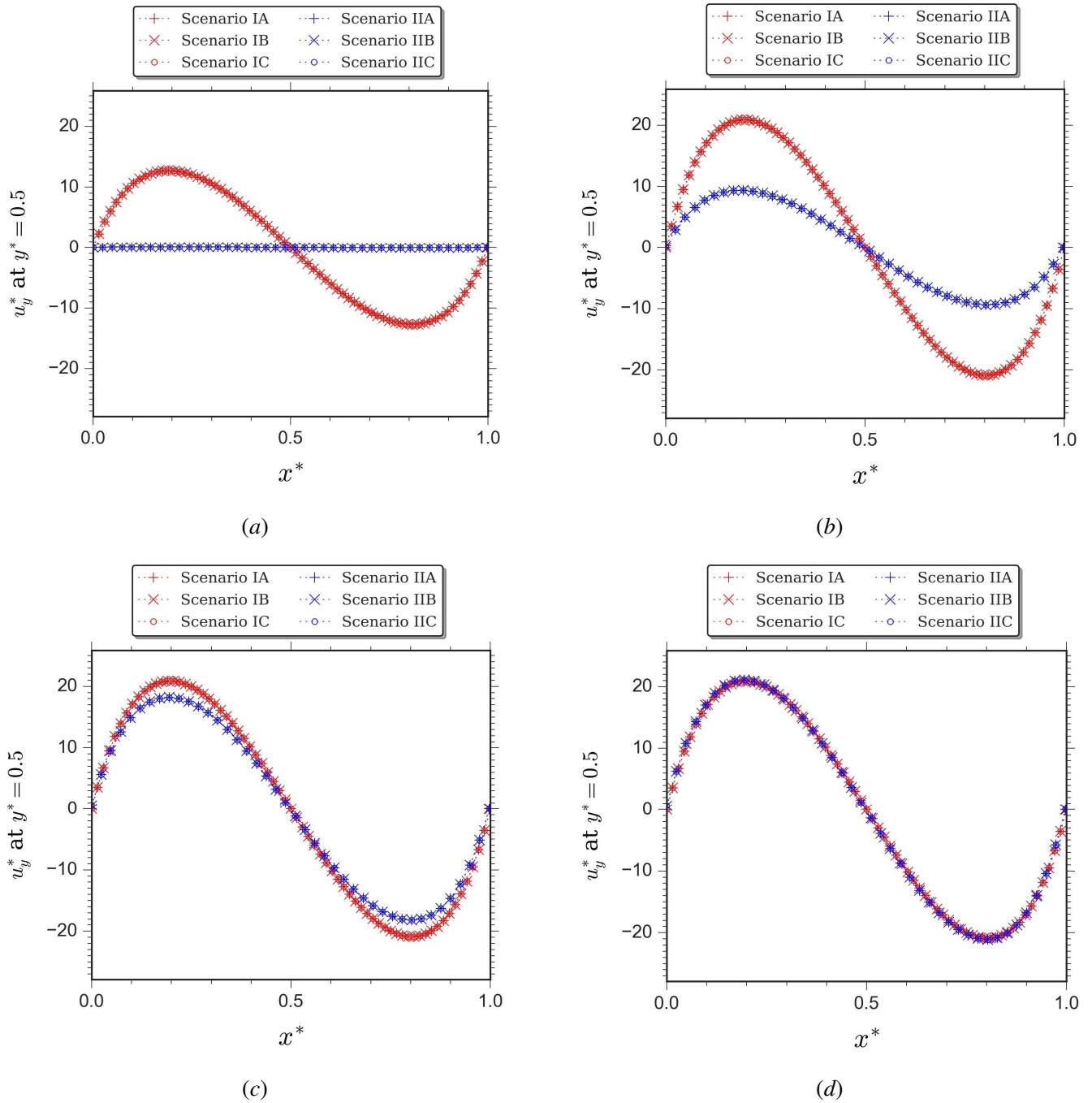
Figure 3.9. Profiles of dimensionless vertical velocity at the horizontal mid-plane of the cavity upon different simulation periods of Rayleigh-Bènard convection for aspect ratio = 1, $Ra = 10^4$, $Pr = 0.71$, $\tau_v = 0.6$, and $Ma = 0.1$, demonstrating conditions at the following time iterations: (**a**) 25,000; (**b**) 140,000; (**c**) 160,000; and (**d**) 300,000.

Figure 3.10 depicts the corresponding profiles of computational cost from every considered LBM scenarios. Similar with the case of natural convection in a differentially-heated cavity, higher computational demand was displayed by the LBM scenarios which adopt a second-order accurate LBM arrangement.
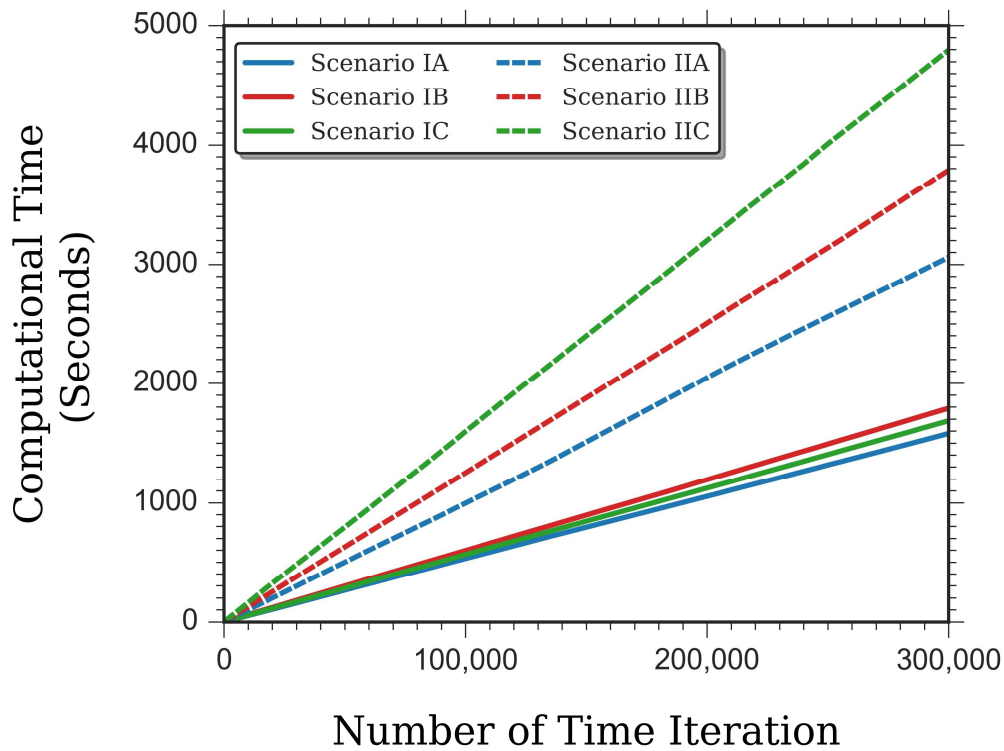
Figure 3.10. Computational overhead of disparate LBM scenarios in modelling Rayleigh-Bènard convection with aspect ratio = 1, $Ra = 10^4$, $Pr = 0.71$, $\tau_v = 0.6$ and $Ma = 0.1$, starting from the transient period up to the accomplishment of the quasi-steady-state period.

3.4   Summary

In this chapter, comprehensive evaluation regarding the efficacy of disparate Lattice Boltzmann Method (LBM) scenarios upon simulation of fluid flow and heat transfer phenomena were studied. The primary objective, herein addressed, was the evaluation of the plausible discrepancy in the computational characteristics of different LBM scenarios when simulating natural convection and heat transfer systems during the unsteady period of the flow. To fulfil the sought objective, the LBM

scenarios were tested upon two distinctive thermo-hydrodynamics systems, namely the natural convection in a differentially-heated cavity and the Rayleigh-Bènard convection.

The key findings of this chapter are:

1. The presence of considerable discrepancy in computational characteristics of disparate LBM scenarios was seen during the unsteady period of the simulation, which diminished gradually as the simulation advanced towards a steady-state condition.

2. The order of accuracy of the discrete lattice Boltzmann expression was identified as the predominant factor inherent to discrepancy in computational characteristics.

3. The contribution of distinct forcing models upon the heterogeneity in computational behavior was found to be trivial.

4. As a steady-state condition, the LBM scenarios which administer a second-order accurate LBM scenario recovered better numerical accuracy than those scenarios which comprise a first-order accurate model. However, the scheme is challenged by higher computational demand.

Chapter 4: Simulation of Unsteady Rayleigh-Bènard Convection under Time-Periodic Boundary Condition: The Effects of Amplitude and Frequency on the Flow Characteristics

4.1 Unsteady Rayleigh-Bènard Convection under Transient Temperature Condition

Fluid flow and heat transfer process pertinent to geothermal system typically exhibits unsteady behavior with time. The complexity of underground porous media as well as the associated flow phenomena occurred therein trigger the occurrence of transient heat flux from the geothermal source formation. As such, the convective flow and heat transfer phenomena associated with geothermal system can be regarded as a special mode of unsteady Rayleigh-Bènard convection flow with time-varying heat flux contribution from the hot underground rock formation.

The present chapter investigates the flow and heat transfer characteristics of unsteady Rayleigh-Bènard convection due to transient temperature condition at the bottom hot wall of the domain. A two-dimensional enclosure with length-to-width aspect ratio equal to two was appointed as the flow domain to model the problem at hand. Figure 4.1 illustrates the schematic arrangement of the prescribed domain. Here, the vertical boundaries were set to be perfectly insulated, while the horizontal perimeters at the top and bottom walls were set to occupy contrasting thermal conditions. The top wall was kept constant at cold temperature, while the opposing bottom wall was set to hot temperature which varies periodically with time following a sinusoidal function, described as

$$T_{hot}(t) = \overline{T}_{hot} + A\sin\left(\frac{2\pi t}{p_\lambda}\right). \tag{9.1}$$

Here, $\overline{T}_{hot}$ represents the average temperature of the hot wall and t designates the simulation time. Parameters A and p_λ respectively denote the amplitude and period of the oscillation.
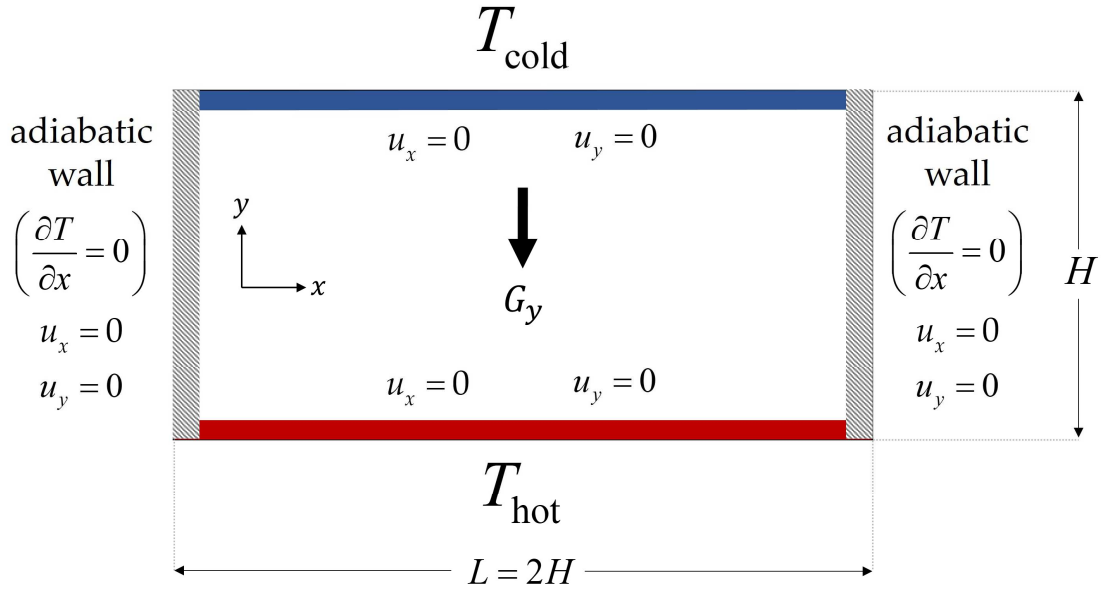
Figure 4.1. Domain configuration for the unsteady Rayleigh-Bènard convection system.
The length-to-width aspect ratio was equal to two.

For practical simulation purposes, the sinusoidal function of equation (9.1) was transformed into its concomitant dimensionless form. Such approach generates the following expression:

$$\Theta_{hot}\left(t^*\right) = \overline{\Theta}_{hot} + A^* \sin\left(\frac{2\pi t^*}{p_\lambda^*}\right), \tag{9.2}$$

where Θ specifies the non-dimensional temperature and t^* depicts the dimensionless simulation time. Quantities A^* and p_λ^* designate respectively the dimensionless amplitude and dimensionless period of the oscillation. The non-dimensional period can be obtained from the following relationship:

$$p_\lambda^* = p_\lambda \frac{D}{N_y^2}, \tag{9.3}$$

where D and N_y respectively denote the thermal diffusivity and the number of grid used in the vertical spatial coordinate. The dimensionless frequency of the oscillation $\left(f_\lambda^*\right)$ is defined as the reciprocal of the dimensionless period, namely

$$f_\lambda^* = \frac{1}{p_\lambda^*}. \tag{9.4}$$

Figure 4.2 shows the schematic illustration of the time-varying temperature at the hot wall.
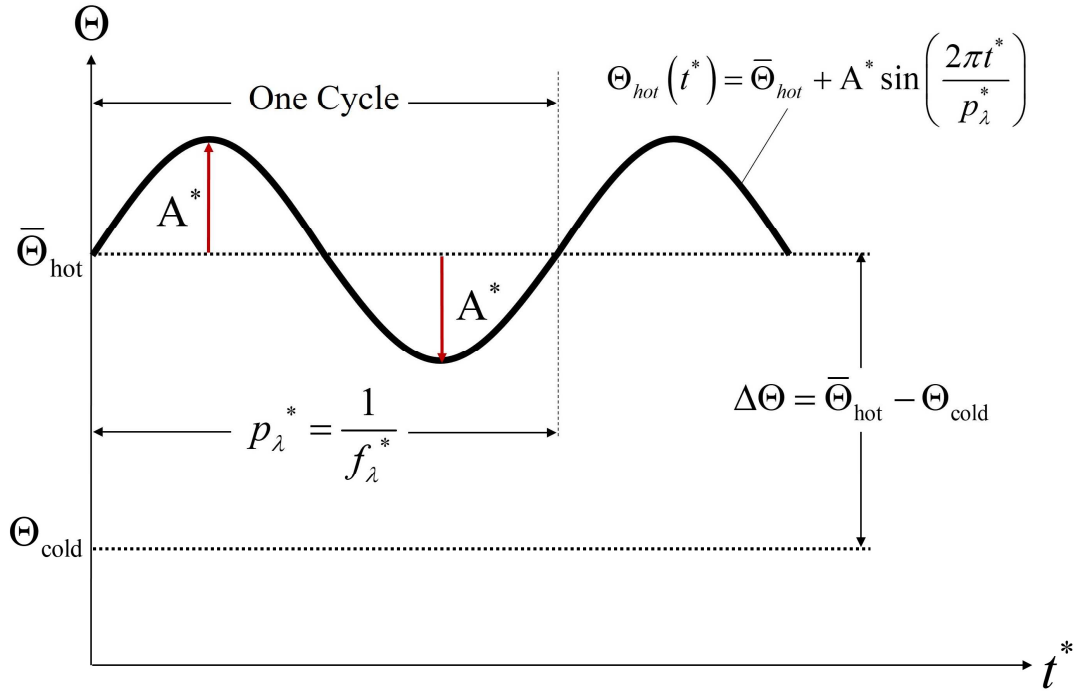
Figure 4.2. Time-dependent temperature at the hot wall.

Simulation was conducted using the second-order accurate single-relaxation-time (SRT) lattice Boltzmann method (LBM) for the fluid and thermal constituents, described accordingly by equations (2.20) and (2.32). A small perturbation was applied to the initial temperature distribution of the system according to the following relationship:

$$\Theta_i(x, y) = \overline{\Theta}_{hot} - \Delta\Theta \frac{y^*}{N_y}\left(0.9 - 0.005\sin\left(\frac{a\pi x^*}{N_x}\right)\right), \tag{9.5}$$

where x^* and y^* specify respectively the non-dimensional horizontal and vertical coordinates. Quantities a and N_x denote the perturbation coefficient and the assigned grid numbers in the horizontal direction, accordingly.

4.2 Numerical Validation of Rayleigh-Bènard Convection

Prior to simulating the unsteady Rayleigh-Bènard convection, the modified LBM scheme was validated with the available benchmark results. Physical configuration similar to the one depicted in Figure 4.1 was adopted. For the purpose of validation, the steady Rayleigh-Bènard convection under constant Prandtl number (*Pr*) of 0.71 (air) was simulated. The adiabatic condition at the vertical

boundaries was replaced by the periodic condition. Numerical simulation was performed under six different Rayleigh number conditions, namely $Ra = 5 \times 10^3, 1 \times 10^4, 2 \times 10^4, 3 \times 10^4, 5 \times 10^4$ and 1×10^5. For brevity, flow streamlines and isotherms at steady-state condition were shown only for $Ra = 5 \times 10^3$ and $Ra = 1 \times 10^5$. Both delineations were displayed in Figure 4.3 and Figure 4.4, respectively. The streamlines and isotherms profiles for the considered Rayleigh numbers were in excellent agreement with earlier studies of He *et al.* (1998), Inamuro *et al.* (2002) and Kao and Yang (2007).

(*a*)

(*b*)
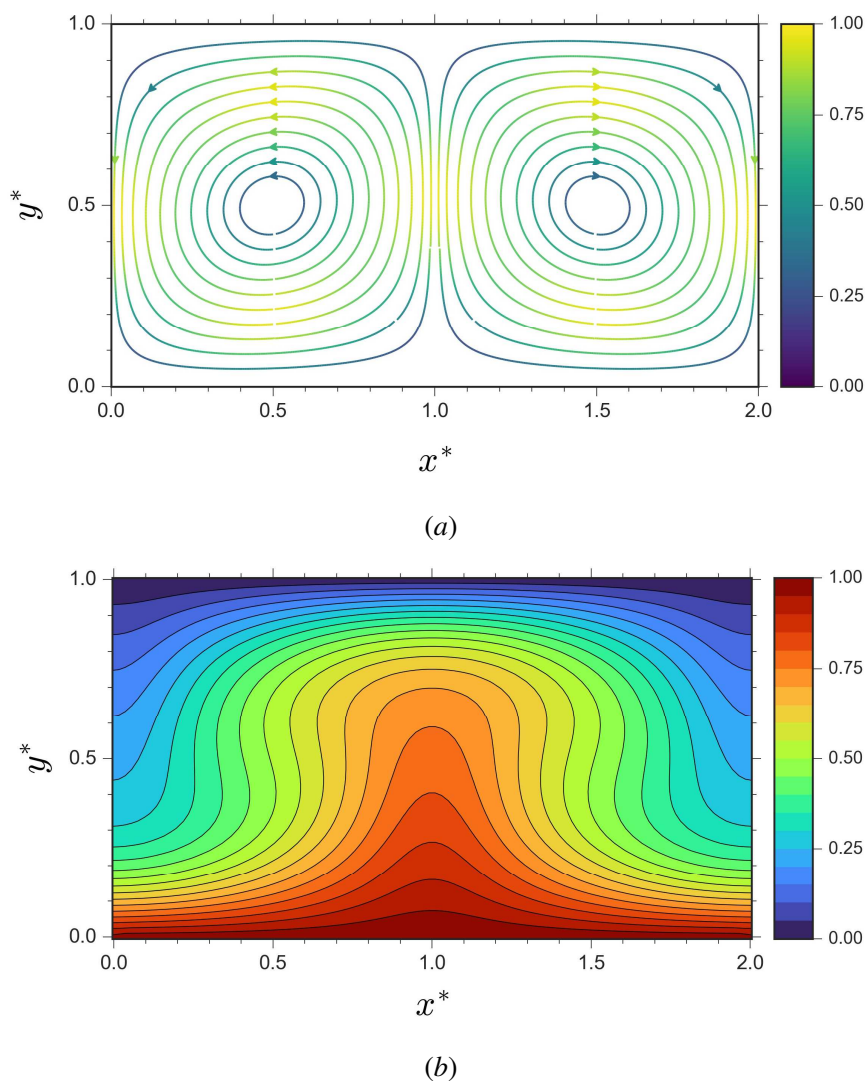
Figure 4.3. Flow profiles for steady Rayleigh-Bènard convection with constant hot temperature at the bottom wall under $Ra = 5 \times 10^3$ and $Pr = 0.71$, displaying (a) streamlines and (b) isotherms.
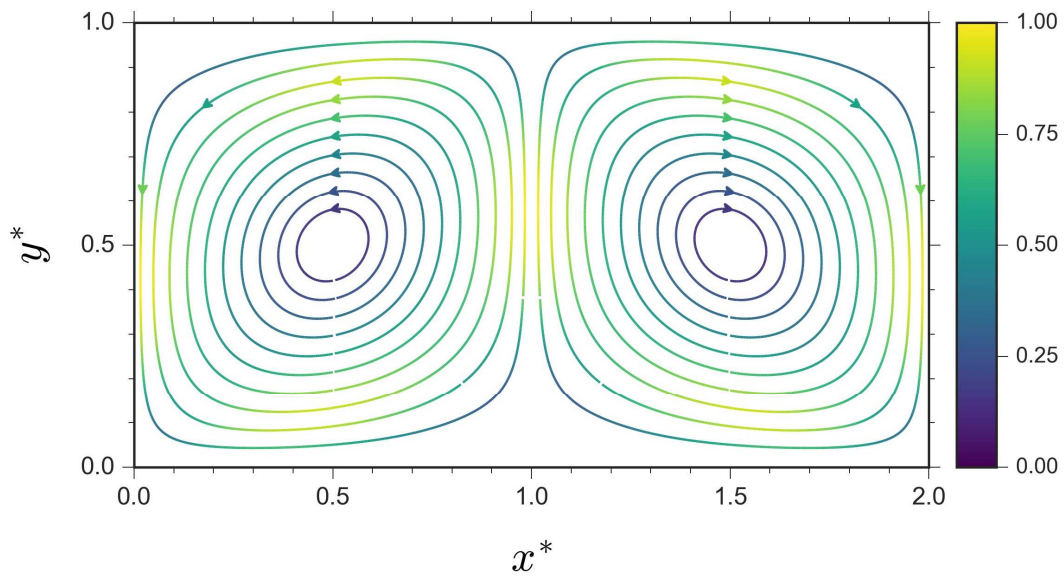
(a)
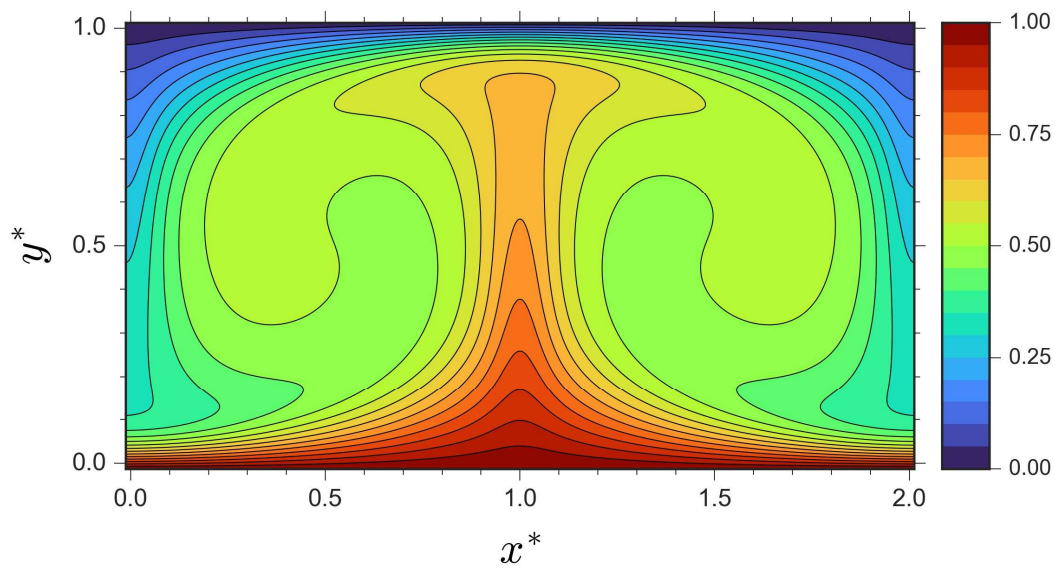
(b)

Figure 4.4. Flow profiles for steady Rayleigh-Bènard convection with constant hot temperature at the bottom wall under $Ra = 1 \times 10^5$ and $Pr = 0.71$, displaying (a) streamlines and (b) isotherms.

Figure 4.5 demonstrates the profile of average Nusselt number captured from numerical simulation. Therein, the values of average Nusselt number from the considered interval of Rayleigh

numbers were compared with the benchmark results from earlier studies of Clever and Busse (1974), He *et al.* (1998) and Inamuro *et al.* (2002). Additionally, the results were also compared with the empirical formula proposed by He *et al.* (1998). As can be seen in the figure, the simulation results captured from the modified LBM scheme agree well with the outcomes from former examinations, as well as the empirical formula. Nevertheless, minor deviation from the results of empirical formula was observed at high Rayleigh number condition. It seems that the present LBM scheme slightly underestimates the heat transfer performance at high Rayleigh number simulation. Overall, the LBM scheme adopted in the current work demonstrate very good conformity with the benchmark results, advocating the capacity and reliability of the proposed LBM scenario.
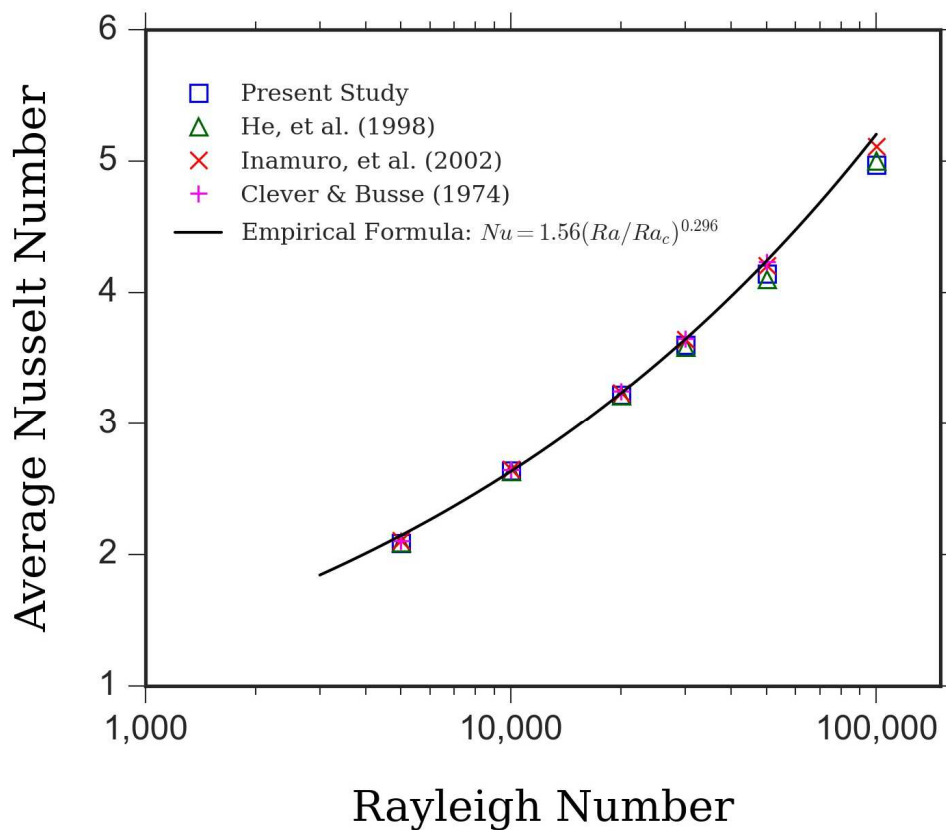
Figure 4.5. Relationship between the average Nusselt number and the Rayleigh number. Numerical results from the present study was compared with outcomes of Clever and Busse (1974), He *et al.* (1998), Inamuro *et al.* (2002), and the empirical formula of $Nu = 1.56(Ra/Ra_c)^{0.296}$.

4.3 Flow Characteristics of Unsteady Rayleigh-Bènard Convection under Time-Periodic Temperature Condition

Following validation of the proposed second-order accurate single-relaxation-time (SRT) LBM scheme, the corresponding numerical technique was used for simulating unsteady Rayleigh-Bènard convection triggered by time-periodic thermal boundary condition. For the purpose of investigating the general characteristics of the problem at hand, the unsteady Rayleigh-Bènard system was simulated under the conditions of fixed Rayleigh and Prandtl numbers, namely $Ra = 5 \times 10^4$ and $Pr = 6.0$ (water). The dimensionless amplitude A^* and frequency f_λ^* of the hot oscillation wall were also kept fixed at 0.3 and 5, respectively. Simulation was performed until $t^* = 1$. Boundary conditions for fluid population were invoked using the bounce-back technique described by equation (2.70). Meanwhile, boundary treatments for thermal population were assigned by the anti-bounce back method depicted by equation (2.73).

Figure 4.6 shows the profile of dimensionless temperature at the bottom hot wall. As indicated in the figure, the temperature condition at the hot wall demonstrates oscillatory behavior around $\overline{\Theta}_{hot} = 1$.
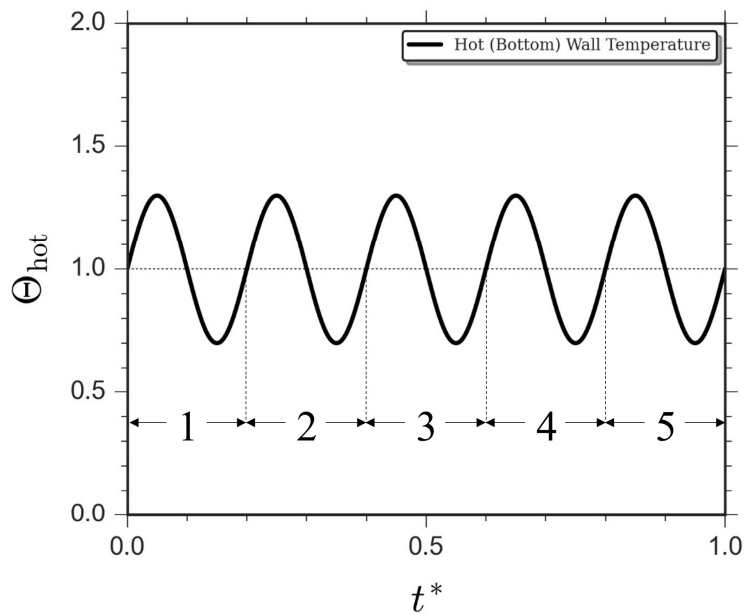
Figure 4.6. Profile of dimensionless temperature at the bottom hot wall during simulation of unsteady Rayleigh-Bènard convection with $A^* = 0.3$ and $f_\lambda^* = 5$.

To investigate the system, the last two cycles of the temperature oscillation were considered in detail. Figure 4.7 shows the last two cycles of the time-periodic oscillation. Therein, n designates the total number of cycles, which in this case is 5. Subsequently, the corresponding cycles were classified into two regions, namely the region of increasing temperature (identified by red-color dots and alphabets) and the region of decreasing temperature (identified by blue-color dots and alphabets). The region of increasing temperature follows the path described by *a-b-c-d-e,* while the region of decreasing temperature follows the path designated by *e-f-g-h-i*. Such definition will be referred to hereinafter. Figure 4.8 displays the streamlines and isotherms of the first-half of the raising temperature region (path *a-b-c*), while Figure 4.9 presents the profiles of the second-half of similar region (path *c-d-e*). The flow characteristics of the first- (path *e-f-g*) and second-half (path *g-h-i*) of the decreasing temperature region were shown in Figure 4.10 and Figure 4.11, respectively.
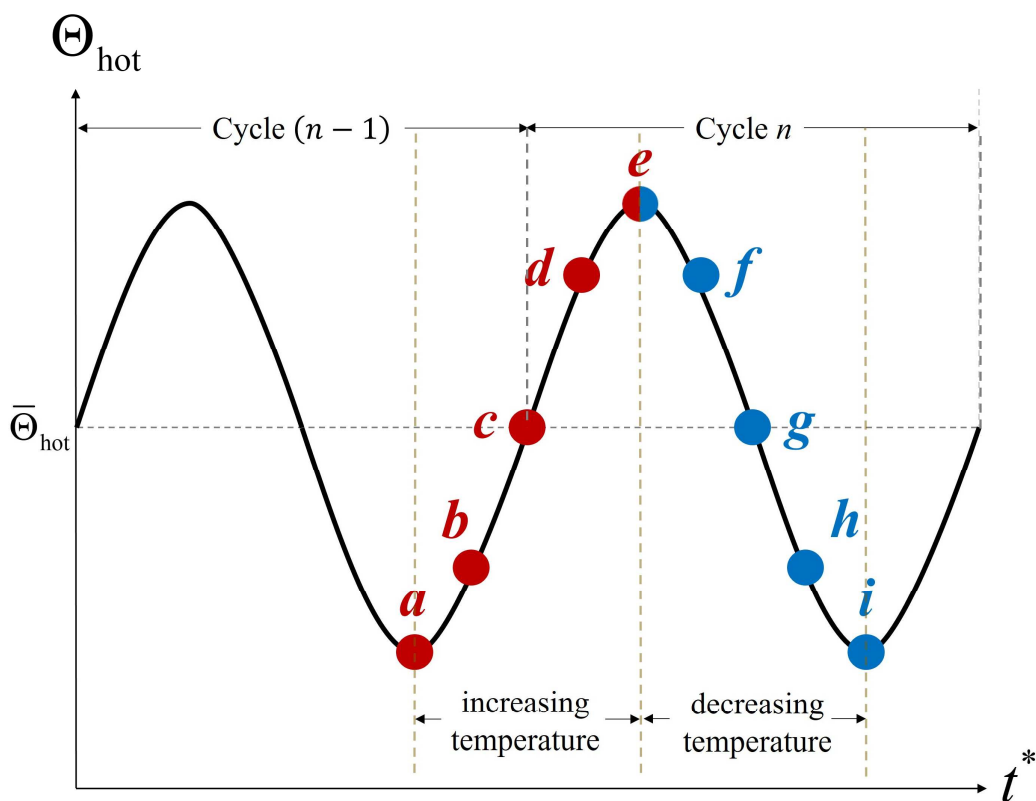
Figure 4.7. The last two cycles of the time-periodic dimensionless temperature, illustrating increasing trend of temperature (red-color alphabets) and decreasing trend of temperature (blue-color alphabets)

(a)

(b)

(c)
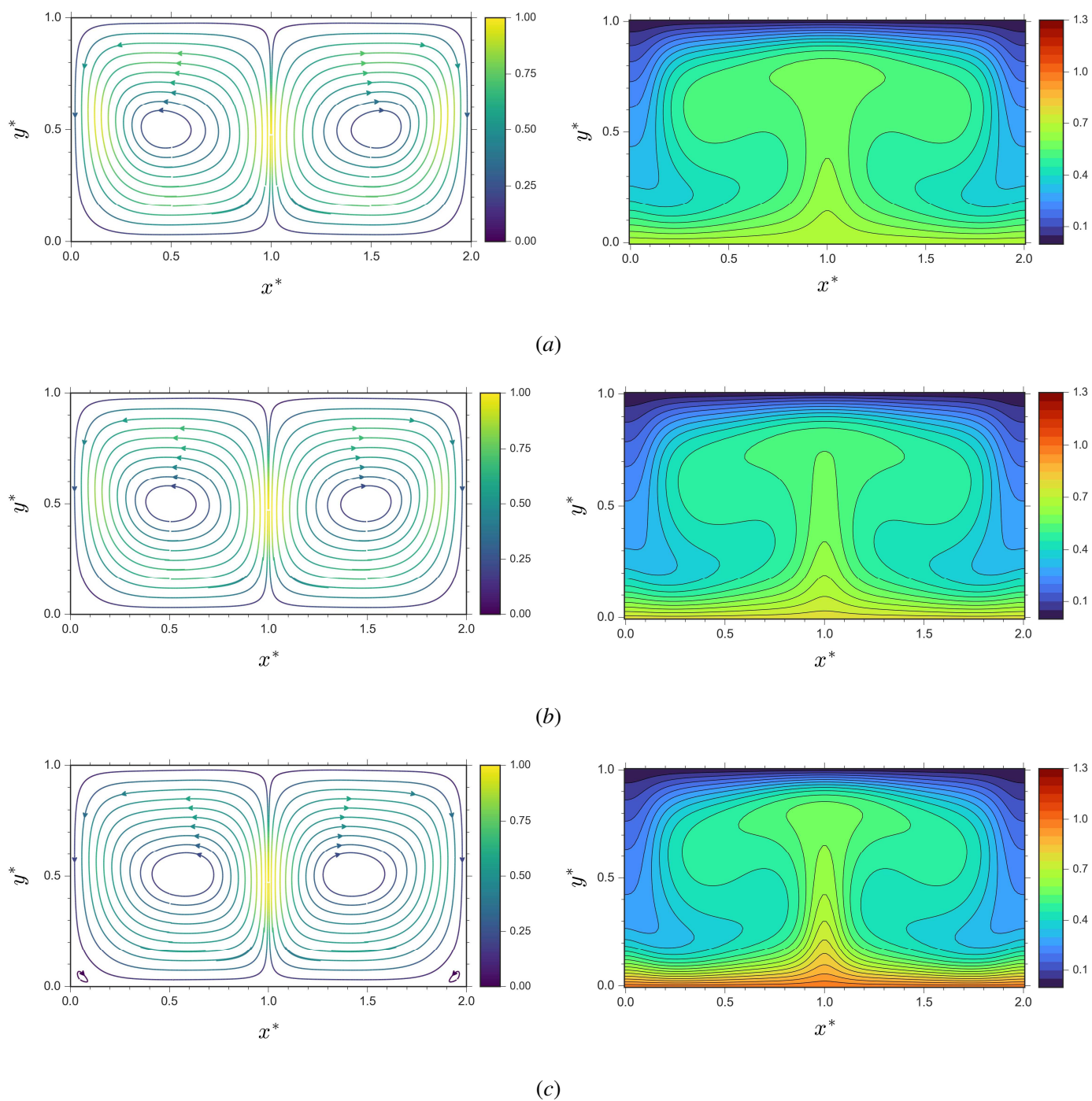
Figure 4.8. Streamlines and isotherms profiles of the first-half segment of the increasing temperature (path *a-b-c*). The flow profiles were shown according to the location of (*a*) point *a*, (*b*) point *b* and (*c*) point *c* of the defined region.

(a)

(b)

(c)
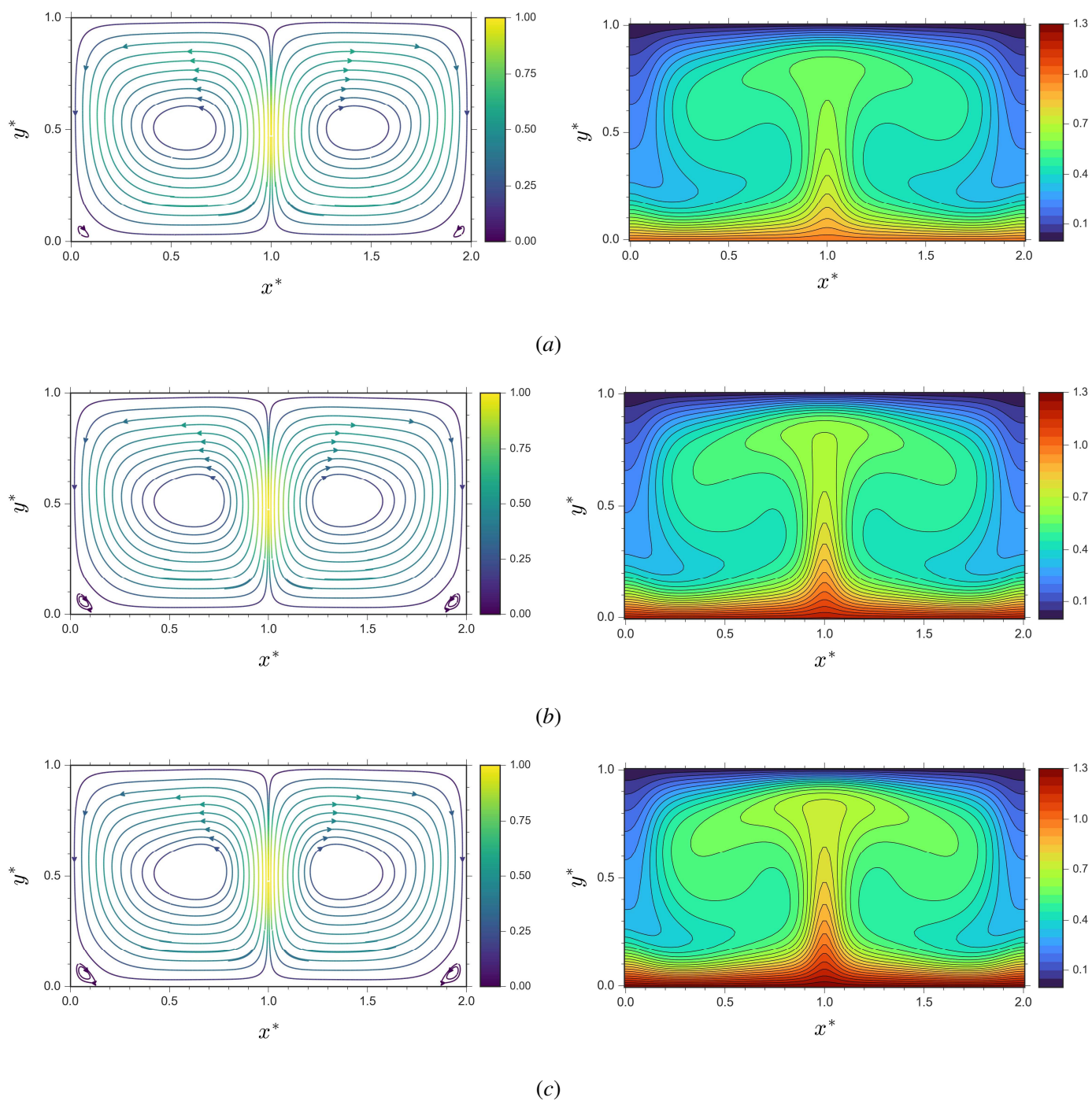
Figure 4.9. Streamlines and isotherms profiles of the second-half segment of the increasing temperature (path *c-d-e*). The flow profiles were shown according to the location of (*a*) point *c*, (*b*) point *d* and (*c*) point *e* of the defined region.
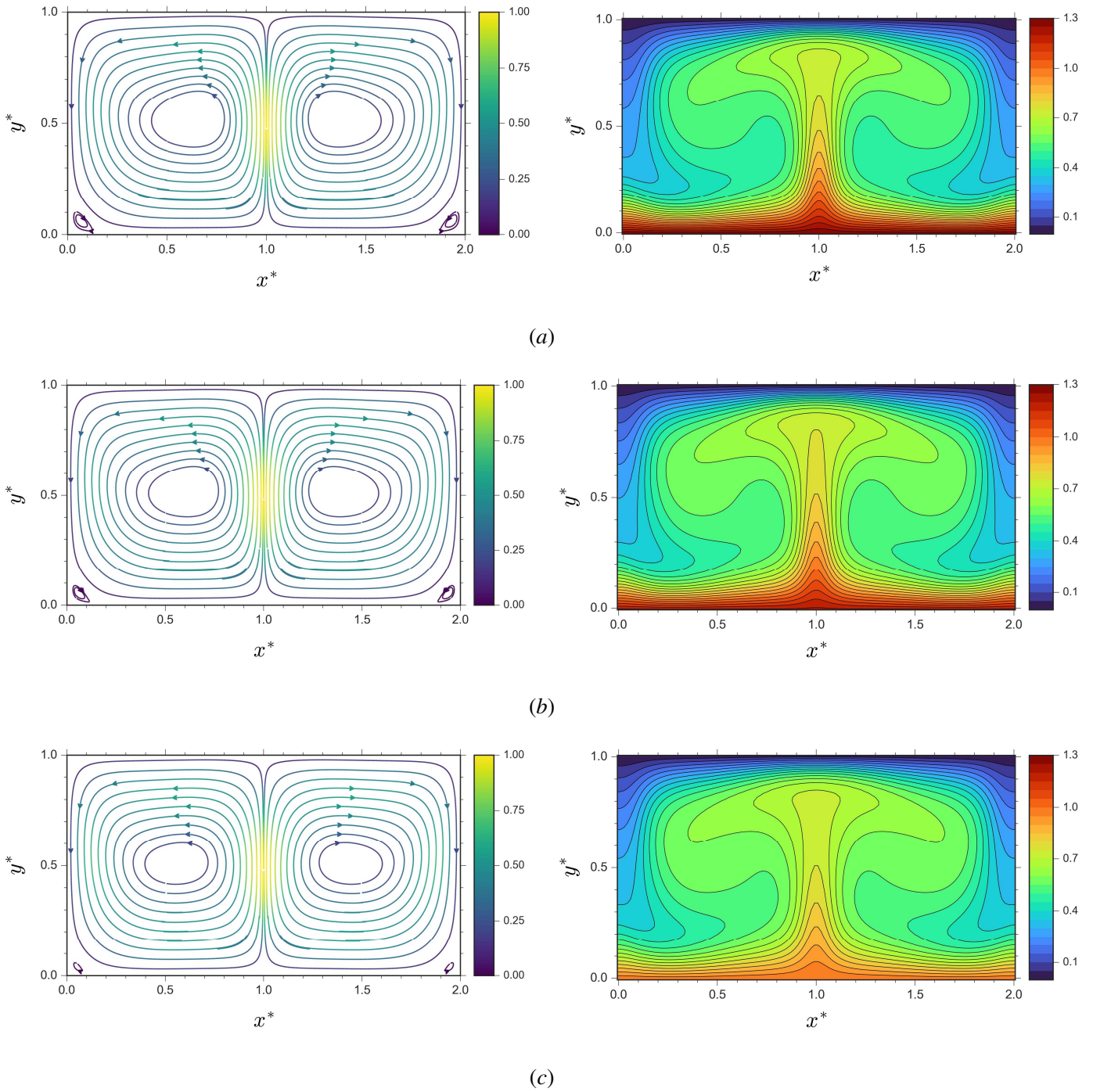
Figure 4.10. Streamlines and isotherms profiles of the first-half segment of the decreasing temperature (path *e-f-g*). The flow profiles were shown according to the location of (*a*) point *e*, (*b*) point *f* and (*c*) point *g* of the defined region.

(a)

(b)

(c)
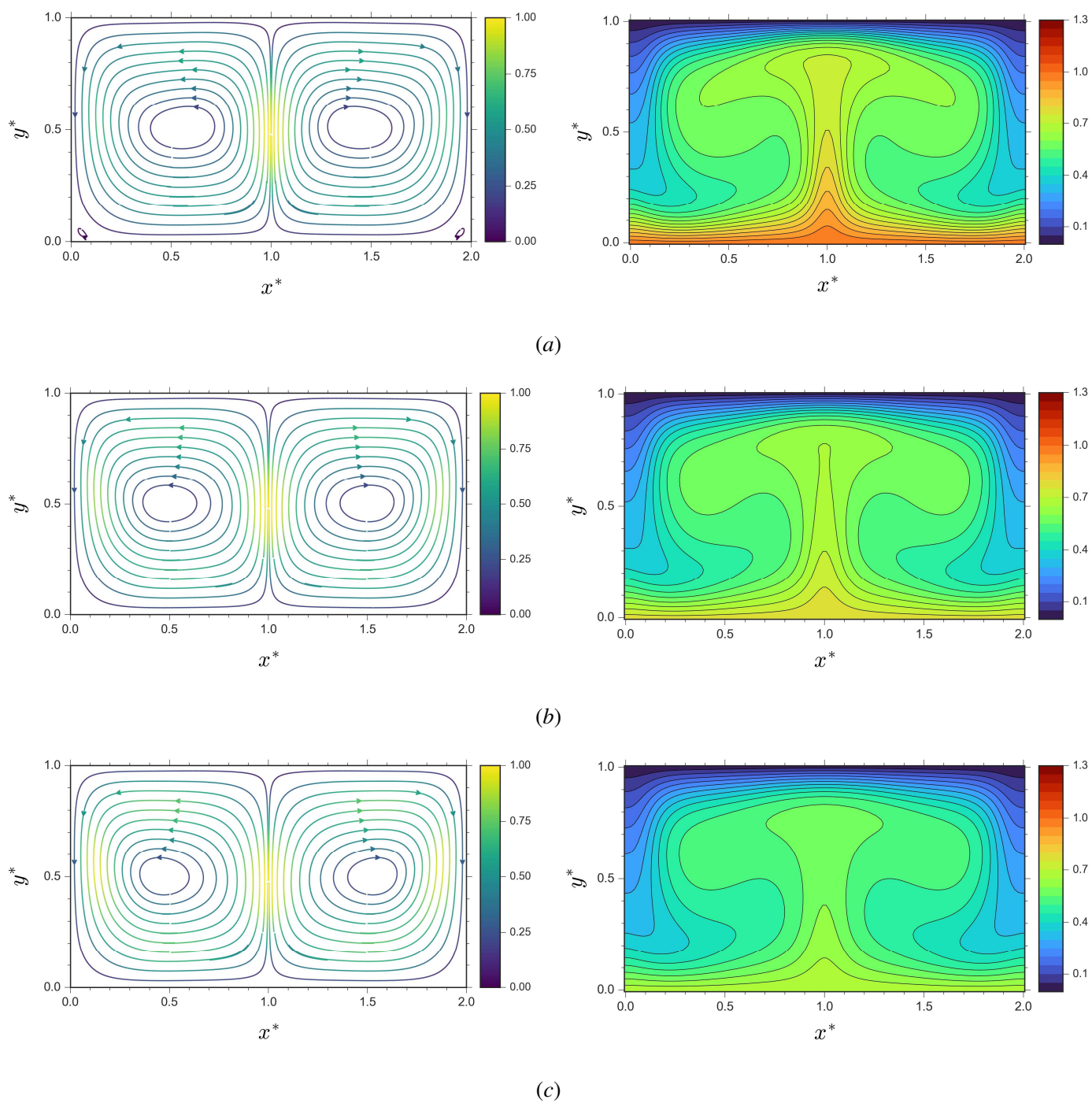
Figure 4.11. Streamlines and isotherms profiles of the second-half segment of the decreasing temperature (path *g-h-i*). The flow profiles were shown according to the location of (*a*) point *g*, (*b*) point *h* and (*c*) point *i* of the defined region.

Performing careful inspection upon the flow profiles displayed in the above figures, the key features of the problem at hand can be configured. The streamlines characteristics were principally governed by two main circulations that filled the entire domain. The two primary cells were symmetric. The left-side primary cell flows in counterclockwise direction, while the cell on the opposite side moves in clockwise direction. At point *a*, the streamlines were tilted to the respective vertical sides of the domain with moderate size of central cell. The streamlines demonstrated moderate thermal dissemination correspond to the low temperature condition of the oscillating hot wall. Such features prevailed until the simulation reached point *b*.

As the simulation proceeds to point *c*, small secondary cells began to develop at the low corners of the enclosure. This was followed simultaneously by the change in the streamlines in which the central cell of the streamlines became larger and the form of the streamlines were tilted to the left-portion of the cavity. As the temperature condition escalates in points *d* and *e*, the secondary cells intensified in both magnitude and intensity. The peak condition of the secondary cell occurred at point e, which is the peak temperature condition of the corresponding path. Later on, following decreasing temperature path of the oscillating hot wall, the secondary cell diminished gradually until vanished entirely at point *h*. This was followed concurrently by the shift of the streamlines that returned back to the right-tilted form. At point *i*, the profiles exhibit similar characteristics as in point *a*.

Figure 4.12 shows the profiles of average Nusselt number at the hot (Nu_{hot}) and cold (Nu_{cold}) walls of the domain. Therein, the profile of Nu_{cold} exhibits a phase-lag in comparison with the Nu_{hot}. The phase lag in Nu_{cold} occurred due to the effect of oscillation in hot wall boundary requires some time to penetrate into the domain. Moreover, before the effect of particular change in temperature propagates into the entire domain, the corresponding temperature at the hot wall has already shifted. This causes the effect of the prior temperature change to be ceased before it can penetrate into the whole domain. This is showed in Figure 4.12, in which the fluctuation of Nu_{cold} exhibit smaller amplitude than the corresponding fluctuation of Nu_{hot}.
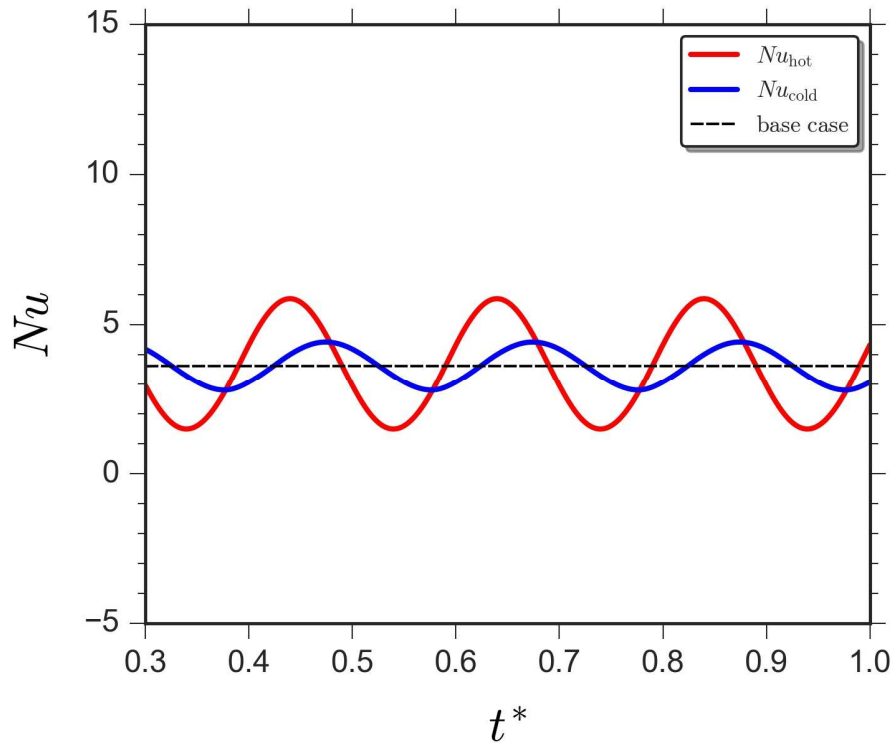
Figure 4.12. Profiles of average Nusselt number at the hot (Nu_hot) and cold (Nu_cold) boundary walls.

Figure 4.13 displays the hysteresis plot of the hot (Nu_hot) and cold (Nu_cold) Nusselt numbers. Therein, the change in Nu_hot in corresponds with the oscillating hot wall temperature encompasses wide interval of values, namely $1 \leq Nu_\text{hot} \leq 6$. Consequently, the corresponding profile demonstrates steep gradient. On the other hand, the change in Nu_cold due to the oscillating hot wall only involves narrow interval of values, that is $3 \leq Nu_\text{hot} \leq 4$, and the corresponding profile exhibits much less steep gradient. This indicates the small changes in heat transfer performance due to the oscillating hot wall temperature. This is parallel with previous exposition that the contribution of hot wall temperature change does not penetrate entirely into the flow domain. The relatively rapid change in the hot wall temperature causes the effect of previous change to be ceased before it can penetrate into the whole domain, leaving such effect to be perceived only moderately at the cold wall of the enclosure.
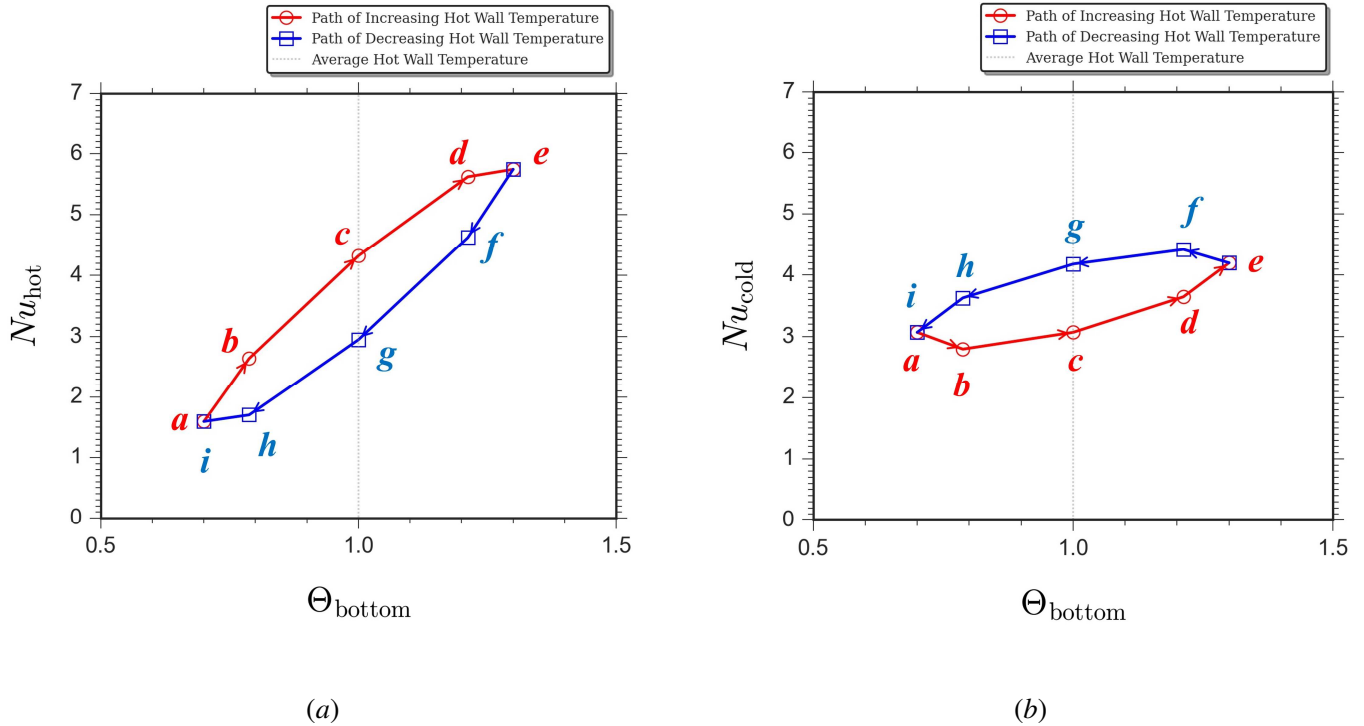
Figure 4.13. Hysteresis of (a) Nu_{hot} and (b) Nu_{cold}.

4.4 Effect of Amplitude on the Flow Characteristics

To examine the implications of amplitude of the oscillating hot wall to the characteristics of fluid flow and heat transfer of the unsteady Rayleigh-Bènard convection, simulations were undertaken upon similar two-dimensional configuration with varying dimensionless amplitude, namely $A^* = 0.5$ and 0.8. The dimensionless frequency was kept constant at $f_\lambda^* = 5$. Simulations were performed under constant values of Rayleigh ($Ra = 5 \times 10^4$) and Prandtl ($Pr = 6.0$) numbers.

Figure 4.14 shows the heat transfer performances for three different values of dimensionless amplitude. Therein, the profiles of Nu_{hot} and Nu_{cold} for $A^* = 0.3, 0.5$ and 0.8 were presented for an interval of dimensionless time $0.2 \leq t^* \leq 1$. As expected, system with larger dimensionless amplitude demonstrates larger fluctuation in Nu_{hot} and Nu_{cold}. Such condition indicates that the effect of oscillating hot wall penetrates deeper into the entire domain as the amplitude gets larger.

Another conspicuous feature lies in the form of the oscillating Nusselt numbers. Careful inspection of Figure 4.14 reveals that at $A^* = 0.8$, the fluctuation characteristics of Nu_{hot} and Nu_{cold}

deviate from the typical symmetric form of sinusoidal function. This fact was elaborated further in Figure 4.15. Therein, the hysteresis profiles of Nu_{hot} and Nu_{cold} for the case of $A^* = 0.8$ demonstrate deviations from symmetric feature.
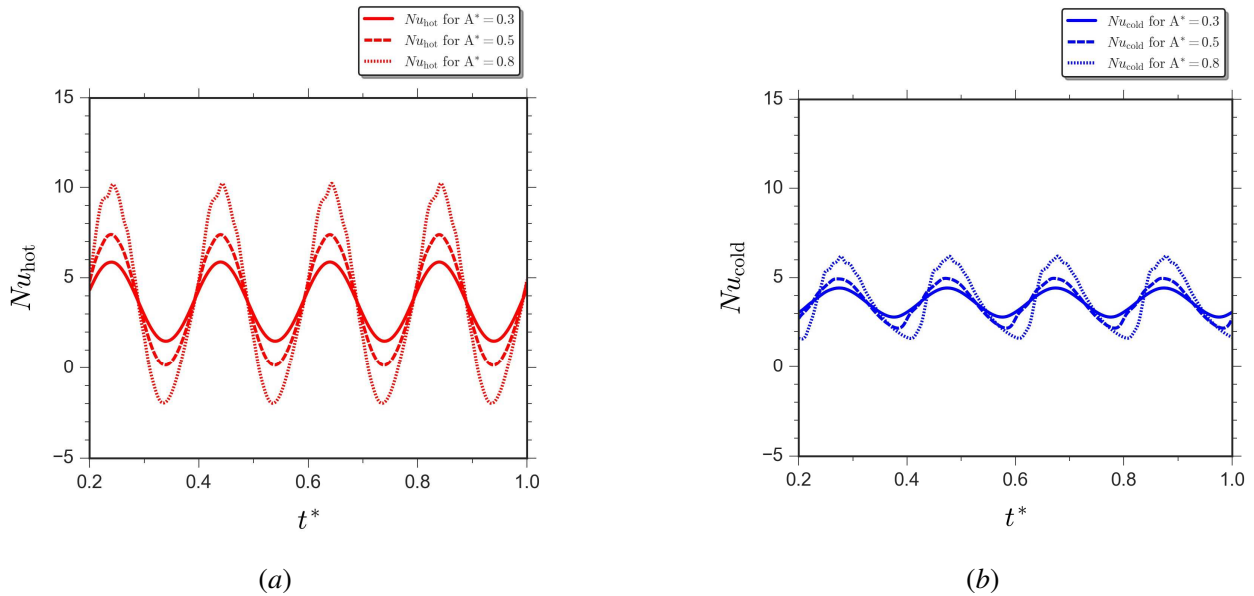
Figure 4.14. Profiles for (a) Nu_{hot} and (b) Nu_{cold} for different values of dimensionless amplitude A^*.
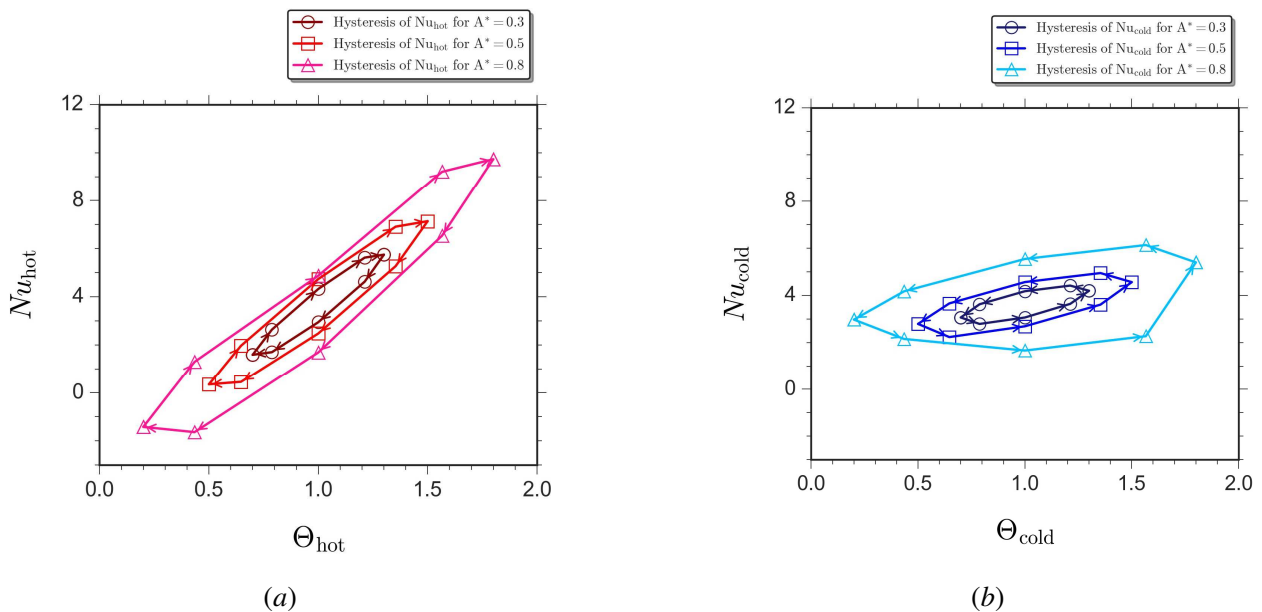
Figure 4.15. Hysteresis plot for (a) Nu_{hot} and (b) Nu_{cold} for different values of dimensionless amplitude A^*.
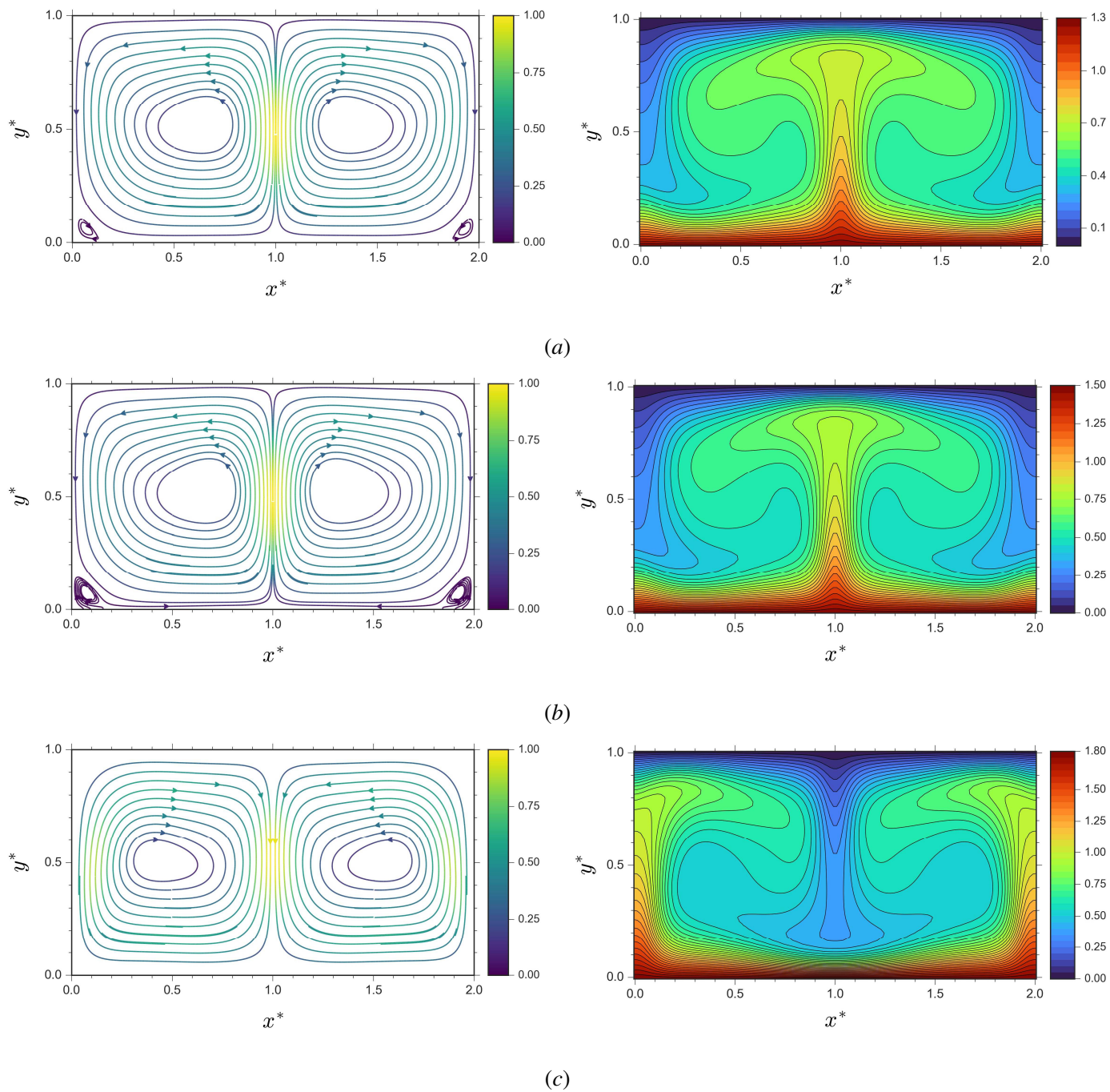
Figure 4.16. Streamlines and isotherms profiles at the peak temperature oscillation (point *e*), showing the contours at (*a*) $A^* = 0.3$ (*b*) $A^* = 0.5$ and (*c*) $A^* = 0.8$.

To understand the departure of heat transfer profiles from symmetric condition for the case of $A^* = 0.8$, the corresponding flow profiles need to be considered. For the sake of brevity, only the flow characteristics at the peak temperature of the oscillating condition (point e) were displayed. Figure 4.16 exhibits such attributes. As can be seen in the figure, the magnitude and intensity of the secondary cells at the bottom corners of the domain were increased as the amplitude was escalated from $A^* = 0.3$ to $A^* = 0.5$. Herein, the heat transfer performance was simultaneously reinforced.

Interesting phenomena occurred at $A^* = 0.8$. Here, the flow profiles demonstrate contrasting behavior from the preceding amplitudes. The materials seemed to flow at opposing directions, where the hot fluid raised from the side corners of the domain instead of the central region. Consequently, the profile of thermal dissemination exhibits reverse condition from the previous cases. This particular behavior existed presumably due to the backflow that occurs when the Nu_{hot} profile reached negative value. At this situation, the temperature of the fluid within the domain was essentially higher than the condition at the bottom hot wall, causing backward flow from the hotter portion at the domain to the cooler upper and bottom parts. Such condition might inflicted the observed reversed-flow behavior at high oscillation amplitude. Further study is required to elaborate deeper understanding of the flow characteristics during high amplitude oscillating condition.

4.5 Effect of Frequency on the Flow Characteristics

To explain the effect of distinct frequency on the fluid flow and heat transfer characteristics of the unsteady Rayleigh-Bènard convection, the problems with varying dimensionless frequency f_λ^* were simulated. Here, the dimensionless amplitude A^* was kept at constant value of 0.3. Similar with the earlier cases, the Rayleigh and Prandtl numbers were kept firm at $Ra = 5 \times 10^4$ and $Pr = 6.0$. The dimensionless frequencies of $f_\lambda^* = 2, 4, 5, 8, 10$ and 12 were incorporated into the examination.

Figure 4.17 displays the profiles of Nu_{hot} and Nu_{cold} for all the considered frequencies. It is clear that increasing frequency reflects in increasing fluctuation of Nu_{hot} and Nu_{cold}. At $f_\lambda^* = 2$, the difference between Nu_{hot} and Nu_{cold} was small, indicating that during this condition, the effect of oscillating hot wall penetrates deep into the domain. This is understandable because at small frequencies, the hot temperature wall changes slowly, allowing sufficient time for that particular changes to propagate deep within the domain. As f_λ^* gets larger, the hot temperature changes more rapidly, causing the discrepancy between Nu_{hot} and Nu_{cold} to be more profound. As such, the effect of temperature change occupies lesser time to propagate inside the domain, causing smaller

oscillation in Nu_{cold}. The assessment of unsteady Rayleigh-Bènard convection under higher frequency condition will be addressed in the forthcoming chapter.

(a)

(b)

(c)

(d)

$$(e) \qquad\qquad (f)$$
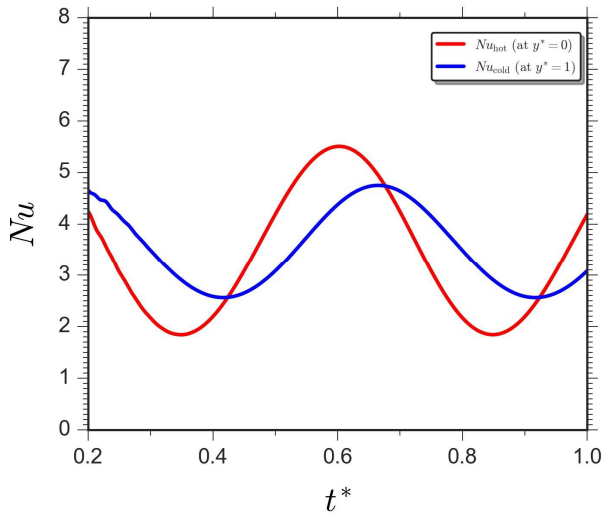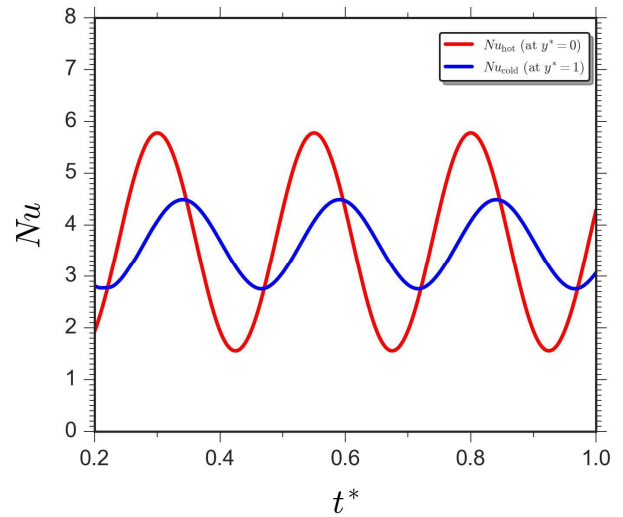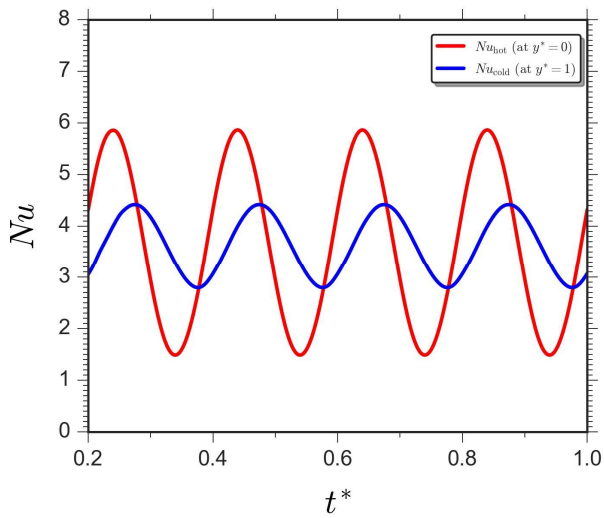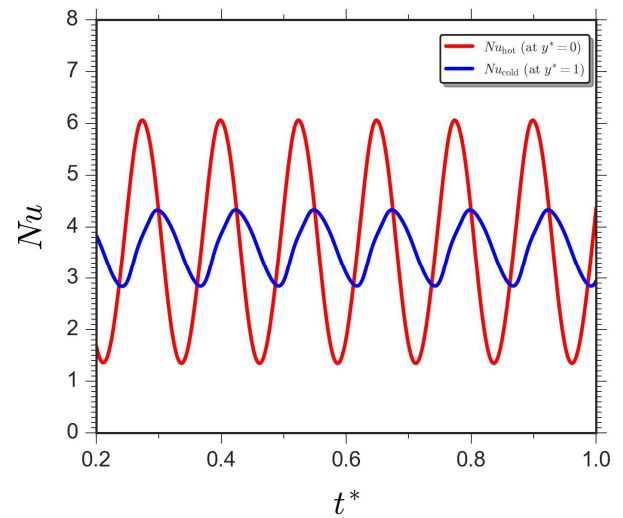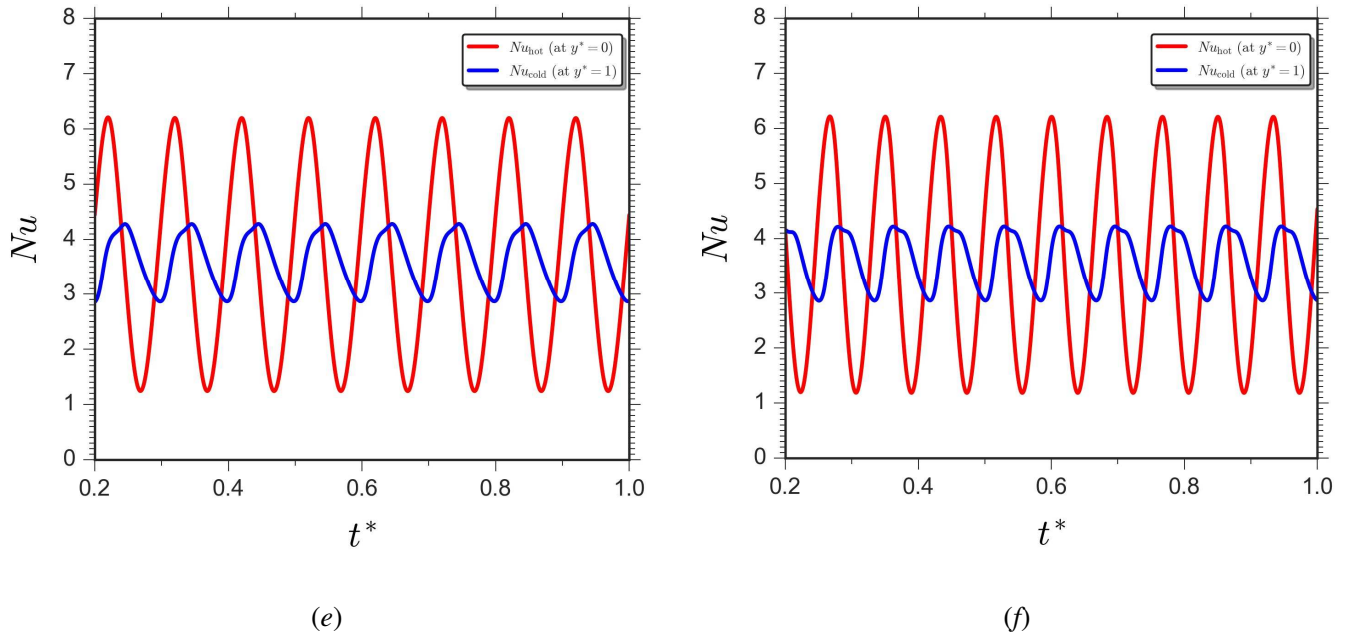
Figure 4.17. Profiles of average Nusselt number at the hot (Nu_{hot}) and cold (Nu_{cold}) walls for unsteady Rayleigh-Bènard convection with varying dimensionless frequency of (*a*) $f_\lambda^* = 2$, (*b*) $f_\lambda^* = 4$, (*c*) $f_\lambda^* = 5$, (*d*) $f_\lambda^* = 8$, (*e*) $f_\lambda^* = 10$, and (*f*) $f_\lambda^* = 12$.

4.6 Summary

In the present chapter, the unsteady Rayleigh-Bènard convection triggered by time-periodic condition of the hot wall boundary has been investigated in detail. The key findings of the present chapter were as follows:

1. Prior to simulating the unsteady problem, the proposed second-order accurate LBM scheme was tested upon simulating steady Rayleigh-Bènard convection with length-to-width aspect ratio equal to two. The modified LBM scheme demonstrates very good agreement with numerical benchmark from earlier studies, justifying its accuracy and reliability.

2. Flow characteristics of the unsteady Rayleigh-Bènard convection were governed by the amplitude and frequency of the corresponding time-periodic hot wall oscillation. Examining in detail the behavior within one cycle of increasing and decreasing temperature paths provide a way to reveal the flow behavior of the corresponding physical system.

3. Generally, the flow characteristics of unsteady Rayleigh-Bènard convection were composed of the primary circulation in the body of the cavity and the small secondary cell that emerged at the

bottom corners of the cavity. It was found that the appearance and disappearance of the secondary cell depend on the path of increasing and decreasing hot wall temperature, respectively.

4. Amplitude of the hot wall oscillation occupies indispensable role to the characteristics of the flow of the problem at hand. The higher the amplitude, the higher the magnitude of fluctuation of the hot and cold Nusselt numbers. However, when the amplitude is excessively high, additional physical intricacy in terms of backflow emerged within the system, rendering it to be challenging. Further research is required in order to disclose the complex behavior of unsteady Rayleigh-Bènard convection at high amplitude of oscillating hot wall.

5. Frequency of the hot wall contributes upon the degree of penetration of the hot wall changes into the domain. The higher the frequency, the lesser time is available for the effect of a particular temperature change to be perceived by the flow domain. Consequently, smaller fluctuation was encountered in the profile of Nusselt number at the cold wall.

Chapter 5: Simulation of Unsteady Rayleigh-Bènard Convection under Time-Periodic Boundary Condition: Special Cases of High Frequency

5.1 Unsteady Rayleigh-Bènard Convection under High-Frequency Condition

Unsteady Rayleigh-Bènard convection invoked by high-frequency fluctuation hot wall is an exemplification of an extreme case in which the heat flux contribution from the underground porous geothermal formation varies rapidly with time. Although such situation is rarely encountered in reality, examining the fluid flow and heat transfer characteristics under the effect of rapid fluctuation of the hot wall holds potential to reveal new insight regarding the underlying physics behind it.

For the purpose of examining the flow characteristics of unsteady Rayleigh-Bènard convection under the influence of high-frequency oscillating hot wall, the synthetic cases involving dimensionless frequency $f_\lambda^* = 20$ and 40 were simulated. The dimensionless amplitude of $A^* = 0.3$ was kept constant for both frequencies. The flow domain and boundary conditions were similar to the one defined previously in Figure 4.1. The second-order accurate single-relaxation-time (SRT) LBM schemes for fluid and thermal populations respectively defined by equations (2.20) and (2.32) were adopted to simulate the high-frequency case. The simulations were undertaken under constant Rayleigh and Prandtl numbers of $Ra = 5 \times 10^4$ and $Pr = 6.0$ (water).

Figure 5.1 exhibits the hot (Nu_{hot}) and cold (Nu_{cold}) Nusselt number profiles of the problems at hand. Therein, the most conspicuous feature of high-frequency oscillating system was the strong and active fluctuations of the Nu_{hot}. As the dimensionless frequency was shifted to higher value, the fluctuation of Nu_{hot} became more profound in magnitude and number. Interestingly, the behavior of Nu_{cold} seemed to be unaffected by the vibrant support from the Nu_{hot}. As a matter of fact, careful inspection upon Figure 5.1 discloses that the fluctuation in Nu_{cold} was actually reduced when the dimensionless frequency was increased from 20 to 40. This fact was elucidated in Figure 5.2, where the hysteresis profiles of Nu_{cold} were presented. Therein, the hysteresis profile of Nu_{cold} at $f_\lambda^* = 40$
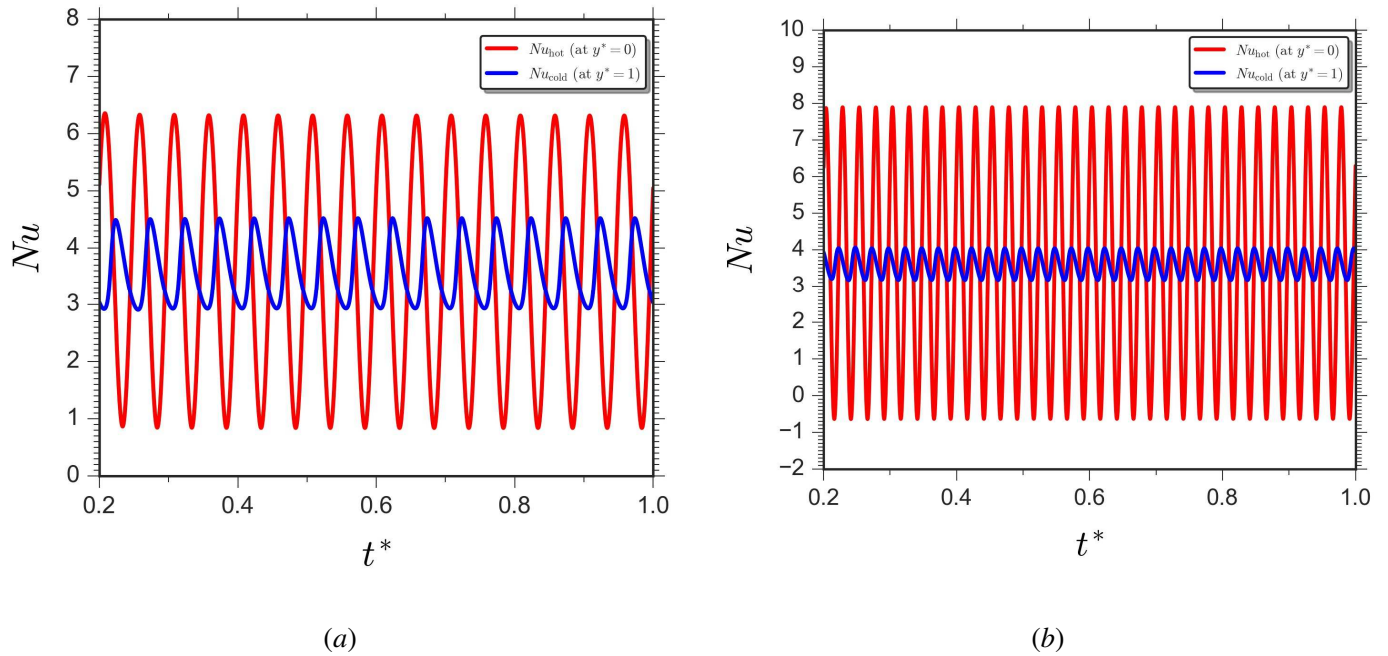
Figure 5.1. Profiles of hot (Nu_{hot}) and cold (Nu_{cold}) Nusselt numbers for high-oscillating frequency of the hot wall temperature, displaying conditions for (a) $f_\lambda^* = 20$ and (b) $f_\lambda^* = 40$.

displays smaller deviation than the case of $f_\lambda^* = 20$. This situation indicates that as the oscillation frequency gets higher, the heat transfer performance was actually reduced.

It is therefore conceivable to infer that at an extremely high frequency value (for example 1,000), the profile of Nu_{cold} would become flat. Such situation reflects that the unrealistically rapid change in frequency is not favorable for heat transfer enhancement in an unsteady Rayleigh-Bènard convection. Future researches are necessary in order to elucidate the intricate behaviors of fluid flow and thermal dissemination in high-frequency oscillation system.
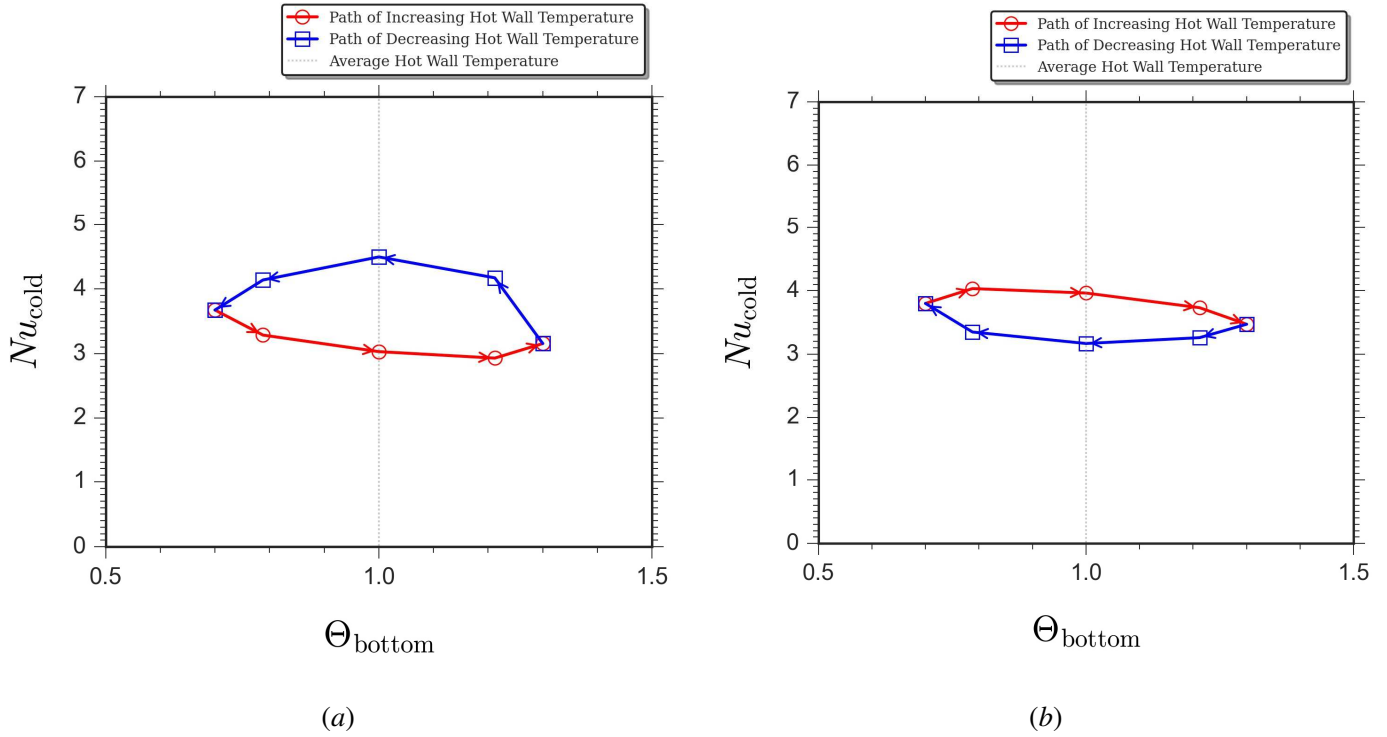
Figure 5.2. Hysteresis of cold Nusselt number for high-oscillating frequency of the hot wall temperature, displaying conditions for (a) $f_\lambda^* = 20$ and (b) $f_\lambda^* = 40$.

5.2 Unsteady Rayleigh-Bènard Convection in High Aspect Ratio Cavity

For unsteady Rayleigh-Bènard convection in a high aspect ratio of the flowing domain, the case of length-to-width aspect ratio equal to 5 was appointed as the exemplification case. The domain configuration was similar with the one used in earlier examinations. However, the aspect ratio was now set to be equal to 5. The dimensionless amplitude and frequency were kept at constant values of $A^* = 0.3$ and $f_\lambda^* = 5$. The Rayleigh ($Ra = 5 \times 10^4$) and Prandtl ($Pr = 6.0$) numbers were kept constant as well.

Figure 5.3 displays the streamlines and isotherms associated with the bottom and top position of the oscillating hot wall. Apparently, the effect of oscillating hot wall fluctuation manifests in the intermittent alteration of streamlines cells. Here, a complex three-pair of circulating flow emanates during the fluctuation path. The isotherms exhibit three plumes of mixing zone between the hot and cold water.
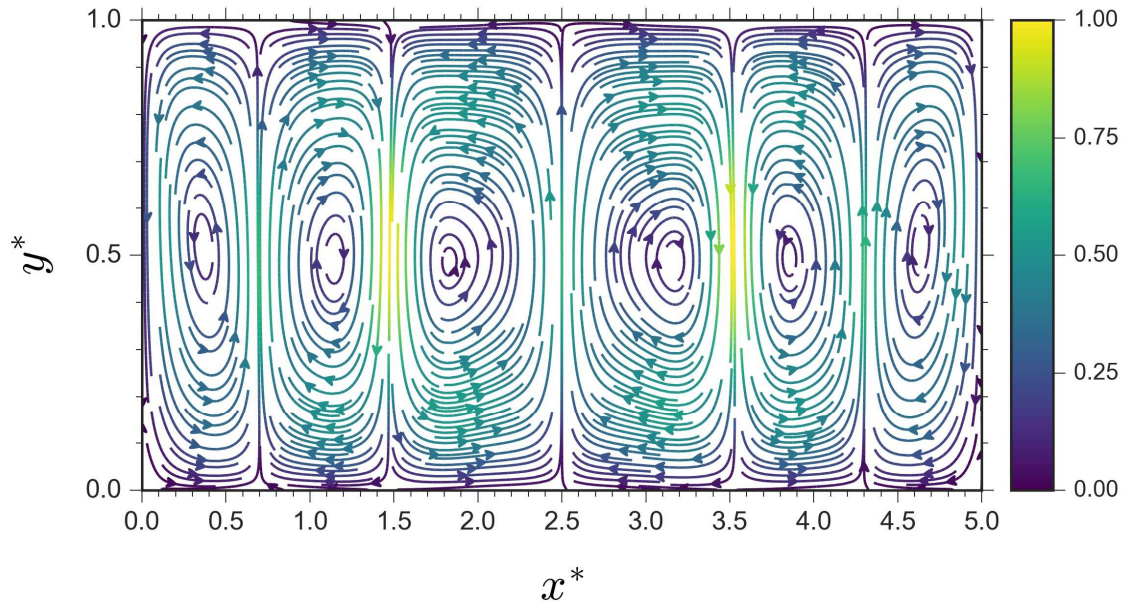
(*a*)
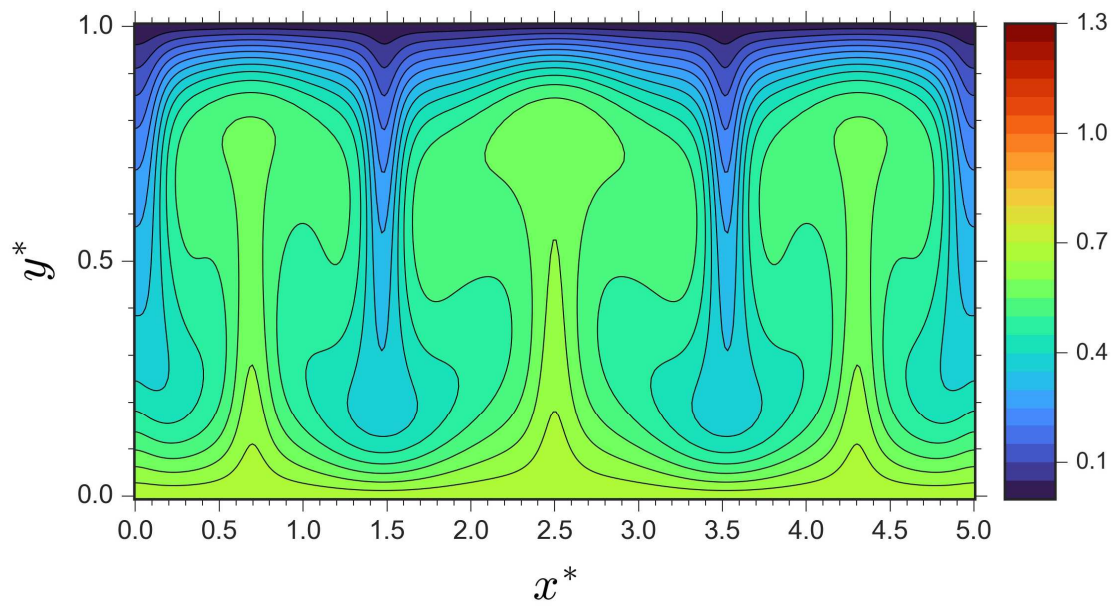
(*b*)
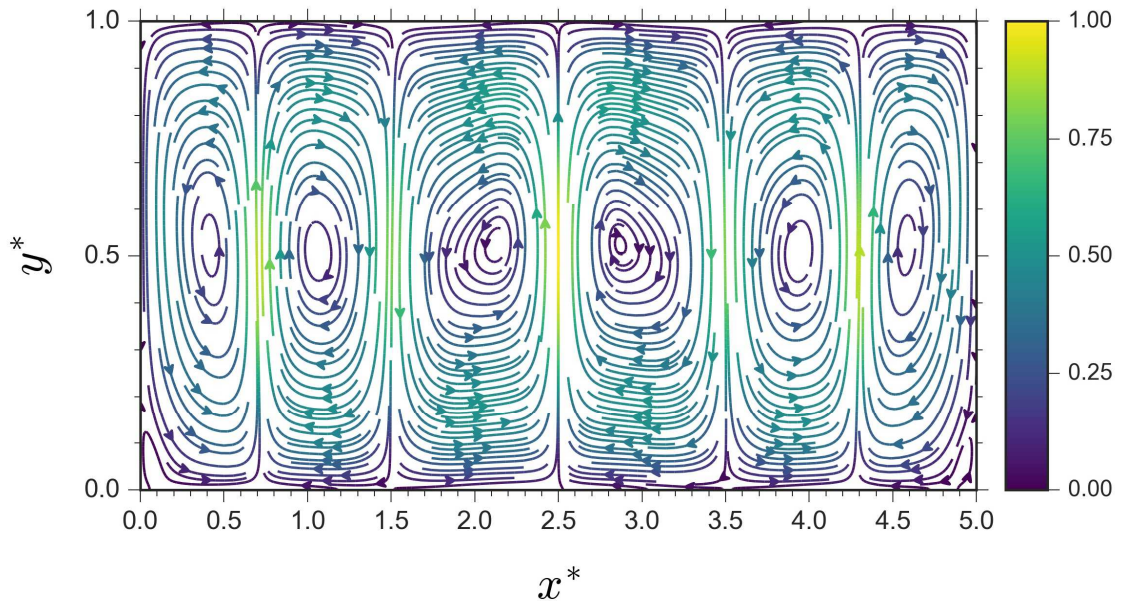
(*c*)
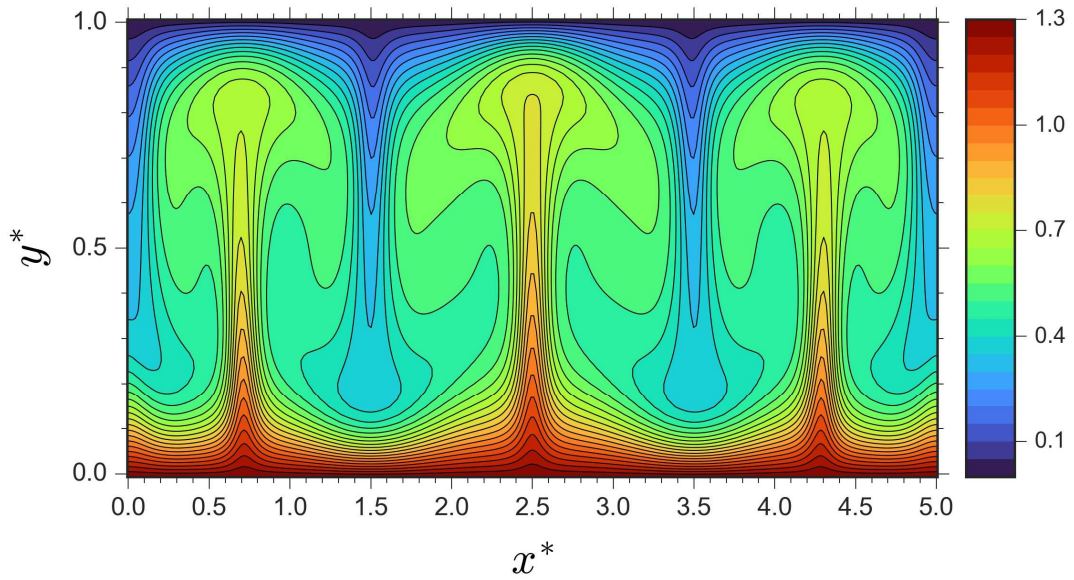
(*d*)

Figure 5.3. Streamlines and isotherms of the unsteady Rayleigh-Bènard convection in a cavity with aspect ratio = 5, displaying (a) streamlines, (b) isotherms at the bottom temperature position (point *a* of Figure 4.7), (c) streamlines and (d) isotherms at the peak temperature position (point *e* of Figure 4.7).

Figure 5.4 illustrates the heat transfer performance in terms of hot (Nu_{hot}) and cold (Nu_{cold}) Nusselt numbers. The figure indicates almost similar feature as the one observed in low aspect ratio of 2. The only visible discrepancy was the presence of minor intermittent feature of both Nusselt number profiles at the early period of the simulation.
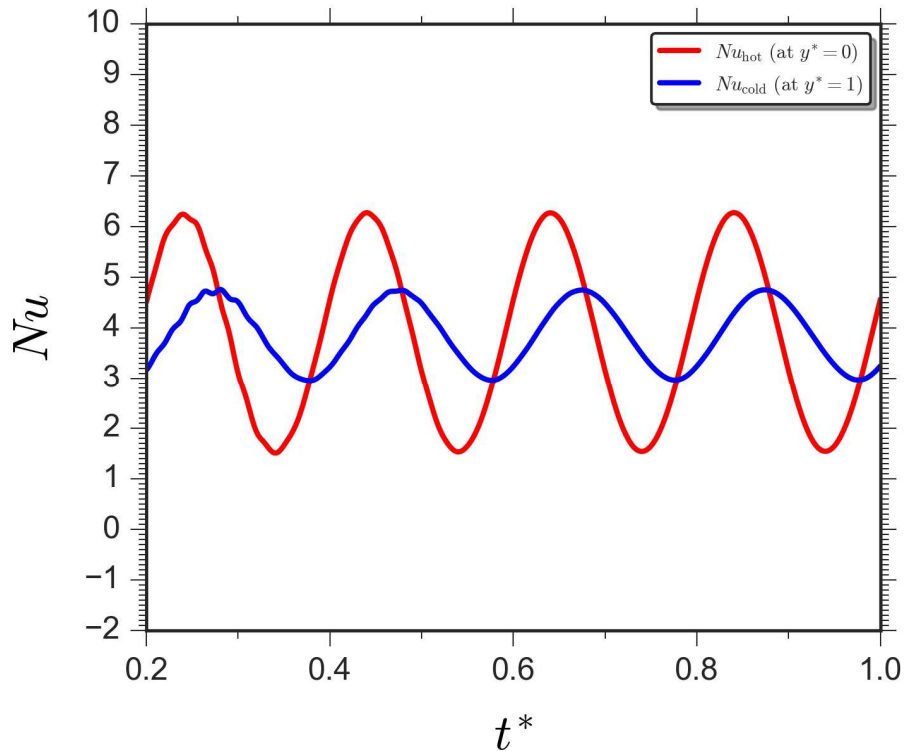
Figure 5.4. Profiles of hot (Nu_{hot}) and cold (Nu_{cold}) Nusselt numbers for unsteady Rayleigh-Bènard convection in high length-to-width cavity aspect ratio of 5.

Unsteady Rayleigh-Bènard convection in high aspect ratio of the enclosure is a challenging topic and the previous studies examining such physical situation is very scarce. The present work offers preliminary outlook into such configuration. Future research regarding this topic is needed in order to reveal more important physical phenomena within.

5.3 Summary

The special cases of unsteady Rayleigh-Bènard convection associating high oscillating frequency and high aspect ratio have been studied. Preliminary outlook was established and the following remarks were noted:

1. The proposed modified LBM scheme with second-order accuracy was able to simulate the extreme cases of heat and thermal convection.

2. For high-oscillating frequency case, there seems to be a limit of frequency value in which above this value, the effect of oscillating wall would be insignificant to the heat transfer process of the system.

3. For high aspect ratio case, the observed streamlines and isotherms profiles showed advanced flow behavior. Nevertheless, the heat transfer performance of the corresponding system was found to be almost equivalent to the case of small aspect ratio. Further studies are required in order to reveal more important physics related to the problem at hand.

Chapter 6: Conclusions and Future Study

6.1 Conclusions

Comprehensive evaluations regarding unsteady Rayleigh-Bènard convection as a representative physical arrangement for the heat and mass transfer occurred in geothermal system have been delivered. The study proposed a modified lattice Boltzmann method (LBM) that demonstrates second-order accuracy in time and spatial coordinates. From the corresponding notion, the single-relaxation-time (SRT) and two-relaxation-time (TRT) LBM schemes were developed.

The numerical evaluations were commenced by addressing the efficacy of disparate LBM scenarios upon simulation of fluid flow and heat transfer phenomena. The sought objective was fulfilled by administering distinct LBM schemes upon two distinctive thermo-hydrodynamics systems, namely the natural convection in a differentially heated cavity and the Rayleigh-Bènard convection.

Following this appraisal was detail evaluation of unsteady Rayleigh-Bènard convection triggered by time-periodic condition of the hot boundary wall. Therein, the effects of amplitude and frequency of the oscillating hot wall were investigated in detail. The analysis was extended to include the special case of high-oscillating frequency of the hot boundary wall.

The key findings of this study are as follows:

1. The presence of considerable discrepancy in computational characteristics of disparate LBM scenarios was seen during the unsteady period of the simulation, which diminished gradually as the simulation advanced towards a steady-state condition.

2. The order of accuracy of the discrete lattice Boltzmann expression was identified as the predominant factor inherent to discrepancy in computational characteristics.

3. The contribution of distinct forcing models upon the heterogeneity in computational behavior was found to be trivial.

4. As a steady-state condition, the LBM scenarios which administer a second-order accurate LBM scenario recovered better numerical accuracy than those scenarios which comprise a first-order accurate model. However, the scheme is challenged by higher computational demand.

6. Generally, the flow characteristics of unsteady Rayleigh-Bènard convection were composed of the primary circulation in the body of the cavity and the small secondary cell that emerged at the bottom corners of the cavity. It was found that the appearance and disappearance of the secondary cell depend on the path of increasing and decreasing hot wall temperature, respectively.

7. Amplitude of the hot wall oscillation occupies indispensable role to the characteristics of the flow of the problem at hand. The higher the amplitude, the higher the magnitude of fluctuation of the hot and cold Nusselt numbers. However, when the amplitude is excessively high, additional physical intricacy in terms of backflow emerged within the system, rendering it to be challenging. Further research is required in order to disclose the complex behavior of unsteady Rayleigh-Bènard convection at high amplitude of oscillating hot wall.

5. Frequency of the hot wall contributes upon the degree of penetration of the hot wall changes into the domain. The higher the frequency, the lesser time is available for the effect of a particular temperature change to be perceived by the flow domain. Consequently, smaller fluctuation was encountered in the profile of Nusselt number at the cold wall.

6. The proposed modified LBM scheme with second-order accuracy occupies capacity to simulate the extreme cases of heat and thermal convection in terms of high-oscillating frequency and high aspect ratio.

7. For high-oscillating frequency case, there seems to be a limit of frequency value in which above this value, the effect of oscillating wall would be insignificant to the heat transfer process of the system.

8. For high aspect ratio case, the observed streamlines and isotherms profiles showed advanced flow behavior. Nevertheless, the heat transfer performance of the corresponding system was found to be almost equivalent to the case of small aspect ratio. Further studies are required in order to reveal more important physics related to the problem at hand.

6.2 Future Study

Few plausible options to extend the numerical investigation of the present study are as follows:

1. The study may be expanded to include the effects of different Rayleigh numbers on the flow characteristics of unsteady Rayleigh-Bènard convection. There is a high possibility that the effects of amplitude and frequency would exhibit distinct characteristics from the present

condition of constant Rayleigh number ($Ra = 5 \times 10^4$). The presence of resonance frequency might be more profound in high Rayleigh number flow.

2. To acquire better mathematical representation of the concurrent heat and mass transfer phenomena pertinent to geothermal system, additional physical complexity, such as inclusion of porous media, may be incorporated into the model.

3. The study can be extended to include more advanced flow conditions, such as heat and mass transfer in a non-Newtonian fluid system.

4. The study can be extended to include advanced flowing material in terms of nanofluids.

5. The convective flow phenomena considered in this study can be extended to incorporate mixed convection system, which is a combination of natural and forced convection.

References

Antohe, B. V. and Lage, J.L. (1996), "Amplitude effect on convection induced by time-periodic horizontal heating", *International Journal of Heat and Mass Transfer*, Vol. 39 No. 6, pp. 1121–1133.

Antohe, B. V. and Lage, J.L. (1997), "The Prandtl number effect on the optimum heating frequency of an enclosure filled with fluid or with a saturated porous medium", *International Journal of Heat and Mass Transfer*, Vol. 40 No. 6, pp. 1313–1323.

Calore, E., Gabbana, A., Kraus, J., Pellegrini, E., Schifano, S.F. and Tripiccione, R. (2016), "Massively parallel lattice–Boltzmann codes on large GPU clusters", *Parallel Computing*, Elsevier B.V., Vol. 58, pp. 1–24.

Çengel, Y.A. and Cimbala, J.M. (2018), *Fluid Mechanics: Fundamentals and Applications*, 4th ed., McGraw-Hill Education, New York.

Clever, R.M. and Busse, F.H. (1974), "Transition to time-dependent convection", *Journal of Fluid Mechanics*, Vol. 65 No. 4, pp. 625–645.

d'Humières, D. and Ginzburg, I. (2009), "Viscosity independent numerical errors for Lattice Boltzmann models: From recurrence equations to 'magic' collision numbers", *Computers and Mathematics with Applications*, Elsevier Ltd, Vol. 58 No. 5, pp. 823–840.

Dixit, H.N. and Babu, V. (2006), "Simulation of high Rayleigh number natural convection in a square cavity using the lattice Boltzmann method", *International Journal of Heat and Mass Transfer*, Vol. 49 No. 3–4, pp. 727–739.

Du, R. and Liu, W. (2013), "A new multiple-relaxation-time lattice boltzmann method for natural convection", *Journal of Scientific Computing*, Vol. 56 No. 1, pp. 122–130.

Ginzburg, I., Verhaeghe, F. and d'Humières, D. (2008), "Two-relaxation-time Lattice Boltzmann scheme: About parametrization, velocity, pressure and mixed boundary conditions", *Communications in Computational Physics*, Vol. 3 No. 2, pp. 427–478.

Goldhirsch, I., Pelz, R.B. and Orszag, S.A. (1989), "Numerical simulation of thermal convection in a two-dimensional finite box", *Journal of Fluid Mechanics*, Vol. 199, pp. 1–28.

Guo, Z., Zheng, C. and Shi, B. (2002), "Discrete lattice effects on the forcing term in the lattice Boltzmann method", *Physical Review E - Statistical Physics, Plasmas, Fluids, and Related Interdisciplinary Topics*, Vol. 65 No. 4, p. 6.

He, X., Chen, S. and Doolen, G.D. (1998), "A Novel Thermal Model for the Lattice Boltzmann Method in Incompressible Limit", *Journal of Computational Physics*, Vol. 146 No. 1, pp. 282–300.

He, X. and Doolen, G.D. (2002), "Thermodynamic foundations of kinetic theory and Lattice Boltzmann models for multiphase flows", *Journal of Statistical Physics*, Vol. 107 No. 1–2, pp. 309–328.

He, X. and Luo, L.S. (1997), "Theory of the lattice Boltzmann method: From the Boltzmann equation to the lattice Boltzmann equation", *Physical Review E - Statistical Physics, Plasmas, Fluids, and Related Interdisciplinary Topics*, Vol. 55 No. 6, pp. 6811–6820.

Inamuro, T., Yoshino, M., Inoue, H., Mizuno, R. and Ogino, F. (2002), "A lattice Boltzmann method for a binary miscible fluid mixture and its application to a heat-transfer problem", *Journal of Computational Physics*, Vol. 179 No. 1, pp. 201–215.

Jami, M., Moufekkir, F., Mezrhab, A., Fontaine, J.P. and Bouzidi, M. (2016), "New thermal MRT lattice Boltzmann method for simulations of convective flows", *International Journal of Thermal Sciences*, Elsevier Masson SAS, Vol. 100, pp. 98–107.

Kao, P.H. and Yang, R.J. (2007), "Simulating oscillatory flows in Rayleigh-Bénard convection using the lattice Boltzmann method", *International Journal of Heat and Mass Transfer*, Vol. 50 No. 17–18, pp. 3315–3328.

Kazmierczak, M. and Chinoda, Z. (1992), "Buoyancy-driven flow in an enclosure with time periodic boundary conditions", *International Journal of Heat and Mass Transfer*, Vol. 35 No. 6, pp. 1507–1518.

Kefayati, G.H.R. (2013), "Lattice Boltzmann simulation of MHD natural convection in a nanofluid-filled cavity with sinusoidal temperature distribution", *Powder Technology*, Elsevier B.V., Vol.

243, pp. 171–183.

Krivovichev, G. V. (2019), "Stability analysis of body force action models used in the single-relaxation-time single-phase lattice Boltzmann method", *Applied Mathematics and Computation*, Elsevier Inc., Vol. 348, pp. 25–41.

Kruger, T., Kusumaatmaja, H., Kuzmin, A., Shardt, O., Goncalo, S. and Viggen, E.M. (2017), *The Lattice Boltzmann Method, Principles and Practice*, Springer International Publishing Switzerland.

Kupershtokh, A.L., Medvedev, D.A. and Karpov, D.I. (2009), "On equations of state in a lattice Boltzmann method", *Computers and Mathematics with Applications*, Elsevier Ltd, Vol. 58 No. 5, pp. 965–974.

Kwak, H.S. and Hyun, J.M. (1996), "Natural convection in an enclosure having a vertical sidewall with time-varying temperature", *Journal of Fluid Mechanics*, Vol. 329, pp. 65–88.

Luo, L.S. (2000), "Theory of the lattice Boltzmann method: Lattice Boltzmann models for nonideal gases", *Physical Review E - Statistical Physics, Plasmas, Fluids, and Related Interdisciplinary Topics*, Vol. 62 No. 4, pp. 4982–4996.

El Mansouri, A., Hasnaouia, M., Amahmida, A., Dahania, Y., Alouaha, M., Hasnaouia, S., Khaoulaa, R., *et al.* (2017), "MRT-LBM simulation of natural convection in a Rayleigh-Benard cavity with linearly varying temperatures on the sides: Application to a micropolar fluid", *Frontiers in Heat and Mass Transfer*, Vol. 9 No. November, available at:https://doi.org/10.5098/hmt.9.28.

Mayne, D.A., Usmani, A.S. and Crapper, M. (2000), "h-adaptive finite element solution of high Rayleigh number thermally driven cavity problem", *International Journal of Numerical Methods for Heat and Fluid Flow*, Vol. 10 No. 6, pp. 598–615.

Mezrhab, A., Amine Moussaoui, M., Jami, M., Naji, H. and Bouzidi, M. (2010), "Double MRT thermal lattice Boltzmann method for simulating convective flows", *Physics Letters, Section A: General, Atomic and Solid State Physics*, Elsevier B.V., Vol. 374 No. 34, pp. 3499–3507.

Mohamad, A.A. (2019), *Lattice Boltzmann Method: Fundamentals and Engineering Applications with Computer Codes*, 2nd ed., Springer, available at:https://doi.org/10.1007/978-1-4471-7423-3.

Molla, M.M., Haque, M.J., Khan, M.A.I. and Saha, S.C. (2018), "GPU Accelerated Multiple-Relaxation-Time Lattice Boltzmann Simulation of Convective Flows in a Porous Media", *Frontiers in Mechanical Engineering*, Vol. 4 No. November, available at:https://doi.org/10.3389/fmech.2018.00015.

Moufekkir, F., Moussaoui, M.A., Mezrhab, A., Lemonnier, D. and Naji, H. (2012), "MRT-lattice Boltzmann computations of natural convection and volumetric radiation in a tilted square enclosure", *International Journal of Thermal Sciences*, Elsevier Masson SAS, Vol. 54, pp. 125–141.

Nasseri, L., Himrane, N., Ameziani, D.E., Bourada, A. and Bennacer, R. (2021), "Time-Periodic Cooling of Rayleigh–B é nard Convection".

Ouertatani, N., Ben Cheikh, N., Ben Beya, B. and Lili, T. (2008), "Numerical simulation of two-dimensional Rayleigh-Bénard convection in an enclosure", *Comptes Rendus - Mecanique*, Vol. 336 No. 5, pp. 464–470.

Peng, Y., Zhang, J.M. and Zhou, J.G. (2016), "Lattice Boltzmann Model Using Two Relaxation Times for Shallow-Water Equations", *Journal of Hydraulic Engineering*, Vol. 142 No. 2, p. 06015017.

Pletcher, R.H., Tannehill, J.C. and Anderson, D. (2016), *Computational Fluid Mechanics and Heat Transfer*, 3rd ed., CRC Press.

Seta, T. (2009), "Lattice Boltzmann Method for Fluid Flows in Anisotropic Porous Media with Brinkman Equation", *Journal of Fluid Science and Technology*, Vol. 4 No. 1, pp. 116–127.

Seta, T. (2010), "Lattice Boltzmann Method for Natural Convection in Anisotropic Porous Media", *Journal of Fluid Science and Technology*, Vol. 5 No. 3, available at:https://doi.org/10.1299/jfst.5.585.

Shan, X. (1997), "Simulation of Rayleigh-Bénard convection using a lattice Boltzmann method", *Physical Review E - Statistical Physics, Plasmas, Fluids, and Related Interdisciplinary Topics*, Vol. 55 No. 3, pp. 2780–2788.

Sheremet, M.A., Pop, I. and Mahian, O. (2018), "Natural convection in an inclined cavity with time-periodic temperature boundary conditions using nanofluids: Application in solar collectors",

International Journal of Heat and Mass Transfer, Elsevier Ltd, Vol. 116, pp. 751–761.

Shu, C., Peng, Y. and Chew, Y.T. (2002), "Simulation of natural convection in a square cavity by Taylor series expansion- and least squares-based lattice Boltzmann method", *International Journal of Modern Physics C*, Vol. 13 No. 10, pp. 1399–1414.

Silva, G. and Semiao, V. (2012), "First- and Second-Order Forcing Expressions in a Lattice Boltzmann Method Reproducing Isothermal Hydrodynamics in Artificial Compressibility Form", *Journal of Fluid Mechanics*, Vol. 698, pp. 282–303.

Succi, S. (2001), *The Lattice Boltzmann Equation for Fluid Dynamics and Beyond*, Oxford University Press.

Sukop, M.C. and Thorne, D.T. (2006), *Lattice Boltzmann Modeling*, available at:https://doi.org/10.1007/978-3-540-27982-2.

Syrjälä, S. (1996), "Higher order penalty-galerkin finite element approach to laminar natural convection in a square cavity", *Numerical Heat Transfer; Part A: Applications*, Vol. 29 No. 2, pp. 197–210.

Trouette, B. (2013), "Lattice Boltzmann simulations of a time-dependent natural convection problem", *Computers and Mathematics with Applications*, Elsevier Ltd, Vol. 66 No. 8, pp. 1360–1371.

Ubertini, S., Asinari, P. and Succi, S. (2010), "Three ways to lattice Boltzmann: A unified time-marching picture", *Physical Review E - Statistical, Nonlinear, and Soft Matter Physics*, Vol. 81 No. 1, pp. 1–11.

De Vahl Davis, G. (1983), "Natural convection of air in a square cavity: A bench mark numerical solution", *International Journal for Numerical Methods in Fluids*, Vol. 3 No. 3, pp. 249–264.

Varmazyar, M., habibi, M. and Mohammadi, A. (2017), "Investigation on Instability of Rayleigh-Benard Convection Using Lattice Boltzmann Method with a Modified Boundary Condition", *Journal of Computational Applied Mechanics*, Vol. 0 No. December, available at:https://doi.org/10.22059/jcamech.2017.243410.197.

Wada, K., Kaneda, M. and Suga, K. (2020), "Rayleigh-benard convection of paramagnetic liquid under a magnetic field from permanent magnets", *Symmetry*, Vol. 12 No. 3, available

at:https://doi.org/10.3390/sym12030341.

Wang, G., Wang, Q., Zeng, M. and Ozoe, H. (2008), "Numerical study of natural convection heat transfer in an inclined porous cavity with time-periodic boundary conditions", *Transport in Porous Media*, Vol. 74 No. 3, pp. 293–309.

Wei, Y., Yang, H., Dou, H.S., Lin, Z., Wang, Z. and Qian, Y. (2018), "A novel two-dimensional coupled lattice Boltzmann model for thermal incompressible flows", *Applied Mathematics and Computation*, Elsevier Inc., Vol. 339, pp. 556–567.

Wu, F. and Wang, G. (2017), "Numerical simulation of natural convection in an inclined porous cavity under time-periodic boundary conditions with a partially active thermal side wall", *RSC Advances*, Royal Society of Chemistry, Vol. 7 No. 28, pp. 17519–17530.

Yu, P.X. and Tian, Z.F. (2012), "Compact computations based on a stream-function-velocity formulation of two-dimensional steady laminar natural convection in a square cavity", *Physical Review E - Statistical, Nonlinear, and Soft Matter Physics*, Vol. 85 No. 3, pp. 1–12.

Zheng, L., Zheng, S. and Zhai, Q. (2019), "Analysis of force treatment in lattice Boltzmann equation method", *International Journal of Heat and Mass Transfer*, Elsevier Ltd, Vol. 139, pp. 747–750.

Zou, Q. and He, X. (1997), "On pressure and velocity boundary conditions for the lattice Boltzmann BGK model", *Physics of Fluids*, Vol. 9 No. 6, pp. 1591–1596.